Roles of PIKfyve in the Retina: A Zebrafish Study

by

Karen Attia

A thesis submitted in partial fulfillment of the requirements for the degree of

Master of Science

Medical Sciences - Medical Genetics
University of Alberta

ABSTRACT

Phosphoinositides (PIs) are membrane lipids that function as signaling molecules. PIs undergo phosphorylation and dephosphorylation at various positions to produce the seven known PI molecules. PIKfyve is a phosphoinositide kinase that produces phosphoinositide-3,5-bisphosphate ($PI(3,5)P_2$) and phosphoinositide-5-phosphate (PI5P). $PI(3,5)P_2$ and PI5P have a low abundance in the cell and their roles are not fully characterized. Evidence suggests involvement in melanosome biogenesis, phagocytosis, endosomal trafficking, lysosomal homeostasis, and autophagy. In humans, mutations in *PIKFYVE* are rare and have been associated with Corneal Fleck Dystrophy and congenital cataracts. Dr. Ian MacDonald at the University of Alberta identified a patient with a novel heterozygous missense mutation in *PIKFYVE* (c.5492A>G, p.(His1831Arg)). The patient does not present with corneal flecks nor congenital cataracts, but rather exhibits a retinal dystrophy phenotype. Thus, phenotypes associated with *PIKFYVE* mutations in humans are heterogeneous and present largely in the eye. Little is known about *PIKfyve in vivo* due to the embryonic lethality of gene knockout in common animal models. Here, I sought to characterize the roles of *PIKfyve in vivo* to elucidate disease mechanism in the patient using zebrafish. I used CRISPR/Cas9 mutagenesis to introduce loss of function mutations in *pikfyve*, and pharmacological inhibition to temporarily inhibit Pikfyve. Moreover, I experimented with various precise gene editing technologies in zebrafish to create a patient mimic mutant line. I found that Pikfyve inhibition/knockdown impaired retinal electrical function, increased cell death, and introduced a variety of abnormalities to the retinal pigment epithelium. Moreover, I determined that cytosine base editing is efficient in zebrafish and established the technique in our lab.

PREFACE

This thesis is an original work by Karen Attia. Approval for this study was obtained from the Animal Care and Use Committee: Biosciences, under protocol AUP1476.

ACKNOWLEDGEMENTS

I am extremely grateful for the learning opportunities and challenges my master's degree has provided me with. I would first like to thank Jesus Christ for guiding and sustaining me throughout every step of this journey. I could not have gotten through my masters without His grace and the prayers of my intercessor, Baba Kyrillos.

I would like to express my deep gratitude to my supervisor, Dr. Jennifer Hocking, for giving me this opportunity. Working in your lab throughout the years has been an invaluable experience that allowed me to grow both academically and personally. Your curiosity and expertise are an inspiration, and I am truly thankful to have had a mentor as caring and supportive as you are.

I would also like to extend my gratitude to my lab mates: Ifrah, Masha, Constantin, and Ehsan. You were all a blessing to work with and I have learnt so much from every one of you.

I would like to thank my committee members, Dr. Ian MacDonald and Dr. Alan Underhill, and my external examiner, Dr. Nicolas Touret, for their time and honest feedback, which has greatly helped shape and advance this work.

I would also like to extend my gratitude to all the labs and students on the 5th floor of the medical sciences building, especially the Webber, Rabey, Simmonds, LaPointe, and Eitzen labs. Not only were they extremely gracious with sharing resources, but they were also always there to support throughout failed experiments and slight frustrations. I would also like to thank Dr. Kacie Norton of the microscopy unit, the HSLAS and MBSU staff for all their help.

Finally, I would like to thank my family for their endless support, love, and patience. I am grateful for all your prayers and kindness in the most stressful of times.

TABLE OF CONTENTS

LIST OF TABLES

LIST OF FIGURES

CHAPTER ONE: INTRODUCTION

1.1 Anatomy of the Human Eye

1.1.1 General Anatomy

Our eyes (Fig. 1.1) are complex organs that capture visual information from our surroundings and relay it as an electrical impulse to the brain. The eye is located within the orbit of the skull and is attached to six extraocular muscles that control its movement and rotation. The first point of contact of light in the eye is the cornea, a transparent, modified mucous membrane covering of the anterior eye that consists of six histologically distinct layers. Directly behind the cornea is the anterior chamber, which is filled with a liquid called the aqueous humor. The iris is a colored, opaque ring that controls the amount of light entering the eye through the pupil using a set of opposing constrictor and dilator muscles. Behind the pupil is the lens, a transparent, biconvex disc that focuses light onto the retina at the back of the eye. The lens is connected to a ring of smooth muscle called the ciliary body through suspensory ligaments. Through contracting and relaxing, the ciliary body changes the shape of the lens, thereby changing its refractive index in a process known as accommodation. The ciliary body also produces aqueous humor. The region between the iris and the lens is known as the posterior chamber while the region between the lens and the back of the eye is known as the vitreous chamber and is filled with a gel-like fluid called the vitreous humor. Both humors in the eye maintain its shape and pressure. Forming the inner lining of the vitreous chamber is a thin layer of neural sensory tissue, the retina, which will be discussed in detail in the next section. External to the retina lies the choroid, a pigment-rich layer containing a dense network of blood vessels that nourish the retina and absorb excess and stray light photons. The choroid is separated from the retina by the extracellular matrix of the Bruch's membrane and is loosely attached to the sclera. The sclera is a

white, opaque layer of fibrous connective tissue that provides structural support and maintains the shape of the eye.

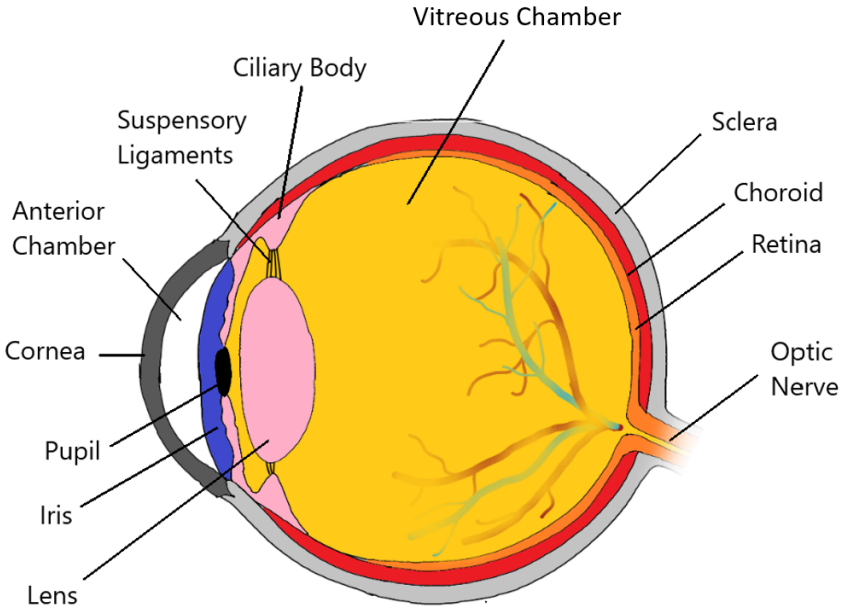

Figure 1.1 – Anatomy of the human eye. Key structures of the eye are labeled, and functions are discussed in section 1.1.1.

1.1.2 Retinal Layers

During development, the neural tube gives rise to lateral extensions, the optic vesicles, which collapse into the double-layered optic cups that give rise to the retina of each eye. The inner layer will form the neurosensory retina, while the outer layer becomes the retinal pigment epithelium (Casey et al., 2023). The primary role of the neurosensory retina, which will be referred to as the retina from now on, is to capture and transduce light photons into a neural signal that can be relayed and interpreted by the brain. Two main subtypes of cells exist in the retina: neuronal cells, including the light-detecting photoreceptors, and glial cells. Furthermore,

the retina is divided into various layers (Fig. 1.2) each performing a specialized function. The retina is the most metabolically active tissue, consuming more oxygen per cell than any other tissue in the body. The following sections will focus on the neurosensory retina, composed of the photoreceptors, amacrine cells, bipolar cells, horizontal cells, ganglion cells, and Müller glia.

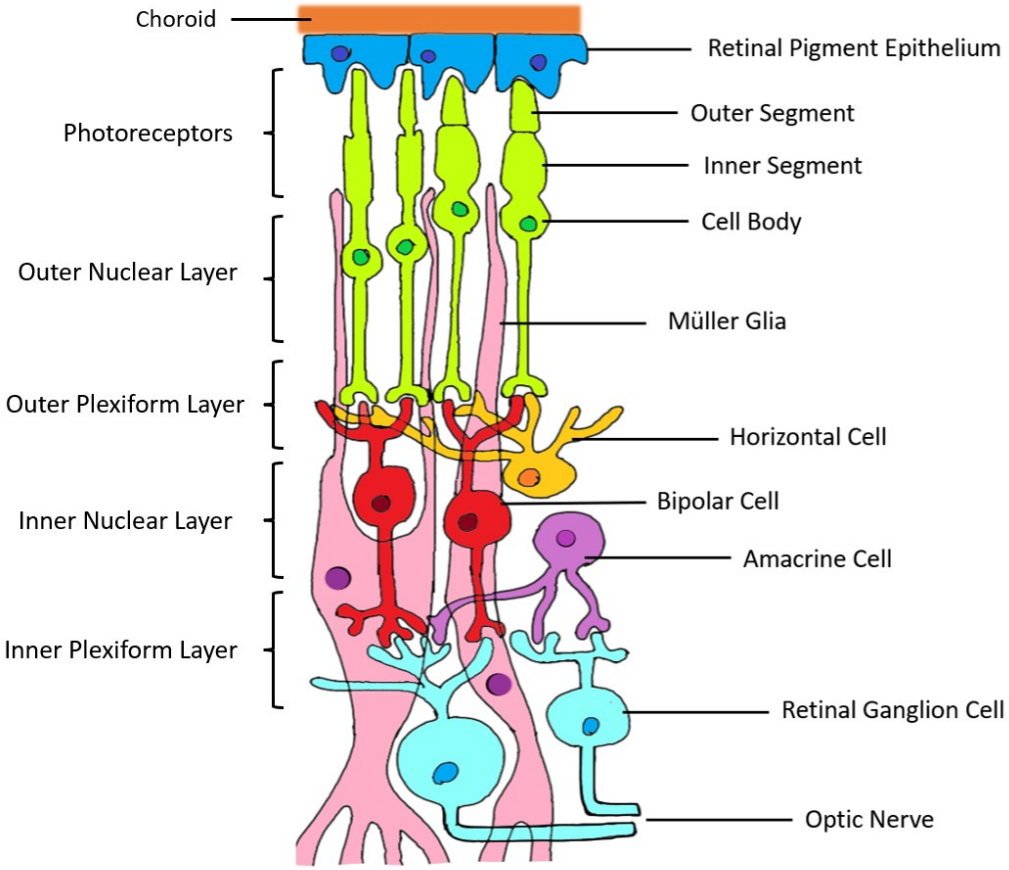

Figure 1.2 – Organization of the retina. The retina is made up of various cell types organized in distinct layers.

1.1.2.1 Photoreceptors

Photoreceptors are in the posterior aspect of the retinal sublayers and are the primary light-detecting cells of the eye. In vertebrates, there are two types of photoreceptor cells: rods

and cones. Rods are highly sensitive cells that primarily detect photons in dim conditions. Approximately 95% of photoreceptors in humans are rods and they are located most densely in the retinal periphery. Rods contain the light-sensitive pigment rhodopsin, responsible for photon absorption. Cones, on the other hand, mediate daytime and color vision. In humans, there are three subtypes of cones: tritans, deutans, and protans, which detect light of short, medium, and long wavelengths, respectively. Cones are concentrated in the central retina and are the only photoreceptors present within the fovea, the central-most region of the retina. While rods and cones function in different light conditions, their structure and mechanism of light detection are very similar.

Each photoreceptor, whether a rod or a cone, consists of an outer segment, an inner segment, a cell body, and synaptic ending. The outer segment (OS) is a specialized cilium that captures light photons and contains stacks of membranous discs. In cones, these discs are continuous with each other and the plasma membrane, while in rods discs are distinct units. Nevertheless, in both subtypes the OS discs house an enormous number of light-sensitive integral membrane proteins called opsins, as well as other components of the phototransduction machinery. Although photoreceptors cannot regenerate in humans, the photoreceptor OSs undergo a continual process of shedding and renewal where every day discs are generated proximally and shed distally as packets. The inner segment (IS) and OS are linked via a thin connecting cilium that transports metabolites, lipids, and proteins between the two segments as needed. The IS is further made up of two regions. First, the distal ellipsoid region which is densely packed with mitochondria and houses the basal body of the connecting cilium. Second, the proximal myoid region which contains various organelles including the smooth endoplasmic reticulum, the Golgi apparatus, and microtubules. Photoreceptor cell bodies form the outer

nuclear layer (ONL) of the retina while the synaptic layer between the photoreceptors and downstream cells in the inner nuclear layer (INL) is called the outer plexiform layer (OPL).

1.1.2.2 Retinal Interneurons

Bipolar cells are interneurons that receive neural input from photoreceptors and synapse onto retinal ganglion cells. There are 13 different types of bipolar cells, and they can be divided into rod bipolar cells and cone bipolar cells depending on which photoreceptor subtype they receive information from. Each bipolar cell is further characterized by whether it depolarizes or hyperpolarizes in response to light. Bipolar cells extend from the OPL through the INL and into the inner plexiform layer (IPL).

Horizontal cells are GABAergic interneurons that receive information from photoreceptors. They are located along the OPL and play a role in early visual processing. Namely, they mediate the process of lateral inhibition, collecting information from photoreceptors and providing feedback to surrounding bipolar cells (Chapot et al., 2017). Horizontal cells thus fine-tune photoreceptor cell output, enhancing contrast in the visual field. (Kramer et al., 2015).

Also functioning laterally in the retina are amacrine cells. Amacrine cells are extremely diverse, but they generally receive input from bipolar cells and other amacrine cells and synapse onto ganglion cells, amacrine cells, or bipolar cells. Amacrine cells release the inhibitory neurotransmitters GABA and glycine although their function can be either inhibitory or excitatory depending on their target neuron. The exact roles of amacrine cells are not clearly defined. However, they are thought to contribute to modulating the light response signal transmitted to retinal ganglion cells.

1.1.2.3 Retinal Ganglion Cells

Retinal ganglion cell (RGC) dendrites synapse with bipolar and amacrine cells in the IPL and are the final path of transmission of the light response to the brain. There are approximately 20 different RGCs, 1-2% of which are intrinsically light sensitive. Like the photoreceptor response, the signal from intrinsically photosensitive retinal ganglion cells (ipRGC) is transmitted to the brain; however, the information functions to regulate physiological processes such as circadian rhythm, melatonin release, and pupil size, and does not contribute to vision. The axons of RGC bundle together at the optic disc and exit the eye as a single unit, the optic nerve.

1.1.2.4 Müller Glia

The retina contains three types of glial cells: Müller glia, astroglia, and microglia. Müller glia are the most abundant of the three; their cell bodies sit in the inner nuclear layer, but their processes span the retinal layers. On one side, Müller glial endfeet form the inner limiting membrane (ILM), which separates the vitreous chamber from the retina. On the other side, Müller glia extend their apical processes through the ONL to form adherens junctions with photoreceptor ISs. The appearance created in histology by the line of Müller glia-photoreceptor junctions gave rise to the term outer limiting membrane (OLM). Müller glia provide structural and metabolic support to retinal neurons. For example, they serve as a cushion for protection of the retina from physical trauma, and they are involved in retinal neuronal plasticity (Kobat 2020).

1.1.2.5 Retinal Pigment Epithelium

The retinal pigment epithelium (RPE) is a monolayer of pigment-rich cells located outside the neurosensory retina, between the photoreceptor OS and the choroid. It is a neuroepithelium derived during embryogenesis from the outer layer of the optic cup. Overall, the RPE supports photoreceptor function and maintains outer retinal homeostasis. It contributes to visual spatial resolution as its pigment absorbs stray light photons, preventing the scattering of light in the retina. Further, the RPE mediates the visual cycle by recycling the vitamin A derivative all-trans-retinal to 11-cis-retinal and is therefore critical in phototransduction and vision. The RPE also regulates the movement of solutes and nutrients as it forms the outer part of the barrier between the neurosensory retina and systemic circulation known as the retinal-blood barrier. RPE cells have processes that extend apically into the photoreceptor OS layer and in humans, each RPE cell is in contact with ~30 photoreceptors (Lakkaraju et al., 2020).

RPE cells (along with Sertoli cells in the testis) are known as specialized phagocytes. Unlike circulating phagocytic immune cells, specialized phagocytes are resident to a particular tissue, form tissue-blood barriers, and facilitate transport (Penberthy et al., 2018). The RPE has one of the highest phagocytic demands in the body. Each RPE cell is responsible for the phagocytosis of shed OS discs from ~30 photoreceptors. Approximately 7-10% of the OS is shed daily, meaning the RPE phagocytoses the entire OS every 2 weeks (Lakkaraju et al., 2020). The complex process of OS disc engulfment and degradation is triggered by light onset or offset and typically occurs within hours in a healthy RPE (Lakkaraju et al., 2020). Accumulation of ingested OS in the RPE results in the formation of lipofuscin, an autofluorescent material that accumulates with age, and is primarily made up of vitamin A aldehyde derivatives known as bisretinoids (Sparrow et al., 2012). Although lipofuscin is found in normal RPE cells, its

production is accelerated in various retinal disorders and is thus often a hallmark of retinal degeneration (Sparrow et al., 2012). Notably, the RPE and photoreceptors are not only spatially close, but their function relies on one another and therefore, RPE dysfunction leads to photoreceptor degeneration, and vice versa. The next section will focus on the process of OS phagocytosis and degradation by the RPE.

1.1.2.5.1 Outer Segment Processing

The process of OS shedding, phagocytosis, and degradation by the RPE is complex and involves numerous signaling molecules. A brief overview of key players is summarized here. The first step of the process involves the recognition of OS discs by the RPE. Photoreceptor OSs accumulate phosphatidylserine (PS) on their distal tips facing the RPE, especially following light onset (Lakkaraju et al., 2020). The PS acts like an "eat me" signal when exposed to the extracellular space. Milk fat globule E8 (MFGE8) is a glycoprotein secreted by the RPE, and it binds exposed PS on OS tips and serves as a ligand for αvβ5, an integrin receptor located on the apical side of the RPE (Nandrot et al., 2007). Next, αvβ5 forms a complex with CD81, which facilitates OS binding to the apical RPE (Kwon et al., 2020). Further, αvβ5 activates a signaling cascade that triggers the ingestion of the OS by the RPE cell. MERTK, a member of the Tyro-Axl-Mer ingestion receptor family, is the primary mediator of OS ingestion. RAC1, a small GTP-binding protein, facilitates actin remodeling and formation of an actin-rich phagocytic cup around the ingested OS (Kwon et al., 2020). The process of phagocytic cup closure and withdrawal of the ingest OS into the RPE cell is not clearly understood although it likely involves myosin-2 (Umapathy et al., 2023).

Following ingestion, phagosomes undergo a complex series of maturation steps that involve fusion with endosomes and finally lysosomes. As phagosomes mature, the RPE

microtubule cytoskeleton, with the motor proteins kinesin-1 and dynein-1, mediates their migration from the apical to the basal side of the RPE (Kwon et al., 2020). The degradation of phagosome contents is a multi-step process that includes the acquisition of V-ATPase for the acidification of the phagosomes (Kwon et al., 2020). Moreover, the lysosomal protease Cathepsin D and cysteine proteases are involved (Kwon et al., 2020).

Interestingly, a significant proportion of phagosomes in the RPE are processed by a different mechanism. Approximately 30-45% of OS phagosomes acquire the microtubule-associated protein 1 light chain 3B (LC3B) in a process known as LC3-associated phagocytosis (LAP) (Kwon et al., 2020). The exact mechanism and role of LAP in the RPE remains enigmatic although literature suggests it plays a neuroprotective role (Kwon et al., 2020). One class of molecules known to be critical in LC3-independent phagocytosis (and likely LAP as well) is phosphoinositides (PIs) (Lakkaraju et al., 2020). PIs are important signaling molecules involved in various cellular pathways. The next section will focus on phosphoinositides, highlighting the phosphoinositide kinase, PIKfyve.

1.2 Phosphoinositides

1.2.1 Overview

Cells and intracellular organelles such as lysosomes and mitochondria are surrounded by membranes made up of proteins and lipids. Cholesterol, glycerophospholipids, and sphingolipids are all examples of lipids that maintain the structural integrity of the cell and organelle membranes. Additionally, some lipids function as signaling molecules. One such example is phosphoinositides (PIs) (Hasegawa et al., 2017). PIs are derived from phosphatidylinositols, which are similar in structure to other phospholipids and consist of a glycerol backbone, two

fatty acids, and a six-membered cyclic polyol myo-inositol head group (Falkenburger et al., 2007). The inositol group can be variably phosphorylated at positions 3, 4, and 5 to generate the seven known PIs (Fig. 1.3). PIs comprise <1% of total phospholipids in eukaryotic cells and their regulation is achieved by various PI kinases, phosphatases, and phospholipases. PIs localize to distinct membranes, as illustrated in Fig. 1.5, where they mediate intracellular signaling by recruiting various proteins to the membrane (Hasegawa et al., 2017). PIs are also involved in ciliogenesis, vesicular transport, cytoskeleton assembly, ion channel regulation, and membrane dynamics (Rajala et al., 2022)

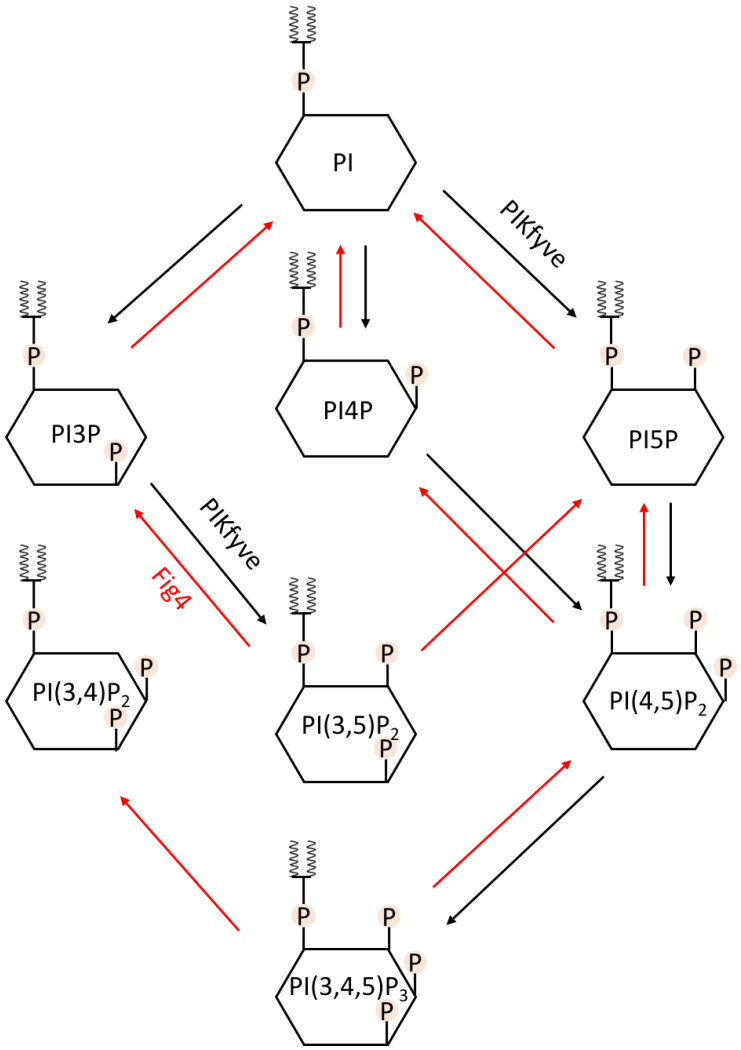

Figure 1.3 – Relationship between the seven phosphoinositides. The actions of kinases are represented by black arrows while the actions of phosphatases are represented by red arrows. PIKfyve kinase primarily phosphorylates PI3P into $PI(3,5)P_2$ and can also produce PI5P from PI. Fig4 phosphatase dephosphorylates $PI(3,5)P_2$ into PI3P.

1.2.2 Roles in the Retina

The retina contains several highly specialized membranes such as the photoreceptor OS discs, apical RPE processes, and bipolar cell and photoreceptor ribbon synapses. As discussed, PIs are critical in membrane dynamics and therefore it is plausible that PIs have a role in the retina, likely through the formation, maintenance, and function of these specialized membranes (Wensel et al., 2020). However, there have been few measurements of PIs in the retina due to their low abundance and difficult detection. Nevertheless, more sensitive detection techniques, such as freeze-fracture electron microscopy combined with the use of tagged proteins (Takatori et al., 2016), are being developed and they support the presence of PIs in the retina (Wensel et al., 2020). For instance, using ribosomal targeting and nuclear labeling, one study found that phosphatidylinositol-3-phosphate (PI3P) was highly expressed in samples containing both rod IS and OS (Rajala et al., 2022). Another recent study detected the presence of PIs to varying degrees in mouse retinas, consistent with the expression of various phosphatidylinositol phosphate kinases (PIPK) (Rajala et al., 2022).

The exact roles of PIs within the retina remain largely unexplored. However, evidence suggests that PIs are important in multiple retinal cell subtypes including photoreceptors, ipRGCs, and especially the RPE (Wensel et al., 2020). Processes mediated by PIs such as phagocytosis, autophagy, endocytosis, and endosomal processing are critical to RPE function.

Indeed, the RPE shows increased levels of PI3P in response to the addition of rod OS in isolated mouse rat cells (Wensel et al., 2020). Moreover, genetic defects that alter the levels of PIs, for instance mutations affecting the PI phosphatases INPPE5 and synaptojanin are associated with retinal degeneration and severe cone defects, respectively (Wensel et al., 2020).

This thesis will focus on phosphatidylinositol-3,5-bisphosphate ($PI(3,5)P_2$) and phosphatidylinositol-5-phosphate (PI5P) and their significance in the retina. $PI(3,5)P_2$ is one of the least abundant and least studied PIs and it makes up 0.04% of total PIs in mouse embryonic fibroblasts (MEF) (Rivero-Rios et al., 2022). PI5P is present at higher levels, making up 0.5% in MEF (Rivero-Rios et al., 2022). Our understanding of the involvement of PI5P and $PI(3,5)P_2$ in vesicular trafficking and maturation is incomplete, although literature suggests that both PIs play an important role. The next section will focus on PIKfyve - the kinase responsible for the production of $PI(3,5)P_2$ and PI5P.

1.3 PIKfyve

1.3.1 Overview

PIKfyve, also called Fab1 in yeast, is a phosphoinositide kinase encoded by the *PIKfyve* gene. In the literature, *PIKfyve/*PIKfyve is used to refer to the gene/protein in general while *PIKFYVE/*PIKFYVE refers specifically to the human gene/protein and *pikfyve/*Pikfyve refers to the zebrafish gene/protein. In humans, *PIKFYVE* is located on chromosome 2 and is 42 exons long. The human PIKFYVE protein is 2089 amino acids long, and it consists of six functional domains. The zinc finger phosphoinositide kinase (FYVE) domain binds PI3P, the pleckstrin homology (PH) domain binds PIs, the β-sheet winged helix DNA/RNA-binding motif binds DNA and RNA, the cytosolic chaperone CCTγ apical domain-like motif and spectrin repeats

facilitate protein-protein interactions, and the C-terminal fragment phosphoinositol phosphate (PIP) kinase domain underlies the protein's catalytic activity (Gee et al., 2015, Mei et al., 2021). *PIKFYVE* is ubiquitously expressed throughout all tissues, with particularly high expression in ocular tissues and the pancreas (Fig. 1.4). PIKfyve is the only kinase that catalyzes the production of $PI(3,5)P_2$, which it produces through the phosphorylation of PI3P (Rivero-Rios et al., 2022). Moreover, it catalyzed the production of PI5P both directly through phosphorylating PI at the 5^{th} position and indirectly through myotubularin-related (MTMR) phospholipid phosphatase-mediated dephosphorylation of $PI(3,5)P_2$ (Wensel et al., 2022).

PIKfyve is tightly regulated in a complex pathway that involves the lipid phosphatase Fig4 (Rivero-Rios et al., 2022). Using cryoelectron microscopy and negative-stain, Lees et al., resolved the structure of the PIKfyve complex and found that Vac14, a scaffolding protein, pentamerizes into a star-shaped structure to which one copy each of PIKfyve and Fig4 bind (Lees et al., 2020). More specifically, PIKfyve and Fig4 bind opposite legs of the Vac14 pentamer, which has significant implications for the complex's function (Rivero-Rios et al., 2022). PIKfyve is capable of autophosphorylation, inhibiting its own activity (Rivero-Rios et al., 2022). Paradoxically, the phosphatase required for its activation, Fig4, also dephosphorylates its product $PI(3,5)P_2$ back to PI3P (Rivero-Rios et al., 2022). Therefore, these two proteins have a close interplay where initially the Fig4 catalytic site is in contact with the membrane giving it access to $PI(3,5)P_2$ while the catalytic site of PIKfyve is oriented away from the membrane (Lees et al., 2020). Upon activation, the complex undergoes a structural rearrangement so that the PIKfyve catalytic site is in contact with the membrane not only giving it access to PI3P, but also orienting it towards Fig4 for its dephosphorylation and activation (Lees et al., 2020).

PIKfyve plays an essential role in multiple cellular pathways which may be mediated by $PI(3,5)P_2$, PI5P, or both. Initially, PIKfyve was thought to only be involved with lysosomes (Rivero-Rios et al., 2022). However, growing evidence suggests roles in autophagy, phagocytosis, melanosome biogenesis, and endosomal trafficking (Hasegawa et al., 2017). A summary of the various pathways in which PIKfyve is implicated is provided in the next section.

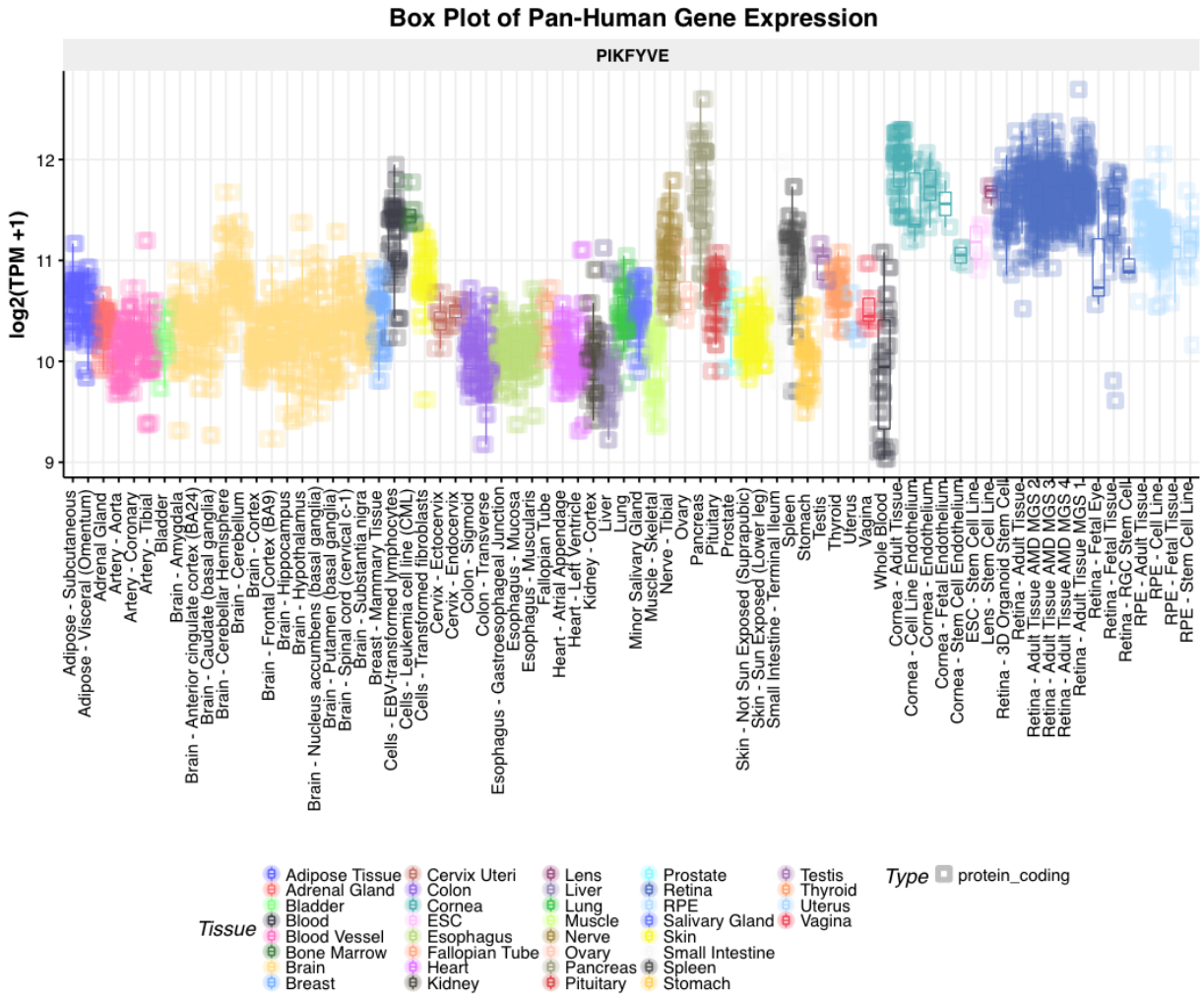

Figure 1.4 – Expression of *PIKFYVE* across human tissues. Figure adapted from eyeIntegration, NEI and shows ubiquitous expression of *PIKFYVE* across human tissues, with elevated levels in the pancreas and the eye (provided by Matt Benson, courtesy of NEI).

1.3.2 Involvement in Cellular Pathways

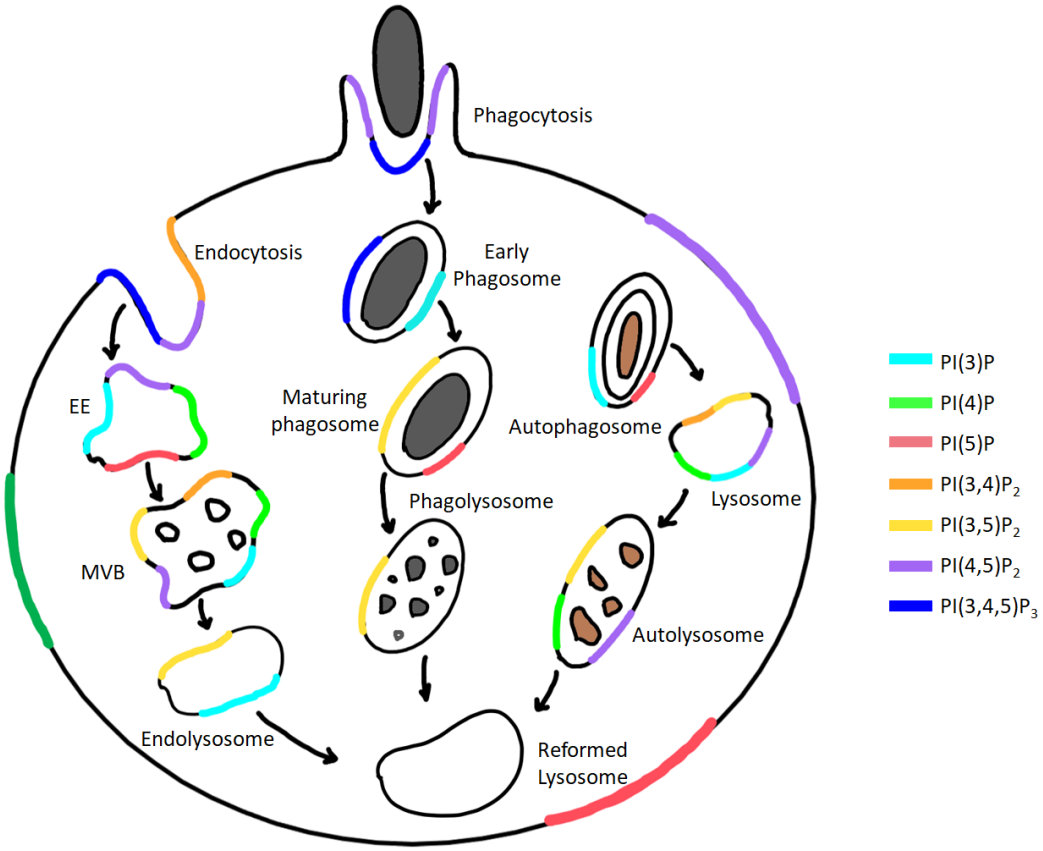

Figure 1.5 – Overview of phosphoinositides in multiple cellular pathways. Endosomal trafficking, phagosome maturation, and autophagy are summarized and the various phosphoinositides implicated in each step are shown. EE= early endosome, MVB= multivesicular body.

1.3.2.1 Lysosomal Homeostasis

The role of PIKfyve in lysosomal function is the most-well studied, and it is primarily mediated by $PI(3,5)P_2$. PIKfyve maintains lysosomal homeostasis through three main processes: ion homeostasis, lysosomal acidification, and lysosomal fission (Rivero-Rios et al., 2022). $PI(3,5)P_2$ is the ligand that activates the lysosomal mucolipin TRP calcium channel, TRPML1

(Li et al., 2020). Moreover, $PI(3,5)P_2$ also directly binds to lysosomal sodium two-pore channels, TRC1 and TRC2 (Li et al., 2020). Notably, the most observed result of PIKfyve inhibition in cell culture is the formation of vacuoles (Rivero-Rios et al., 2022). One potential mechanism underlying vacuolization is the buildup of fluid within lysosomes. Upon inhibition of PIKfyve, $PI(3,5)P_2$ production ceases and therefore, TRPML1, TRC1, and TRC2 are inactivated, which results in a buildup of calcium and sodium ions inside the lysosomes (Rivero-Rios et al., 2022). An influx of water into lysosomes follows, leading to swelling and the formation of large vacuoles (Rivero-Rios et al., 2022). $PI(3,5)P_2$ is also important in maintaining lysosomal pH. Lysosomes are characterized by an acidic pH that activates lysosomal hydrolases. The addition of the PIKfyve inhibitor apilimod to yeast and mammalian cells results in an increase in lysosomal pH (Banerjee et al., 2020, Ponsford et al., 2020). Hence, it is likely that $PI(3,5)P_2$ is a regulator of the v-ATPase responsible for lysosomal acidification (Rivero-Rios et al., 2022). Finally, $PI(3,5)P_2$ drives lysosomal fission through a mechanism not fully understood (Rivero-Rios et al., 2022). Many cellular pathways terminate by fusion with a lysosome (Fig. 1.5). After degradation, it is important for lysosomes to reform to continue degrading other vesicles. PIKfyve inhibition impairs lysosomal fission and leads to a steady-state increase in lysosomal fusion and therefore, lysosomal enlargement (Rivero-Rios et al., 2022).

1.3.2.2 Endosomal Trafficking

Endosomes are intracellular vesicles formed by the endocytosis of macromolecules such as proteins and lipids from the extracellular space into the cytoplasm through plasma membrane invagination and remodeling. Immediately following endocytosis, vesicles are referred to as early endosomes (EE). EE membranes are enriched in PI3P, which recruits protein complexes that result in the invagination of the EE membrane into multiple intralumenal vesicles (Lartigue

et al., 2009). This process results in the formation of multivesicular bodies (MVBs) or late endosomes. Late endosomes then fuse with lysosomes to form endolysosomes, through which cargo is degraded.

Three key PIs play an important role in endosomal trafficking: PI3P, PI5P, and PI(3,5)P_2. As mentioned, PI3P is enriched on EE where it mediates maturation into a MVB through recruiting FYVE-containing effector proteins (Lartigue et al., 2009). Similarly, PI5P localizes to the EE membrane and its upregulation enhances endocytosis (Ramel et al., 2011, Viaud et al., 2014). In contrast, PI(3,5)P_2 is primarily localized to late endosomes and lysosomes (Hasegawa et al., 2017). Bissig et al., found that inhibition of PIKfyve resulted in the accumulation of enlarged endolysosomes in HeLa cells, suggesting a role for PI(3,5)P_2 in reformation of lysosomes from endolysosomes. Thus, PI3P and PI5P are involved in early endosomal trafficking while PI(3,5)P_2 is involved in the later steps of the endosomal pathway.

1.3.2.3 Phagocytosis

Phagocytosis and phagosome maturation were described in section 1.1.2.5.1. Much of the knowledge about the role of PIKfyve in phagocytosis comes from studies done on macrophages, which are professional phagocytes of the immune system that degrade pathogens and cellular debris (Kim et al., 2014). Like other phagocytes, macrophages engulf target pathogens within a membrane to form an intracellular phagosome. Through a series of fusions with endosomes and lysosomes, the phagosome matures into a highly acid phagolysosome that is then able to break down the engulfed pathogens (Kim et al., 2014). The level of PI(3,5)P_2 gradually increases as phagosomes mature in macrophages (Hasegawa et al., 2017). Moreover, silencing of *PIKfyve* by shRNA or pharmacological inhibition results in delayed phagosome maturation (Kim et al., 2014). Kim et al., found that PIKfyve is crucial in trafficking phagosomes to lysosomes and

maintaining both organelle's degradative capacity. Of note, the authors were not able to contribute this solely to $PI(3,5)P_2$ as PI5P may also be involved. Another mechanism through which PIKfyve is implicated in phagocytosis is through the TRPML1 lysosomal channel. TRPML1 facilitates the movement of calcium out of lysosomes which mediates phagosome-lysosome fusion. Indeed, Dayam et al., found that when TRMPL1 was silenced or PIKfyve inhibited, lysosomes docked to phagosomes but did not fuse (Dayam et al., 2015).

1.3.2.4 Autophagy

Autophagy, or macroautophagy, is a conserved, complex intracellular degradation pathway that removes damaged and unnecessary organelles and proteins (O'Connell et al., 2023). Autophagy is triggered by cellular stress such as starvation and it involves the formation of a double-membrane vesicle called an autophagosome around the target components (O'Connell et al., 2023). Following the engulfment of degradation components, autophagosomes fuse with lysosomes to create autolysosomes. Through enzymatic activity, contents are degraded into their building blocks and recycled for energy and macromolecule synthesis (O'Connell et al., 2023). Autophagy involves the activity of many different proteins including PIKfyve. In liver cancer cells, PIKfyve inhibition results in the accumulation of autophagosomes (Hou et al., 2018). This suggests that $PI(3,5)P_2$, and/or PI5P, is involved in autophagosome-lysosome fusion. Moreover, mutations in the autophagy protein Atg18 that interfere with its binding to $PI(3,5)P_2$ cause defects in autophagy (Hasegawa et al., 2017). Our knowledge of the exact roles of PIKfyve in autophagy is limited; however, evidence suggests that both PI5P and $PI(3,5)P_2$ are important mediators of the process.

1.3.2.5 Melanosome Biogenesis

Melanosomes are lysosome-related organelles that synthesize and store melanin. Melanosome biogenesis and maturation occurs in four steps, beginning with stage I melanosomes derived from specialized early endosomes (Liggins et al., 2018). Stage I melanosomes are characterized by the presence of the transmembrane protein premelanosome (PMEL), which undergoes cleavage and fibrillation during the transition into a stage II melanosome (Bissig et al., 2019). Endosomes transport key melanogenesis enzymes including tyrosinase from the Golgi to stage II melanosomes (Theos et al., 2005). In stage III melanosomes, tyrosinase mediates the production of melanin, which is deposited onto PMEL fibrils (Bissig et al., 2016). Maturation is complete within stage IV melanosomes, which are opaque organelles that are densely packed with melanin (Liggins et al., 2018).

Mice with knockout of Fig4, one of the PIKfyve complex proteins, exhibit lack of pigmentation. Nevertheless, the role of PIKfyve in pigment formation had been unexplored until recently. Liggins et al., demonstrated that melanocyte-specific knockout of *Pikfyve* in mice results in the accumulation of stage I and II melanosomes. The authors determined that PIKfyve is important in trafficking of tyrosinase-containing endosomes from the Golgi to stage II melanosomes. Moreover, Bissig et al., found that PIKfyve is required for membrane remodeling during the transition from stage I to II melanosomes. Together, these findings demonstrate the role of $PI(3,5)P_2$ and potentially PI5P in melanogenesis.

1.3.3 Clinical Relevance of PIKFYVE

Human mutations in *PIKFYVE* are ultrarare and mostly associated with Corneal Fleck Dystrophy, an autosomal dominant, non-progressive disease with a prevalence of <1/1,000,000.

Affected patients typically remain asymptomatic with white, opaque flecks that appear within the stromal layer of the cornea (Gee et al., 2015). Corneal flecks consist of dilated keratocytes that are filled with complex lipids and glycosaminoglycans in intracytoplasmic vesicles, and flecks do not affect vision (Gee et al., 2015). Mutations associated with Corneal Fleck Dystrophy fall within the cytosolic chaperone CCTγ apical domain-like motif, FYVE domain, or SPEC domain of PIKFYVE. Frameshift, nonsense, missense, splice-site, and copy number variants have been identified (Gee et al., 2015)

A novel phenotype associated with *PIKFYVE* mutations was recently reported by Mei et al. The authors identified a Chinese Korean family with congenital cataracts. All affected individuals that underwent whole exome sequencing carried a novel heterozygous missense p.(G1943E) variant in *PIKFYVE*, while an unaffected family member did not (Mei et al., 2021). Modeling in zebrafish revealed that the variant likely causes disease through haploinsufficiency and not dominant-negative inhibition as overexpression of the mutation-containing gene did not produce a cataract phenotype in fish, but gene knockdown did (Mei et al., 2021). Curiously, none of the affected patients identified had corneal flecks. Unlike Corneal Fleck Dystrophy patients, the variant identified by Mei et al. falls within the kinase domains of the PIKFYVE protein, suggesting that the location of the mutation has a profound effect on the phenotypes displayed. On the other hand, the researchers screened additional cataract patients unrelated to the original family and discovered mutations in six more loci spread across the *PIKFYVE* gene. It is therefore unclear why some mutations cause cataracts and others cause corneal fleck dystrophy. The next section will report yet another novel *PIKFYVE* variant and associated phenotype.

1.4 PIKFYVE Patient

1.4.1 Clinical Phenotype

Dr. Ian MacDonald, an ophthalmologist at the University of Alberta, previously identified a mother-son patient duo with a unique retinal degeneration phenotype. The son (proband) was first referred to Dr. MacDonald at the age of 39 with complaints of visual field loss. The proband had also developed night blindness in early childhood. The patient underwent ophthalmic examination including fundoscopy, which images the inside of the back of the eye. The patient's fundus images revealed evidence of retinal depigmentation and degeneration (Fig. 1.6A). The patient also underwent fundus autofluorescence (FAF) testing, which is a non-invasive imaging technique to detect abnormal autofluorescent molecules in the retina indicative of degeneration. As shown in Fig. 1.6B, a ring of hyperfluorescence was detected in the patient, suggesting the presence of drusen deposits and/or lipofuscin in the RPE. There was no significant thinning of retinal layers observed in the patient's optical coherence tomography scan (data not shown). Moreover, the patient underwent a slit-lamp examination where a light is shone through the eye. Normally, iris pigmentation prevents light from reflecting back. However, in the patient bilateral transillumination was observed (Fig. 1.6C), indicative of depigmentation of the iris. The patient also underwent retinal functional testing by electroretinography and there was no significant light response recorded in photopic (well-lit) or scotopic (dark) conditions (Fig. 1.6D). Beyond the visual phenotype, the patient also presented with hearing loss, progressive complex migraines, and worsening neurodegeneration. The proband's mother presented with a similar phenotype of hearing and vision loss, transillumination defect, migraines, and neurodegeneration. The proband's mother eventually developed ischemic dementia, paranoid psychosis, and hallucination and passed away at the age of 62.

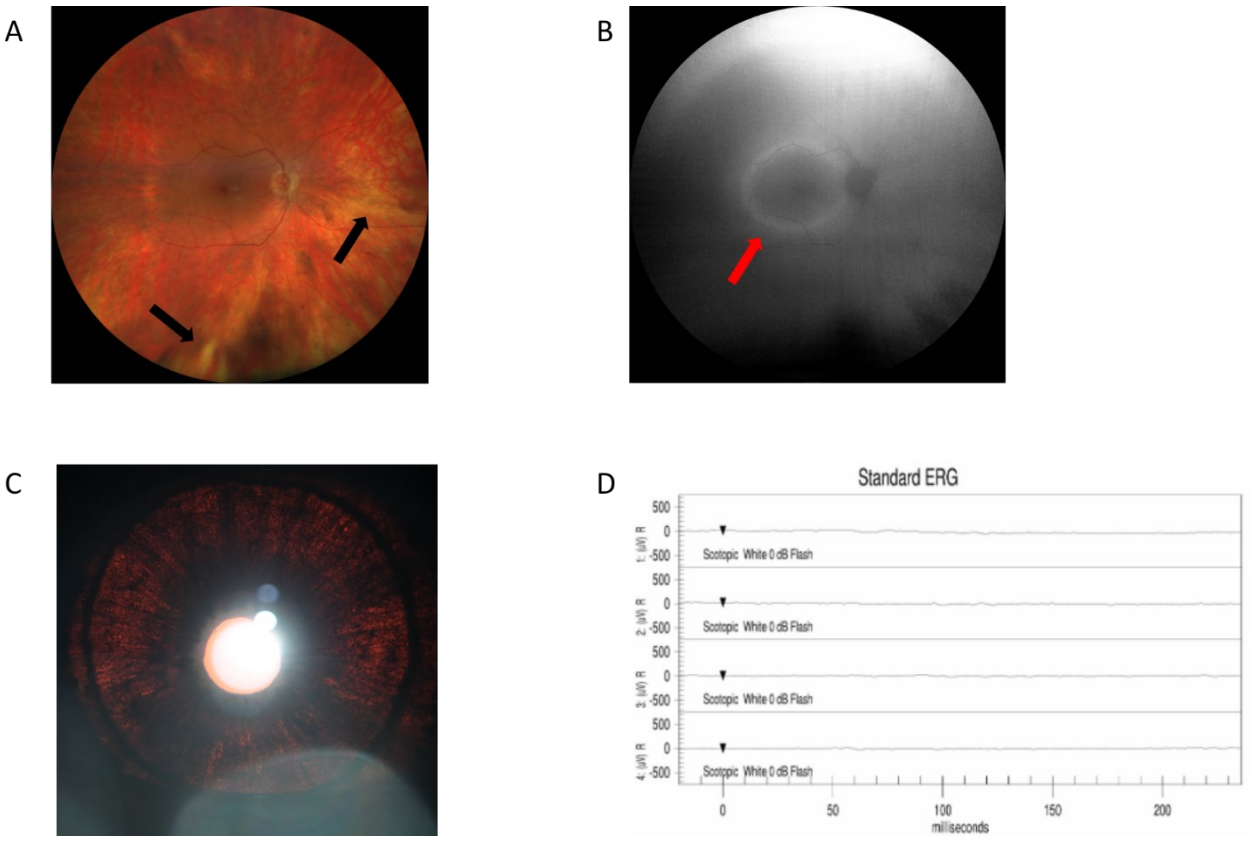

Figure 1.6 – *PIKFYVE* patient ophthalmic examination findings. (A) Fundoscopy showing retinal depigmentation and degeneration (black arrows). (B) Fundus autofluorescence showing a ring of hyperfluorescence (red arrow). (C) Slit-lamp examination showing transillumination of the iris. (D) Electroretinography (ERG) testing showing flat retinal electrical responses to light. All data was obtained by Dr. Ian MacDonald.

1.4.2 Patient Genotype

Trio whole exome sequencing (WES) could not be performed due to the mother's death. However, the proband and his father underwent WES, and it revealed a novel heterozygous missense variant in the *PIKFYVE* gene in the proband. The variant is a single base substitution that falls within the kinase domain of the PIKFYVE protein (c.5492A>G, p.(His1813Arg)). The variant was not present in the father and has not been previously reported in the literature.

Although the mother did not undergo genetic testing, we hypothesize that she carried the same variant due to the similarity in phenotype between the son and mother. The prediction results by three software Mutation Taster, Polyphen2 and SIFT were inconsistent, with the variant being predicted as benign, possibly damaging, and tolerated, respectively. Based on the current evidence, this variant is classified as a variant of unknown significance (VUS). Molecular modeling of the variant by Yuri Sergeev revealed that it alters the kinase domain conformation by shifting the first helix (Fig. 1.7).

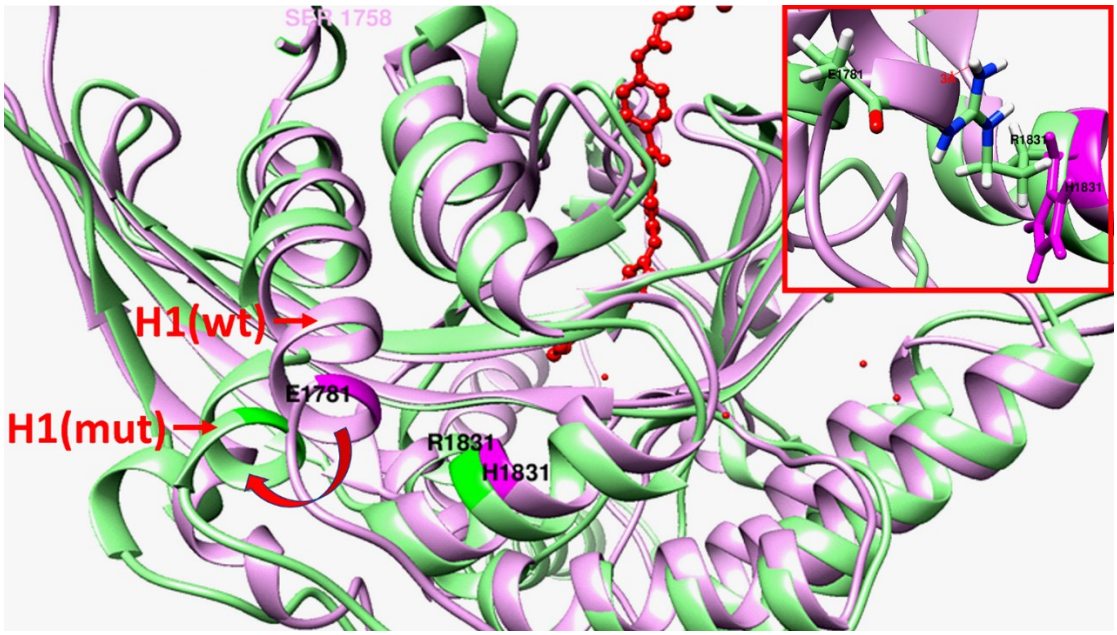

Figure 1.7 – Molecular modeling of the p.(His1813Arg) *PIKFYVE* mutation. Wildtype structure is shown in purple and mutant structure is shown in green. The patient mutation is expected to shift the first helix (H1) of the kinase domain. Molecular modeling and the figure were provided by Yuri Sergeev (National Eye Institute, USA).

1.4.3 Current Understanding

Our understanding of the mechanism of disease of *PIKFYVE* mutations is limited, and

genotype-phenotype associations are difficult to deduce due to the heterogeneity of phenotypes observed in patients with *PIKFYVE* mutations. Although it is tempting to speculate that the domain in which the mutation lies determines the phenotype, two variants of close proximity, both in the kinase domain, produce vastly different phenotypes – one associated with congenital cataracts and one with retinal dystrophy. Moreover, the nature of the mutation also seems to have little correlation with phenotype; nonsense and frameshift mutations in the early domains of the protein are tolerated and only produce a phenotype of corneal flecks while a missense mutation in the kinase domain critically impairs vision. Nonetheless, heterozygous *PIKFYVE* mutations in humans cause a largely ocular phenotype. Hence, an *in vivo* model is required to better understand the roles of *PIKfyve* in the eye. Knockout of *PIKfyve* is embryonic lethal in mice, zebrafish, and *C.elegans* (Mei et al., 2021), and therefore studying the gene *in vivo* has been difficult. Here, I utilized various precise gene editing technologies in an attempt to introduce the specific patient mutation and overcome the lethality associated with gene knockout. I chose *Danio rerio* (zebrafish) as a model organism for several advantages that will be discussed in the next section.

1.5 Zebrafish as a Disease Model

Zebrafish have become a powerful model of human disease over recent years as they provide many advantages for use in research. Zebrafish are characterized by high fecundity, generating a large number of embryos from a single breeding (Lui et al., 2019). Fertilization is external in zebrafish, allowing access to embryos as early as the one-cell stage (Lui et al., 2019). This is particularly advantageous in genetics research since embryos can be genetically manipulated at very early time points. Moreover, rapid drug screenings can be performed on zebrafish at any time point during development. Transparency of the embryos allows for

visualization of developing tissue and the monitoring of embryogenesis following genetic manipulation or drug treatment. The human and zebrafish genomes are highly conserved with 70% of disease-causing genes in humans having an ortholog in zebrafish (Lui et al., 2019), allowing for the use of zebrafish as disease models. Zebrafish are particularly advantageous for the study of eye diseases as their retinal organization closely resembles that of the human (Fig. 1.8). Moreover, unlike the rod-dominated retinas of common rodent models, zebrafish retinas consist of a 1:1 ratio of rods: cones and therefore, both rod and cone disorders may be studied in fish (Richardson et al., 2017).

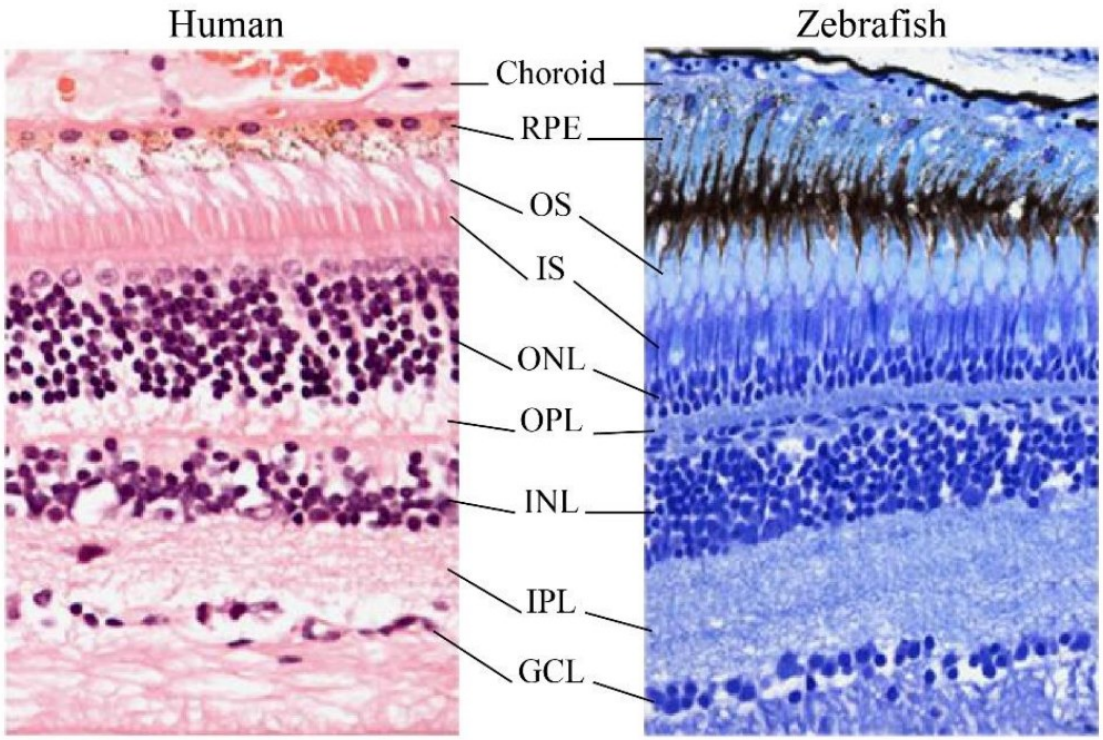

Figure 1.8 – Comparison of retinal organization in humans and zebrafish. Zebrafish retinal architecture closely resembles that of humans. RPE= retinal pigment epithelium; OS= outer segment; IS= inner segment; ONL= outer nuclear layer; OPL= outer plexiform layer; INL= inner

nuclear layer; IPL= inner plexiform layer; GCL= ganglion cell layer. Figure adapted from Richardson et al., 2017.

1.6 Precise Genome Editing

1.6.1 Homology Directed Repair

The development of Clustered Regularly Interspaced Short Palindromic Repeats (CRISPR)/Cas9 as a gene editing tool by Emmanuelle Charpentier and Jennifer Doudna has greatly advanced genetics research. Briefly, the CRISPR/Cas9 system allows for precise DNA cutting through utilizing a Cas9 endonuclease that is guided to the sequence of interest by a guide RNA (gRNA). The Cas9 binds the DNA at the protospacer adjacent motif (PAM) sequence, which is typically a three-nucleotide sequence consisting of any base followed by two guanines (NGG). The endonuclease then generates a double-stranded break (DSB) three bases upstream of the PAM site. DSBs generated by the CRISPR/Cas9 system may be repaired by one of three mechanisms: homology directed repair (HDR), non-homologous end joining (NHEJ), or microhomology-mediated end joining (MMEJ). NHEJ is active throughout all stages of the cellular cycle and its repair is fast, making it the prominent pathway in most cells (Yang et al., 2020). In NHEJ, the broken DNA strands are ligated regardless of sequence homology. Therefore, NHEJ results in random mutations that may include insertions or deletions at the site of the DSB (Yang et al., 2020). In MMEJ, small homologous sequences on either side of the break are annealed and ligated, resulting in a precise deletion (Yang et al., 2020). HDR, on the other hand, is restricted to cells in the S and G2 phase and it relies on an undamaged sister chromatid to repair the DSB. Repair may also be mediated by an exogenous DNA template that is provided to the cell (Yang et al., 2020). Combining HDR and CRISPR/Cas9, precise edits can

be introduced in the DNA by providing cells with a DNA template encoding the desired DNA change.

1.6.2 Base Editing

The use of an exogenous DNA template encoding the desired edit can allow for the introduction of specific mutations into the genome through HDR. However, since HDR relies on the introduction of DSBs, DSB-associated byproducts such as indels, translocations, and rearrangements are a constant concern (Rees et al., 2018a). Moreover, HDR is in competition with NHEJ and MMEJ and unfortunately, in most cells (especially those that are not dividing), NHEJ is the prominent DNA repair pathway, decreasing the efficiency of HDR (Rees et al., 2018a). 64% of disease-causing genetic variants are linked to a single base substitution (Fig. 1.9) and therefore precise introduction of a single point mutation to either mimic patient mutations in animal models or correct them in the clinic is of utmost importance. In 2016, Komor et al., developed a technology termed base editing that allows for single base substitutions without the use of an exogenous template, or creation of DSBs and DSB-associated byproducts.

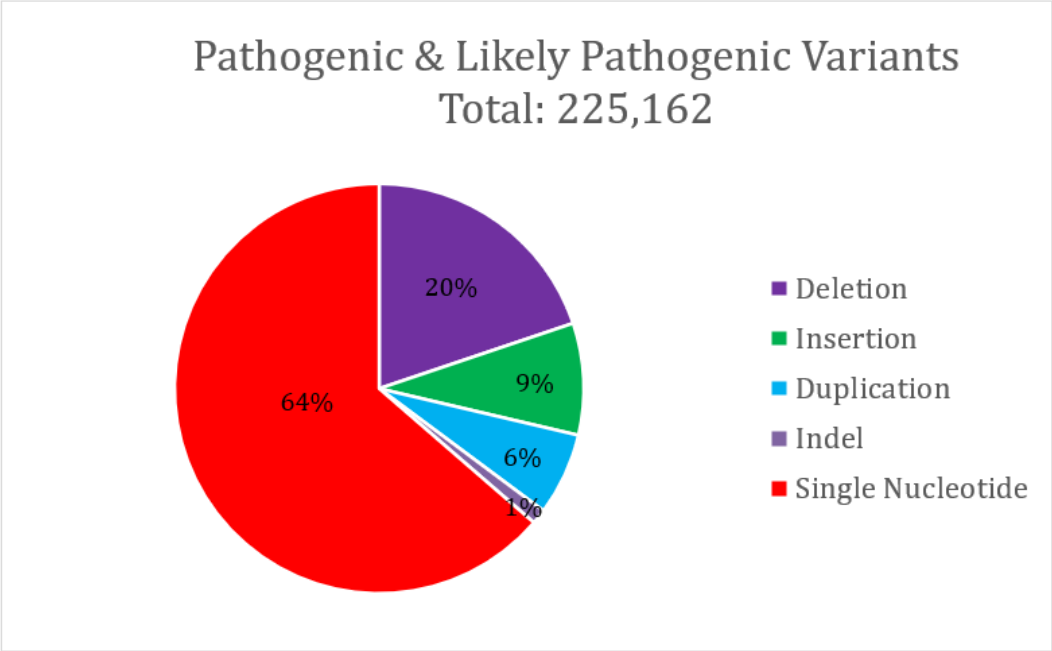

Figure 1.9 – Nature of pathogenic and likely pathogenic variants. Data pulled from ClinVar April 2023.

1.6.2.1 Cytosine Base Editing

The original class of base editors (BE1) utilized a catalytically dead Cas9 (dCas9) that does not cut the DNA but retains its DNA-binding ability (Komor et al., 2016). The dCas9 is fused to a cytosine deaminase, an enzyme that catalyzes the conversion of cytosine into uracil, which is analogous to thymine in base-pairing properties and is read by DNA polymerase as a thymine (Komor et al., 2016). Upon hybridization of the gRNA to the complementary DNA sequence, the opposite strand of the protospacer sequence is unpaired (the first 11 nucleotides), forming a single-stranded region called the R-loop (Komor et al., 2016). Single-stranded DNA within the R-loop makes cytosine residues accessible for deamination by the cytosine deaminase (Komor et al., 2016). Unfortunately, uracil residues are rapidly marked by uracil glycosylases and removed from the DNA by base excision repair (BER) (Komor et al., 2016). The second

generation of base editors (BE2) addresses this limitation by fusing an uracil glycosylase inhibitor (UGI) to the C-terminus of the BE1 fusion protein (Komor et al., 2016), ensuring that uracil does not get excised rapidly from the DNA. The editing remains on one strand of the DNA and therefore, Komor et al., developed the third generation of base editors (BE3) to increase editing efficiency by aiming to mutate both strands of the DNA. BE3 utilizes Cas9 nickase (nCas9) which only cuts one of the two DNA strands. DNA nicks are known to activate mismatch repair, therefore increasing the chance of the unedited strand being mutated to match the base edited strand (Komor et al., 2016).

1.6.2.2 Adenine Base Editing

Cytosine to thymine point mutations only make up a subset of disease-causing single base substitutions and therefore Gaudelli et al., developed adenine base editing (ABE) to create adenine to guanine single base substitutions (Gaudelli et al., 2017). The authors engineered a heterodimeric protein that incorporates nCas9 and a mutated *E. coli* TadA deoxyadenosine deaminase (Rees et al., 2018a). Directed to the sequence of interest by the gRNA, the heterodimeric protein catalyzes the deamination of an adenine residue within the exposed, single-stranded R-loop into an inosine (Rees et al., 2018). During DNA replication, inosine is read by DNA polymerases as a guanine, allowing for adenine to guanine single base substitutions with ABE (Gaudelli et al., 2017). Different versions of ABE carrying various mutations in the TadA deoxyadenosine deaminase have been created to increase editing efficiency and manipulate the location of the adenosine deaminated with respect to the PAM (Rees et al., 2018a, Gaudelli et al., 2017, Carrington et al., 2020). Moreover, online tools such as the ACEofBases have been created to simplify gRNA design and improve targeting and editing efficiency of base editors (Cornean et al., 2022, Hwang et al., 2018).

1.6.3 Prime Editing

While the development of base editing enables researchers to model and correct point mutations without generating double stranded breaks in the DNA, the technology is unfortunately limited by the four transition mutations previously described. Base editing cannot generate transversion mutations in which a two-ring purine is changed into a one-ring pyrimidine or vice versa. As a result, base editing is not applicable in the correction of some disease-causing mutations such as the nucleotide change causing sickle cell anemia (GAG → GTG) (Anzalone et al., 2019). Moreover, base editing only allows for single base substitutions and thus, correction of disease-causing small insertions and deletions is not possible (Anzalone et al., 2019). Therefore, a precise gene editing technology capable of introducing all 12 possible point mutations as well as small insertions and deletions without the introduction of double-stranded breaks is critical for enhancing the breadth of diseases that could be treated by gene therapy.

In 2019, Anzalone et al developed a "search and replace" technology termed prime editing that significantly advances the field of genome editing by eliminating most of the limitations and concerns associated with other gene editing technologies. By combining the power of reverse transcription and catalytically inactive endonucleases, Anzalone et al created a system that is capable of precisely copying genetic changes into DNA (Fig. 1.10). Consistent between all versions of prime editors is the prime editing guide RNA (pegRNA), a specialized gRNA that both directs an endonuclease/reverse transcriptase fusion protein to the sequence of interest and encodes the desired sequence change. The pegRNA includes the spacer sequence, which is complementary to the DNA target site and hybridizes with it, and the 3' extension. The 3' extension is made up of two sequences: first, the primer binding site (PBS) which hybridizes to the nicked DNA strand and acts as a primer for the reverse transcriptase; and second, the

reverse transcriptase template (RTT) which encodes the desired edit (Scholefield and Harrison, 2021). The spacer and 3' extension sequences are joined by a scaffolding sequence.

The first generation of prime editors (PE1) consists of an M-MLV reverse transcriptase (RT) fused to a mutated Cas9 nickase (H840A) through the C-terminus (Scholefield and Harrison, 2021). In this technique, the spacer sequence of the pegRNA binds to the target strand, opening the DNA into an R-loop. The mutated nickase then cuts the non-complementary DNA strand three bases upstream of the PAM site. The exposed DNA flap (called a 3' flap) binds to the PBS of the pegRNA, forming a DNA-RNA hybrid. This serves as a primer for RT to start reverse transcribing the pegRNA RTT and extending the 3' DNA flap. The newly synthesized 3' flap replaces the unedited 5' flap, which is degraded by the endogenous endonuclease FEN1, resulting in the integration of the desired edit into the genome (Scholefield and Harrison, 2021). The second generation of prime editors (PE2) consists of similar components and mechanisms, but the M-MLV RT carries a series of mutations that increase its thermostability, substrate affinity, and processivity (Anzalone et al., 2019). Because only one of the two DNA strands is edited, both PE1 and PE2 generate a heteroduplex region in the DNA, creating a mismatch between the two DNA strands (Scholefield and Harrison, 2021). Ideally, mismatch repair enzymes would edit the wildtype DNA strand to match the desired edit, but it is also possible for the edit to be reverted to wildtype. Therefore, the third generation of prime editors (PE3) was created to address this limitation and increase editing efficiency. PE3 utilizes an additional standard gRNA that nicks the complementary strand, promoting the editing of the wildtype strand rather than the mutated strand during mismatch repair (Scholefield and Harrison, 2021). While increased editing efficiency is observed with PE3, an increase in indel formation is also common since both strands are nicked and therefore DSBs are generated (Scholefield and

Harrison, 2021). A revised system, PE3b, addresses this limitation by creating a gRNA that only recognizes the complementary DNA strand after prime editing has occurred, decreasing indel formation (Scholefield and Harrison, 2021).

Since its development, prime editors have been rapidly employed by researchers to both create and correct various patient mutations in models. Thus far, prime editing has been successful in human cells (Anzalone et al., 2019, Petri et al., 2021), mice (Jang et al., 2021, Lin et al., 2021, Liu et al., 2020), plants (Ren et al., 2021, Walton et al., 2020, Jiang et al., 2020), and zebrafish (Petri et al., 2021). One limitation arising with prime editing is the restriction due to the PAM site; not all disease-causing mutations have a PAM site that fits pegRNA design guidelines. Walton et al., developed a near PAM-less Cas9 nickases (SpG and SpRY) that loosen the restriction on the PAM site sequence (Walton et al., 2020). Another limitation of prime editing is the complexity of pegRNA design. The success and efficiency of prime editing are largely dependent on the pegRNA and thus, tools have been developed to aid in the pegRNA design process (Standage-Beier et al., 2021, Hsu et al., 2020).

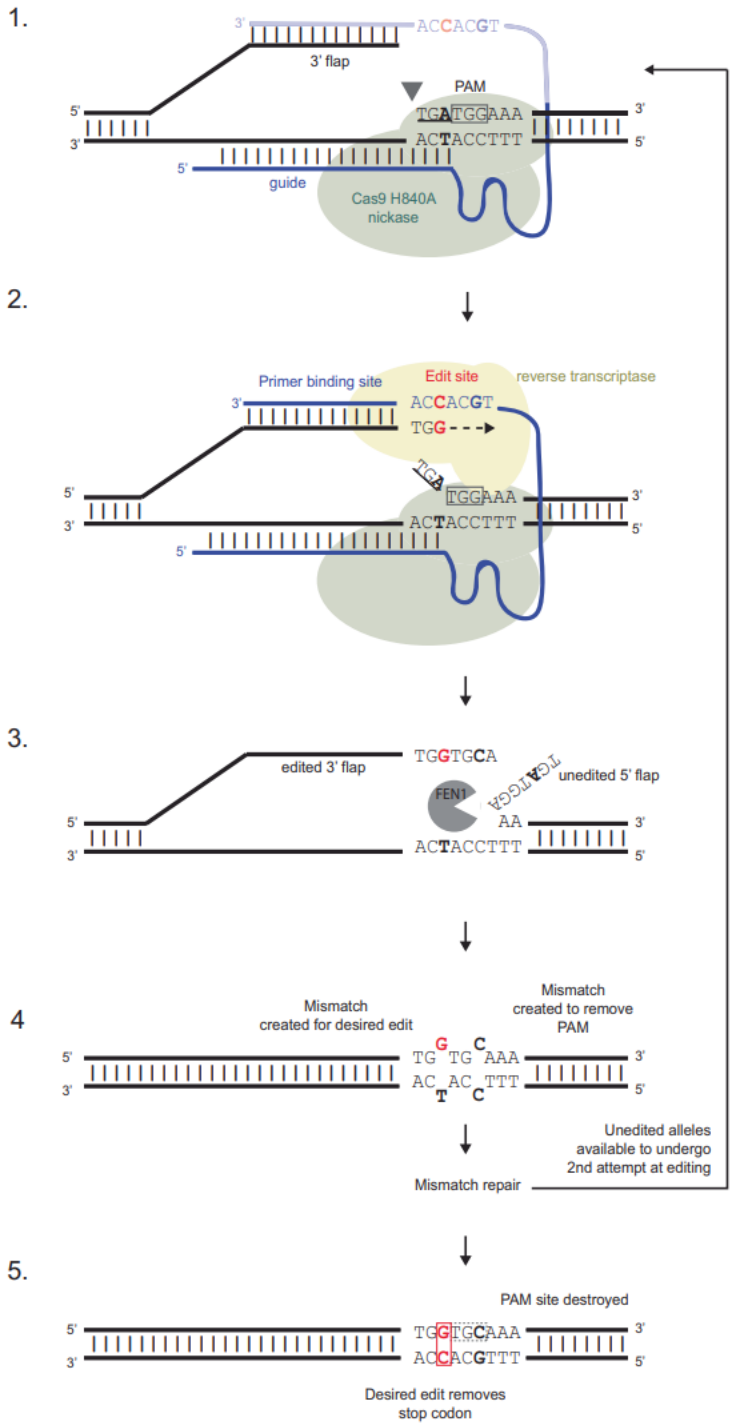

Figure 1.10 – Prime editing overview. Figure from Scholefield and Harrison, 2021 showing the five steps of prime editing**.** 1. The nCas9/reverse transcriptase fusion protein binds the target

region and nicks the DNA three bases upstream of the PAM site creating a 3' flap. 2. The 3' flap hybridizes with the primer binding site of the pegRNA and acts as a primer for reverse transcription initiation which occurs using the reverse transcriptase template of the pegRNA. 3. The edited 3' flap replaces the unedited 5' flap, which is excised by the cellular endonuclease FEN1. 4. Editing results in a mismatch between the edited and unedited DNA strands. 5. Mismatch repair enzymes either mutate the unedited strand to match the edit or reverse the sequence back to wildtype in which case, the process starts over.

1.7 Purpose

The primary goal of this thesis was to provide the first characterization of PIKfyve function in the retina, particularly in the retinal pigment epithelium. As previously discussed, phenotypes associated with *PIKFYVE* mutations in humans are heterogenous and typically present in the eye. While *in vitro* work has highlighted a role of PIKfyve in various cellular pathways including endocytosis, phagocytosis, autophagy, and melanogenesis, little is known about its roles *in vivo* and the mechanism through which mutations in the gene result in an ocular phenotype. The knockout of *PIKfyve* is embryonic lethal in zebrafish, mice, and *C.elegans* and therefore elucidating ocular disease mechanisms has been difficult. Zebrafish possess one highly conserved ortholog of the *PIKfyve* gene, and they are excellent models for genetic and ocular research. Thus, I sought to characterize the roles of PIKfyve in the zebrafish retina.

Hypothesis: PIKfyve is essential in the RPE through involvement in phagocytosis, lysosomal function, melanosome biogenesis, and autophagy, and therefore, its loss results in disrupted retinal homeostasis which negatively affects photoreceptor function and health.

My first aim was to use CRISPR/Cas9 mutagenesis to target the kinase domain of the zebrafish Pikfyve protein. In the patient identified by Dr. MacDonald, the mutation falls within the kinase domain and is associated with a retinal dystrophy phenotype. In the patients identified by Mei et al, mutations in the kinase domain are associated with congenital cataracts. Thus, I chose to target the kinase domain as it is associated with significant disease phenotypes in humans that are poorly characterized mechanistically. I sought to introduce a loss of function mutation to knockout or knockdown the gene in zebrafish and study the resultant effect on the eye. I examined retinal electrical function and retinal structure of the CRISPR-injected fish to elucidate a disease mechanism for Pikfyve loss.

My second aim was to study the effects of Pikfyve pharmacological inhibition on the zebrafish retina. Apilimod is a potent and specific inhibitor of PIKfyve that has been in clinical trials for cancer and neurodegeneration. Surprisingly, the effects of the drug on vision are unexplored and the inhibitor has never been tested on zebrafish before. Thus, I sought to treat zebrafish larvae and adults with apilimod and analyze retinal electrical function and structure. I utilized electroretinography, electron microscopy, and confocal analysis to characterize apilimod-treated zebrafish.

My third aim was to utilize precise gene editing technologies to introduce the variant identified by Dr. MacDonald into the zebrafish *pikfyve* gene. Knockout of the gene is embryonic lethal and therefore, I sought to create a patient mimic line that would survive to adulthood and allow us to not only confirm the causative nature of the variant but also study its progressive effect on the retina. I developed methods for using homology directed repair, prime editing, and base editing, each of which could potentially create the analogous patient mutation into zebrafish.

CHAPTER TWO: MATERIALS AND METHODS

2.1 Animal Ethics

Approval for this study was obtained from the Animal Care and Use Committee: Biosciences, under protocol AUP 1476.

2.2 Zebrafish Care

Zebrafish were cared for by the Health Sciences Laboratory Animal Services (HSLAS) at the University of Alberta. Stock embryonic media (EM) was prepared by combining 17.5 g NaCl, 0.75 g KCl, 2.9 g $CaCl_2$-$2H_2O$, 0.41 g KH_2PO_4, 0.142 g Na_2HPO_4 anhydrous, 4.9 g $MgSO_4$-$7H_2O$ in 1 liter of Milli-Q water, vacuum filtered, and stored at 4°C. Working EM solution was prepared fresh every week by combining 50 mL stock EM, 2 mL 500X sodium bicarbonate, and Milli-Q water to 1 liter, and stored at room temperature. Zebrafish larvae were grown in working EM solution at 28.5°C until 5-days post fertilization (dpf) at which point they were transferred to 3.5-liter tanks at a density of 30 fish/tank in the HSLAS aquatics facility. Tank density was lowered to 15 fish/tank once fish reached adulthood to optimize living and feeding conditions. Zebrafish were fed three times as larvae and juveniles and twice as adults with a combination of rotifers and Ziegler dry food. Zebrafish were kept in a 14:10 hour light/dark cycle. Zebrafish of the AB line were used in all experiments throughout this thesis. Tricaine mesylate (TMS) was used to anesthetize and euthanize zebrafish. Stock TMS was prepared by combining 400 g tricaine powder (3-amino benvoic acidethylester, MS222), 97.9 mL DD H_2O, 2.1 mL 1M Tris pH 8 and stored at -20°C. A 4.2% working TMS solution was prepared with Milli-Q water for zebrafish anesthesia.

2.3 CRISPR/Cas9 Mutagenesis

The CHOPCHOP web tool (https://chopchop.cbu.uib.no) and the Integrated DNA Technologies (IDT) Custom Alt-R CRISPR-Cas9 guide RNA tool were used to design CRISPR RNAs (crRNAs). Two crRNAs targeting the third and fourth exons of the kinase domain of the *Danio rerio pikfyve* gene were designed. The first crRNA targets the sense strand of exon 38 while the second crRNA targets the antisense strand of exon 39. Co-injection of the two crRNAs generates two double stranded breaks that are ~268 nucleotides apart.

Alt-R ® CRISPR-Cas9 crRNAs (Table 2.1), Alt-R ® CRISPR-Cas9 tracrRNA, and Alt-R™ S.p. Cas9 Nuclease V3 were ordered from IDT. RNAs were resuspended in RNase-free 1X Tris-EDTA buffer to a concentration of 100 µM. To anneal, 5 µL tracrRNA and 5 µL crRNA (100 µM ea.) were heated at 95°C for 5 minutes and then gradually cooled to room temperature in a thermocycler at 0.1°C/second. Annealed RNA duplexes were stored at -20°C. Injection mixtures consisted of 5 µM each RNA duplex (diluted in IDT duplex buffer) and 5 µM Cas9 (diluted in 1X RNase-free PBS). 100-200 zebrafish embryos were injected at the single-cell stage with 2 nL of the injection mixture. To prepare injection needles, filamented borosilicate glass capillary tubes (OD 1.20mm, ID 0.90 mm; Sutter Instruments, Novato, USA) were pulled on a Sutter micropipette puller. Injections were performed under an Olympus stereo microscope using a WPI micromanipulator and pneumatic pump (World Precision Instruments, Sarasota, USA). Injected embryos and uninjected siblings were grown in a 28.5°C incubator in EM for 1-6 dpf prior to genotyping and analysis or transfer to the fish facility.

Table 2.1 – Sequence of crRNAs used to target *pikfyve, tyr,* and *slc45a2* genes.

crRNA	**Sequence (5' → 3')**
PIK5crExon3 (crispant, ABE)	AGAGUUCCAUAAAAUGCGGGGUUUUAGAGCUAUGCU

PIK5crExon4 (crispant)	UGUGAUGUACGUAAAGUAGUGUUUUAGAGCUAUGCU
PIKfyveExon38 (HDR)	CUGAAGAGUUCCAUAAAAUGGUUUUAGAGCUAUGCU
Tyr(W273*)NAN (CBE)	CCUUCCAGGAUGAGAACACAGUUUUAGAGCUAUGCU
Slc45a2(W121*) (CBE)	GGCCCCAUGACGACCUACAGGUUUUAGAGCUAUGCU

2.4 Homology Directed Repair

Like CRISPR/Cas9, homology directed repair (HDR) involves a Cas9 protein that breaks both strands of the DNA and a crRNA that directs the Cas9 to the sequence of interest. In addition, HDR involves the co-injection of a nucleotide template that is complementary to the DNA sequence, except for the desired edit. I used HDR in an attempt to introduce the analogous *PIKFYVE* patient mutation into zebrafish and create a patient mimic mutant line.

The human and zebrafish *PIKfyve* genes share a 70% sequence homology (Boisset et al., 2008). The human *PIKFYVE* gene is located on chromosome 2 while the zebrafish *pikfyve* gene is on chromosome 9. The histidine encoded by the CAT codon mutated to CGT in the human patient is conserved between humans and zebrafish, and therefore I targeted the same residue. In humans, the patient mutation is c.5942A or p.His1831, which correlates to c.5530A or p.His1833 in zebrafish. To design the HDR components, I used the IDT Alt-R HDR Design Tool (https://www.idtdna.com/site/order/designtool/index/HDRDESIGN) and incorporated recommendations from Prill and Dawson 2020. The crRNA sequence is shown in Table 1 and directs the Cas9 to cut the DNA five base pairs downstream of the adenine base of interest. According to the Prill and Dawson 2020 recommendations, I designed the DNA template to be single stranded and asymmetrical with homology arms of 18-400 nucleotides long. The single-stranded oligonucleotide (ssODN) was 198 nucleotides long to align template ends with regions

in the surrounding introns and prevent undesired changes in the exon sequence. The ssODN carried three single base changes compared to the wildtype DNA sequence: an A>G to mimic the patient mutation, and two silent mutations (G>A and C>T) to prevent rebinding of the crRNA after editing has occurred and to introduce an XmnI restriction enzyme cut site. The introduction of the XmnI cut site allows for easier detection of successful HDR as described in section 2.4. The crRNA, Cas9, and ssODN were ordered from IDT.

crRNA and tracrRNA were annealed according to the protocol described in section 2.3. I experimented with varying concentrations of the injected components as summarized in Table 2.2. I added the small molecule inhibitor NU7441 (Stem Cell Technologies, Catalog #74082) to inhibit non-homologous end joining (NHEJ) and direct the cells to repair Cas9-induced DNA damage through HDR. Injecting the inhibitor versus adding it to embryonic media produces mixed results according to the literature (Prill and Dawson, 2020) and therefore I attempted both approaches (Table 2.2). 2 nL of the final mixture Table 2.2 was injected into zebrafish embryos at the single-cell stage according to the protocol described in section 2.3. Injected embryos were either placed in embryonic media or embryonic media containing 2 μM NU7441. Embryonic media was changed daily, and the inhibitor was removed after the first day following injections. Injected and uninjected siblings were grown in a 28.5°C incubator until 5-6 dpf, at which point surviving embryos were transferred to the fish facility.

Table 2.2 – HDR microinjection mixtures. Summary of injection mixture components and their respective concentrations attempted for HDR. *NU7441 was added to the embryonic media in treatment 2 and not injected.

Experiment A	**Cas9 mRNA**	**gRNA duplex**	**Template**	**NU7441**
Treatment 1	300 ng/uL	50 ng/uL	30 ng/uL	20 ng/uL
Treatment 2*	300 ng/uL	50 ng/uL	30 ng/uL	0.80 ng/uL

Treatment 3	300 ng/uL	50 ng/uL	-	-
Treatment 4	300 ng/uL	50 ng/uL	30 ng/uL	-
Treatment 5	-	-	-	-
Experiment B				
Treatment 1	500 ng/uL	75 ng/uL	25 ng/uL	20 ng/uL
Treatment 2*	500 ng/uL	75 ng/uL	25 ng/uL	0.80 ng/uL
Treatment 3	500 ng/uL	75 ng/uL	-	-
Treatment 4	500 ng/uL	75 ng/uL	25 ng/uL	-
Experiment C				
Treatment 1	800 ng/uL	170 ng/uL	-	-
Treatment 2	800 ng/uL	170 ng/uL	60 ng/uL	-
Treatment 3	800 ng/uL	170 ng/uL	60 ng/uL	20 ng/uL

2.5 Prime Editing

2.5.1 pegRNA Design

Success of prime editing is largely based on the design of the pegRNA. Therefore, I explored multiple tools to design and check the pegRNA sequence including PrimeDesign, PINE-CONE, and pegFinder. Moreover, I incorporated suggestions from the Billon lab protocol and the original prime editing paper (Billon et al., 2021, Anzalone et al., 2019). The length of both the PBS and the RTT has a critical effect on prime editing efficiency and literature shows that a PBS of 13-16 nucleotides and a RTT of 10-16 nucleotides provide the greatest editing efficiency. However, the region of interest in the zebrafish *pikfyve* gene did not possess a PAM site that satisfies pegRNA design requirements. To address this, I devised two solutions. First, targeting the antisense strand, which has a PAM fitting pegRNA requirements, and second, using an SpRY nCas9 prime editor, which is a near PAM-less nCas9 and gives more leeway in pegRNA design.

The pegRNA sequences used are shown in Table 2.3. First, a PAM site was identified 14 nucleotides downstream of the base of interest. The 20 nucleotides upstream of the PAM site

make up the spacer sequence. The nCas9 fusion protein nicks the DNA three bases upstream of the PAM site. The 13 nucleotides upstream of the nicking site form the PBS and the 13 nucleotides downstream of the PAM site form the RTT. Next, the desired modification was applied to the RTT so that the sequence carried the adenine to guanine single base substitution. The 3' extension sequence is therefore the RTT-PBS sequence. Cloning handles were added to the fragments and DNA fragments and their reverse complements were ordered from IDT as single-stranded DNA oligos.

2.5.2 Golden Gate Cloning

I used golden gate cloning to assemble the pegRNA DNA fragments in the correct order and orientation in a BB10 vector plasmid, generously gifted by the Childs lab (University of Calgary). BB10 is an assembly vector that contains a red fluorescent protein (RFP) gene, hence the bacteria transfected with the plasmid appear pink if the RFP gene is uncut. I first digested the BB10 plasmid with BsaI-HFv2 (New England Biolabs, Catalog #R3733) to linearize and excise the RFP gene. 5 µL 10X rCutSmart buffer, 1 µg BB10 plasmid, 0.5 µL BsaI-HFv2 enzyme and water to 50 µL were combined. 1.0 µL shrimp alkaline phosphatase (rSAP, NEB, Catalog #M0371S) was added to dephosphorylate the plasmid and the reaction was incubated at 37°C for 1 hour in a thermocycler. The reaction was then run on a 1% low-melting point agarose gel in 1X tris-acetate EDTA (TE) buffer and the 2.2 kb band was excised and purified using the GeneJet Gel Extraction Kit (ThermoFisher, Catalog #KO691). The purified, linearized plasmid was stored at -20°C until further use.

Next, the forward and reverse oligonucleotides were annealed to create double stranded DNA fragments. Three separate reactions were set up, one for each of the spacer, scaffold, and 3' extension sequences of the pegRNA. To anneal oligonucleotides, a 10 µL reaction containing 4

μM forward and 4 μM reverse oligos for each pegRNA component was set up and heated at 95°C for 3 minutes, then gradually cooled to 22°C at 0.1°C/s in a thermocycler. The annealed oligonucleotide duplexes were then phosphorylated to facilitate assembly in the BB10 plasmid vector. A reaction mixture containing 6.25 μL oligonucleotide duplex (4 μM), 0.5 μL T4 polynucleotide kinase (PNK, ThermoFisher, Catalog #EK0031), 5 μL 5X T4 DNA Ligase Buffer, and 13.25 μL water was assembled for each duplex and incubated at 37°C for 1 hour. Annealed and phosphorylated oligonucleotides (at a final concentration of 1 μM) were stored at -20°C.

The final step was to ligate the annealed, phosphorylated oligonucleotides and assemble into the linearized, pure BB10 plasmid. The assembly reaction contained 2 μL 5X T4 Ligase Buffer, 10-30 ng dephosphorylated, purified plasmid, 0.5 μL T4 DNA Ligase (ThermoFisher, Catalog #EL0011), 1 μL annealed scaffold duplex (1 μM), 1 μL annealed spacer duplex (1 μM), 1 μL annealed 3' extension duplex (1 μM), and water to 10 μL. A negative control assembly reaction was prepared containing everything but the oligonucleotide duplexes. The assembly reactions were incubated at room temperature for 10 minutes or in a thermocycler cycling 8 times between 16°C for 5 minutes and 37°C for 5 minutes. The ligated plasmids were stored at -20°C.

Table 2.3 – Golden gate cloning DNA fragments and BB10 primers.

Fragment/Primer Name	Sequence (5' → 3')	Tm (°C)
SpacerTopA	CACCGGATCTCCTCCCGCATTTTAGTTTT	62.1
SpacerBottomA	CTCTAAACAAAATGCGGGAGGAGATCC	59.2
ExtensionTopA	GTGCTTACGGAATTCTTCTCCTCCCGCATT	63.3
ExtensionBottomA	AAAAAATGCGGGAGGAGAAGAATTCCGTAA	60.2
5'PhosScaffoldTop	AGAGCTAGAAATAGCAAGTTAAAATAAGGCTAGTC CGTTATCAACTTGAAAAAGTGGCACCGAGTCG	67.9

5'PhosScaffoldBottom	GCACCGACTCGGTGCCACTTTTTCAAGTTGATAACGGACTAGCCTTATTTTAACTTGCTATTTCTAG	68.1
601F BB10_FWD_A	GAGGGCCTATTTCCCATGATT	54.6
602F BB10_FWD_B	GACTATCATATGCTTACCGT	48.9
603F BB10_FWD_A_T7P	TAATACGACTCACTATAGGGGAGGGCCTATTTCCCATGATT	64.6
604F BB10_FWD_B_T7P	TAATACGACTCACTATAGGGGACTATCATATGCTTACCGT	62.0
601R BB10_REV	GGGAAACGCCTGGTATCTTTA	54.6
605F pegRNABB10_T7	TAATACGACTCACTATAGGGCGATACAAGGCTGTTAGAGAGATAA	63.5
606F pegRNABB10 FWD	CGATACAAGGCTGTTAGAGAGATAA	53.9
606R pegRNABB10 REV	GATTGAATGCGGGAGGAGAA	54.8
607F T7Promoter_FWD	TAATACGACTCACTATAGGG	47.5
Spacer+T7P Top	CACCGTAATACGACTCACTATAGGATCTCCTCCCGCATTTTAGTTTT	65.1
Spacer+T7 Bottom	CTCTAAAACTAAAATGCGGGAGGAGATCCTATAGTGAGTCGTATTAC	63.1

2.5.3 Bacterial Transfection

One Shot™ TOP10 Chemically Competent *E. coli* (Invitrogen, Catalog #C404010) stored at -80°C were thawed on ice; then 16.5 µL bacterial cells and 2 µL ligated plasmid mix were combined and incubated on ice for 30 minutes. The mixtures were next heat shocked at 42°C for 30 seconds in a water bath to facilitate uptake of the plasmid by creating pores in the bacterial membranes and then placed back on ice for 2 minutes. Next, 250 µL of S.O.C Medium (Invitrogen, Catalog #15544034) was added, and the reactions were incubated at 37°C for one hour in a shaker at 300 rpm. 50-100 µL of the reaction mixture was plated on carbenicillin-

containing (100 µg/mL) luria broth (LB) plates and incubated at 37 °C overnight. The next day, individual colonies were picked from the plate using a sterile pipette tip and inoculated into liquid LB broth containing 100 µg/mL carbenicillin in culture tubes. Culture tubes were incubated at 37°C in a shaker overnight and then placed at 4°C for storage. I performed minipreps to isolate the assembled plasmid from successfully transfected bacteria using the QIAprep Spin Miniprep Kit (Qiagen, Catalog #27104).

2.5.4 *in vitro* Transcription

The BB10 plasmid does not contain a T7 promoter site and therefore, I added a T7 promoter to the assembled plasmid to allow for its *in vitro* transcription. I used a series of two PCR amplification reactions - the first to amplify the pegRNA sequence and the second to add a T7 promoter upstream of the pegRNA spacer sequence since attempting both steps in one PCR reaction was not successful. The assembled BB10-pegRNA vector was digested with BsaI-HFv2 as described in section 2.5.3. Here, the smaller gel band containing the pegRNA sequence was purified with the GeneJet Gel Extraction Kit (ThermoFisher, Catalog #KO691) and the purified DNA was used as the template for the first PCR amplification. A 100 µL PCR reaction was prepared by combining 20 µL 1X GoTaq Green Buffer, 2 µL nucleotide mix (1 mM each), 8 µL #601F forward primer, 8 µL #601R reverse primer, 0.5 µL GoTaq Polymerase, 2 µL purified DNA, and water to 100 µL. The reaction was incubated in a thermocycler according to the protocol shown in Figure 2.1. The PCR product was gel purified and the purified DNA was used as the template for the second PCR amplification. Here, primers complementary to the pegRNA spacer sequence with a T7 promoter site upstream of the pegRNA spacer sequence were used. A 100 µL PCR reaction was prepared by combining 20 µL 1X GoTaq Green Buffer, 2 µL nucleotide mix (1 mM each), 8 µL #603F forward primer, 0.5 µL GoTaq Polymerase, 2 µL

purified DNA, and water to 100 µL and incubated according to the protocol shown in Figure 2.1. The PCR product was gel purified and DNA was sent for Sanger Sequencing to confirm the correct sequence was produced.

Following T7 pegRNA sequence confirmation, I used the MEGAshortscript T7 Transcription Kit (Thermofisher #AM1354) to transcribe the pegRNA. A reaction containing 2 µL T7 10X Reaction Buffer, 2 µL T7 ATP Solution (75 mM), 2 µL T7 CTP Solution (75 mM), 2 µL GTP Solution (75 mM), 2 µL T7 UTP Solution (75 mM), <8 µL template DNA (purified PCR product), 2 µL T7 Enzyme Mix, and nuclease-free water to 20 µL was set up and incubated at 37°C for 2 hours. Next, 1 µL TURBO DNase was added to remove residual DNA template and the reaction was incubated at 37°C for 15 minutes. To terminate transcription and recover RNA, I first attempted alcohol precipitation. 115 µL nuclease-free water and 15 µL sodium acetate (3 M) was added to the reaction and mixed thoroughly. To precipitate RNA, 2 volumes of 100% ethanol were added, and the mixture was chilled at -20°C for 30 minutes. The mixture was then centrifuged at 4°C for 15 minutes at maximum speed (>10,000 x g) to pellet the RNA. A clear pellet forms, which is then resuspended in nuclease-free water and stored at -20°C for short-term use and -80°C for long-term storage. In some cases, RNA purification was carried out with the Monarch RNA Cleanup Kit (NEB #T2040S). 100 µL RNA Cleanup Binding Buffer was added to the 50 µL transcription reaction. Next, 150 µL of 100% ethanol was added to the sample and mixed by pipetting. The sample was loaded onto a column and spun for 1 minute at 16,000 x g. The flow-through was discarded and 500 µL RNA Cleanup Wash Buffer was added. The sample was spun for 1 minute and the flow-through discarded. This step was repeated before the column was transferred to a clean, RNase-free 1.5 mL microfuge tube and RNA was eluted

with 6-20 µL of nuclease-free water and spinning for 1 minute at 16,000 x g. RNA concentration was measured with a Nanodrop and the remaining sample stored at -20°C.

Since the prime editor nCas9-RT protein is not sold commercially, I synthesized *nCas9-RT* mRNA using *in vitro* transcription. BB11 – pCMV-PE2 and BB23 – pCMV-PE2 SpRY-P2A-GFP plasmids were generously gifted by the Childs lab (University of Calgary). Both plasmids encode the nCas9-RT sequence, but BB11 encodes an SpG-nCas9 which requires an NGG PAM site while BB23 encodes a SpRY-nCas9 which is near-PAMless with a preference for NAN and NGN PAM sites (Ren et al., 2021). Both plasmids contained a T7 promoter and therefore I used the HiScribe T7 ARCA mRNA Kit (NEB #E2060S) to synthesize mRNA. Plasmids were first linearized with EcoRI (ThermoFisher, Catalog #ER0271) by combining 2 µL 10X Buffer EcoRI, 1 µg plasmid DNA, 1 µL EcoRI restriction enzyme, and water to 20 µL. The reaction was incubated at 37°C for a 1 hour then heat inactivated at 80°C for 15 minutes. The linearized plasmid was gel purified. To synthesize the prime editor mRNA, 10 µL 2X ARCA/NTP Mix, 1 µg template DNA (purified, linearized plasmid), 2 µL T7 RNA Polymerase Mix, and nuclease-free water to 20 µL were combined and incubated at 37°C for 30 minutes. 2 µL DNase I was added to remove residual DNA and incubated at 37°C for 15 minutes. Next, the following Poly(A) tailing reaction was set up: 20 µL prime editor mRNA synthesis reaction, 5 µL 10X Poly(A) Polymerase Reaction Buffer, 5 µL Poly(A) Polymerase, and 20 µL nuclease-free water. The reaction was incubated at 37°C for 30 minutes, then the mRNA was purified with the NEB Monarch RNA Cleanup Kit as described above. mRNA concentration was measured with a Nanodrop and RNA was stored at -20°C until use.

2.5.5 Zebrafish Microinjections

Zebrafish were injected at the one-cell stage with the prime editing mRNA and pegRNA. The injection mixture contained 300 ng/µL prime editor mRNA and 70 ng/µL pegRNA and 2 nL was injected into each embryo. Injected and un-injected siblings were grown in EM at 28.5°C until 1-6 dpf.

2.6 Base Editing

2.6.1 Base Editing Design

I used base editing in an attempt to introduce the specific patient mutation into the zebrafish genome. I used the AceofBases Software to design a crRNA for adenine base editing that placed the adenine base of interest in the position with the highest chance of editing (11 nucleotides from the PAM site). As proof of concept for base editing, I replicated the experiment described by Rosello and colleagues where they use cytosine base editing to edit two zebrafish pigment genes: *tyr* and *slc45a2*. I used the same two crRNA used by Rosello et al., (sequence shown in Table 2.1). All crRNAs were ordered from IDT, resuspended in 1X TE Buffer to a concentration of 100 µM and annealed to tracrRNA as described in section 2.3.

2.6.2 *in vitro* Transcription

The pCS2+_CBE4max-SpRY plasmid was generously gifted by the del Bene lab (Institute de la Vision, Paris, France) and the ABE8e plasmid was ordered from Addgene (#138489). The ABE8e plasmid contains a T7 promoter site and therefore was transcribed *in vitro* using the HiScribe T7 ARCA mRNA Kit (NEB #E2060S) as described in section 2.5.4 after being linearized with EcoRI and gel purified. Transcribed ABE8e mRNA was purified with the Monarch RNA Cleanup Kit (NEB, Catalog #T2040S) and its concentration measured with a Nanodrop before being stored at -20°C. The pCS2+_CBE4max-SpRY plasmid contains a Sp6

promoter site and was transcribed by combining reagents from the HiScribe T7 ARCA mRNA Kit (NEB #E2060S) and MEGAscript Sp6 Transcription Kit (Thermo #AM1330). The plasmid was first linearized by combining 1 µL NotI (Thermo #ER0591), 2 µL 10X Buffer O, 1 µg plasmid, and nuclease-free water to 40 µL. The reaction was incubated at 37°C for 1 hour then heat inactivated at 80°C for 20 minutes. The linearized plasmid was gel purified according to section 2.5.4. The *in vitro* transcription was set up as follows: 10 µL 2X ARCA/NTP Mix, 2 µL 10X Sp6 Reaction Buffer, 2 µL Sp6 Polymerase, 1 µg DNA, and nuclease-free water to 20 µL. The transcription reaction was incubated at 37°C for 2 hours, then 1 µL DNase I was added, and the reaction was incubated at 37°C again for 15 minutes. To add a Poly(A) tail, 20 µL of the *in vitro* transcription reaction was combined with 5 µL 10X Poly(A) Polymerase Buffer, 5 µL Poly(A) Polymerase, and 20 µL nuclease-free water and incubated at 37°C for 30 minutes. mRNA was purified with the NEB Monarch RNA Cleanup Kit according to section 2.5.4. The mRNA was stored at -20°C after its concentration was measured with a Nanodrop.

2.6.3 Reverse Transcription

Because reagents from two kits were combined to transcribe the pCS2+_CBE4max-SpRY plasmid, I reverse transcribed the mRNA to confirm its sequence. I used the QIAGEN OneStep RT-PCR Kit (#210210) and designed primers against two regions of the RNA to reverse transcribe and amplify. The first region was 202 nucleotides long and amplified the APOBEC1 sequence, which encodes the cytosine deaminase. The second region was 946 nucleotides long and was within the Cas9(N) region which encodes the Cas9 nickase. Two reactions with each set of primers were set up containing 5 µL Qiagen OneStep RT-PCR Buffer, 1 µL dNTP Mix (1 mM each), 1 µL Enzyme Mix, < 2 µg mRNA, 3 µL forward primer, 3 µL reverse primer, and nuclease-free water to 25 µL. The reaction was incubated at 50°C for 30

minutes for reverse transcription then 95°C for 15 minutes to activate PCR reagents. The reaction was then incubated in a thermocycler according to the protocol shown in Fig. 2.1. The products of RT-PCR were run on a 2% sodium borate (SB) gel and the band sizes were analyzed under a UV Lamp.

Table 2.4 – Cytosine base editor reverse transcription primers. List of primers used in the reverse transcription of the CBE4max-SpRY mRNA.

Primer Name	Sequence (5' → 3')	Tm (°C)
608F APOBEC-1a FWD Set 1	GTTTACCACAGAGCGGTACTT	54.6
608R APOBEC-1a REV Set 1	GCCTCGTTGCTAGGAGAATAAT	54.5
609F APOBEC-1b FWD	GCACACCTCTCAGAACACAA	55.1
609R APOBEC-1b REV	CAGCCTGGCGATGTAGATAAA	54.7
610F nCas9-SpRYa FWD Set 2	GAGAACCGCCAGAAGAAGATAC	55.1
610R nCas9-SpRYa REV Set 2	CAGGATGGGCTTGATGAACT	54.9
611F nCas9-SpRYb FWD Set 4	CACCATCTACCACCTGAGAAAG	54.9
611R nCas9-SpRYb REV Set 4	CAGGTCGAAGTTGCTCTTGA	54.8

2.6.4 Micronjections

Zebrafish were injected at the one-cell stage with either the cytosine base editor or adenine base editor mRNA and the corresponding gRNA duplex(es). For adenine base editing, I based the concentrations used for each injected component on recommendations from Rosello et

al., 2021, Zhang et al., 2017, and Qin et al., 2018. The final base editing injection mix contained 300 ng/µL ABE8e mRNA and 50 ng/µL *pikfyve* gRNA duplex. For cytosine base editing, the injection mix was made according to Rosello et al., 2021 and contained 600 ng/µL CBE mRNA, 8.6 µM *tyr* gRNA duplex, 8.6 µM *slc45a2* gRNA. Injected and uninjected siblings were grown in EM at 28.5°C until 1-6 dpf before being transferred to the fish facility as described in section 2.2.

2.7 Genotyping

2.7.1 Polymerase Chain Reaction

DNA was extracted from either pools of five to ten 2 dpf embryos or 5 dpf fin clips by heating the tissue in 10 µL NaOH (50 mM) at 95°C for 20 minute before cooling to 4°C for 10 minutes and neutralizing with 1.2 µL 1M Tris pH 8. 50 µL PCR reactions were prepared by combining 10 µL 5X Green GoTaq Buffer, 1 µL nucleotide mix (1 mM each), 4 µL forward primer (5 µM), 4 µL reverse primer (5 µM), 0.25 µL GoTaq Polymerase, <0.5 µg/50 µL DNA, and water to 50 µL. The PCR amplification reaction followed the general protocol in Figure 2.1 and the annealing temperature varied depending on the primers used. Generally, the annealing temperature was set to 2°C lower than the primer melting temperatures (provided by IDT). PCR products were run on a 2% sodium borate (SB) buffer gel stained with Invitrogen 10,000X SYBR Safe DNA Gel Stain at 170V for 30 minutes. Alternatively, if samples were to be gel purified, then they were run on a 1% TAE low-melting point agarose gel at 80-100V for 1-1.5 hours.

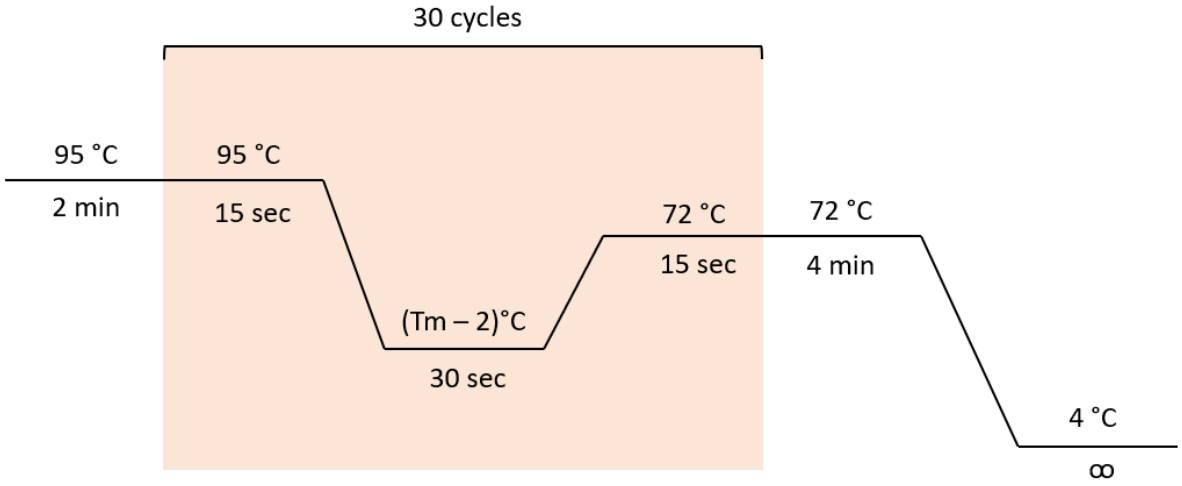

Figure 2.1 – General polymerase chain reaction amplification protocol. Incubation was done in a thermocycler. The annealing temperature was dependent on the primer melting temperatures (Tm) provided by IDT. Generally, annealing temperatures were set to 2 °C lower than the primer's Tm.

Table 2.5 – List of primers used for *pikfyve, tyr,* and *slc45a2* amplification.

Primer Name	Sequence (5' → 3')	Tm (°C)
501F Pikfyve_E38_FWD	CAGACAGGGAACCCACATATT	54.4
501R Pikfyve_E38_REV	GGG CAT CTG CTT CAG AAT AAA C	54.1
502F pikfyve_E38_HRMa FWD	AGTTCTACTGCCGGATCTACTA	54.3
502R pikfyve_E38_HRMa REV	AGTTGACACAGTGGGAAAGAG	54.7
503F pikfyve_E38_HRMb FWD	CGATGCAAATGCTAAGTTCTACTG	54.2
503R pikfyve_E38_HRMb REV	TCCTCTGTGCTCTCCATGAT	55.3
504F pikfyve_exon3&4_FWD	CTCTCTAATCTCTCCCTTTCATTCC	54.3
504R pikfyve_exon3&4_REV	GCGGATGTTCTTCTGAGTAGTT	54.6
505F pikfyve_E38_FWD_M	AGTTCTACTGCCGGATCTACTA	54.3

505R pikfyve_E39_REV	AGTGGTCAACGCTTACCTTTA	53.9
506F pikfyve_E39_FWDb	TCAGGTTGTTGGATTCCTGTATG	54.8
506R pikfyve_E39_REVb	ACAGCCCTAGTTGGGACTAA	55.3
507F tyr_FWD	ATCGGGTGTATCTGCTGTTTTGG	57.4
507R tyr_REV	CCATACCGCCCCTAGAACTAACAT T	58.2
508F slc45a2_FWD	AACCATGACTCTTCTTACTGAGGAC	56.0
508R slc45a2_REV	GACCCTGAAACTCATCTACTTCCTT	56.1

2.7.2 Restriction Fragment Length Polymorphism

The HDR template introduced an XmnI restriction enzyme cut site. Therefore, I used restriction fragment length polymorphism (RFLP) to assess incorporation of the edit. DNA from injected embryos was extracted and amplified as described in section 2.7.1 and then the PCR product was analyzed with RFLP. A reaction containing 1 µg PCR product, 5 µL 10X rCutSmart Buffer, 1 µL XmnI restriction enzyme (NEB, Catalog #R0194), and water to 50 µL was set up and incubated at 37 °C for 1 hour. Reaction products were analyzed on a 2% sodium borate gel. The wildtype sequence does not contain an XmnI cut site, and therefore one band at 454 bp was expected. The mutated sequence carries an XmnI cut site, and therefore two bands at 229 and 225 bp were expected (visible as one band).

2.7.3 Sanger Sequencing

PCR reactions were prepared according to section 2.7.1. PCR reactions were purified using the Monarch® PCR & DNA Cleanup Kit (NEB, Catalog #T1030S). Sanger sequencing samples were prepared by combining 150 ng purified PCR product and 0.25 µM forward (or reverse) primer to a final volume of 10 µL. All sequencing was run by staff at the Molecular

Biology Service Unit (MBSU) at the University of Alberta. Sequencing results were analyzed with SnapGene View 6.0.2.

2.7.4 High Resolution Melt Analysis

High resolution melt (HRM) analysis was used to assess whether gene editing occurred with CRISPR/Cas9, HDR, prime editing, and base editing. I used the QIAGEN Type-it HRM PCR Kit (#206544) and the primers shown in Table 2.5 to analyze genetic sequence variations in exon 38 of the *pikfyve* gene. All samples were run as three technical replicates. A master mix containing 400 µL QIAGEN Master Mix, 112 µL forward primer (5 µM), 112 µL reverse primer (5 µM), and 16 µL nuclease-free water was prepared and divided across 80 PCR tubes. 2 µL gDNA extracted from 5 dpf fin clips or pools of five 2 dpf embryos was added to each tube and samples. Samples were heated to 95℃ for 5 minutes followed by 40 denaturing, annealing, and extension cycles of 95℃ for 10 seconds and 55℃ for 30 seconds. Samples were then heated from 65℃ to 95℃ at a rate of 0.1℃/2 seconds. Fluorescence as a function of temperature was recorded by the Rotor-Gene Q and HRM curves were generated and analyzed in the Rotor-Gene Q software 2.3.5.

2.8 Drug Treatment

Apilimod was ordered from Sigma-Aldrich (#SML2974). The inhibitor was resuspended in dimethyl sulfoxide (DMSO) to a concentration of 5 mM by gently heating. 1 mM aliquots were stored at -20°C and stock inhibitor was stored at -80°C. Drug exposure occurred in 24-well plates for 4 and 5 dpf zebrafish larvae (6 fish/well) and 100 mm x 15 mm petri dishes for 1 mpf fish (5-10 fish/plate). Zebrafish larvae were exposed to apilimod at a concentration of 500 nM (in 1% DMSO/EM) from 4-6 dpf or 5-7 dpf. Control larvae were exposed to 1% DMSO/EM for the same duration. 1 month-post fertilization (mpf) zebrafish were exposed to 500 nM or 1 µM

apilimod (in 1% DMSO/EM) for 4-6 hours while controls were exposed to 1% DMSO/EM for the same duration. The drug was removed through three EM washes at the termination of the experiment and fish were euthanized in 4.2% TMS according to section 2.2.

2.9 Electroretinography

Electroretinography (ERG) is a non-invasive technique that measures retinal electrical activity in response to light. Full-field ERG, which measures a response spanning the entire retina, was used here. Reference and recording electrodes were prepared by removing 2 cm of insulative housing from a platinum electrical lead wire and intertwining the exposed platinum with 4 cm of 32-gauge silver wire. Both electrodes were placed into household bleach (5.25%) for 5 minutes to increase electrode conductivity and then air dried for three minutes. The reference electrode was positioned on top of a 35 mm petri dish, fitted with a sponge soaked in anesthetic, and taped to a 3D printed testing platform. Zebrafish larvae were anaesthetized in TMS until unresponsive and transferred to filter paper that was then placed on the soaked sponge. The tip of the recording electrode was positioned on the centre of the cornea using a micromanipulator. The platform was placed into the ColorDome Ganzfeld light stimulator for ERG testing using the E3 Electrophysiology System. Anesthetized fish were flashed with 10 $cd \cdot s/m^2$ light five times and the average response was calculated from the five individual ERG traces. Waveform quantification was done through the system's built-in algorithm.

2.10 Fluorescent Spectroscopy

Fluorescent spectroscopy was used to quantify melanin according to the protocol described by Fernandes et al., 2016. I used fluorescent spectroscopy to analyze the efficiency of *tyr* and *slc45a2* CBE in inhibiting pigment formation in injected fish. 1-phenyl-2-thiourea (PTU) is an inhibitor that suppresses pigment formation in zebrafish embryos. I treated zebrafish

embryos with 60 mg/L PTU in EM as a negative control for the fluorescence assay. Embryos were euthanized in 4.2% TMS at 3 dpf and samples (20 embryos/sample) were lysed in 1 mL 10% DMSO in 1M NaOH by centrifuging at 10,000 x g for 10 minutes. The supernatant was discarded, and the pellet resuspended in 200 µL 10% DMSO in 1M NaOH. Samples were incubated at 80°C for 1 hour and vortexed every 20 minutes. Samples were then centrifuged at 3000 x g for 5 minutes and 140 µL of the supernatant was added into a PCR strip tube (3 replicates per sample). 60 µL of 30% hydrogen peroxide was added to each sample before the tubes were loosely covered with aluminum foil and incubated at room temperature for 4 hours. Following incubation, samples were centrifuged at 3000 x g for 5 minutes and 150 µL of each sample was loaded into a 96-well COSTAR black bottom microplate. Fluorescence was then measured with a CLARIOstar plate reader at an excitation wavelength of 470 nm and an emission wavelength of 550 nm.

2.11 Tissue Processing

2.11.1 Cryopreservation and Cryosectioning

Zebrafish larvae were euthanized in 4.2% TMS for 15 minutes then placed in 4% paraformaldehyde (PFA) at 4°C for 1-3 days. 8% PFA was prepared by combining 70 mL Milli-Q water with 8 g PFA and heating on a stir plate to 60°C. A few drops of 1 N NaOH were added to clear the solution before cooling to room temperature. The volume of the solution was adjusted to 100 mL with 0.3X PBS and the pH was adjusted to 7.4 with 1 N HCl. 4% PFA was made by diluting 50 mL 8% PFA in 50 mL 1X PBS and stored at 4°C. After fixing, the samples were washed 3 times with 1X PBS (5 min each) and placed in 17.5% sucrose at 4°C for cryo-protection. Once the eyes sunk to the bottom of the tube, the solution was replaced with 35% sucrose and stored at 4°C overnight on a shaker. Eyes were embedded in cryo-molds filled with

Fisher Healthcare Tissue Plus O.C.T Compound Clear and stored at -80°C until sectioning. Eyes were sectioned at 12 µm using a Leica cryostat and Fisherbrand Superfrost Plus slides were stored at -20°C until staining.

2.11.2 Paraffin Embedding and Sectioning

Zebrafish 6 dpf larvae were euthanized in 4.2% TMS for 15 minutes and fixed in neutral buffered formalin (NBF) for 1-3 days at 4°C on a shaker. Samples were washed 3x in PBS and then embedded in agarose (3 fish/block) to aid in positioning and handling. The blocks were allowed to solidify at room temperature before being placed back into NBF overnight. The next day, samples were dehydrated through a graded ethanol series performed in a Leica Tissue Processor 1020 (ethanol concentrations were 50%, 70%, 90%, and 100%). Samples were then placed in a 1:1 toluene:ethanol (100%) solution before being submerged in toluene. Samples were then placed in liquid paraffin wax overnight to allow for tissue penetration. The next day, agarose blocks were mounted in paraffin blocks and allowed to solidify at room temperature. A Leica microtome was used to cut 5 µM coronal sections of the central zebrafish eye that were collected on Fisherbrand Plain Premium microscope slides. Slides were incubated at 37°C until staining.

2.11.3 Transmission Electron Microscopy Fixation and Sectioning

Zebrafish 6 dpf larvae were euthanized in 4.2% TMS for 15 minutes. Euthanized larvae were fixed in 2.5% glutaraldehyde, 2% paraformaldehyde in 0.1M phosphate buffer, pH 7.2-7.4 for 1-3 days in 4°C on a shaker. Tissue processing was carried out in a fume hood and occurred over three days. On day one, fixative was removed with three 0.1M phosphate buffer washes (10 min each) and samples were stained with 1% osmium tetraoxide in 0.1M phosphate buffer for 1 hour. Samples were washed three times in 0.1M phosphate buffer (10 min each) and dehydrated

through a graded ethanol series (15 min each) as follows: 50% ethanol, 70% ethanol, 90% ethanol, 100% ethanol (x3). A 1:1 mixture of 100% ethanol and Low Viscosity Embedding Media Spurr Resin was used to infiltrate the dehydrated samples for 1-3 hours. Next, samples were left in 100% Spurr resin overnight. On day two, the Spurr resin was changed twice in the morning. Samples were embedded in flat molds with Spurr resin and sample ID paper labels before being cured in a 70°C incubator overnight. On day three, samples were removed from the oven following resin hardening and stored at room temperature until sectioning.

Samples were sectioned by Dr. Kacie Norton at the Biological Sciences Microscopy Unit at the University of Alberta using a Reichert-Jung Ultracut E Ultramicrotome to generate sections of 70 to 90 nm thickness. Sections were stained with uranyl acetate and lead citrate stain.

2.12 Tissue Staining

2.12.1 Immunohistochemistry

Cryosections were stained with a variety of primary and secondary antibodies according to the following protocol. If staining occurred immediately after sectioning, slides were allowed to air-dry for at least 2 hours. If slides were frozen after sectioning, then they were allowed to come to room temperature before staining. A lipid line was drawn around sections with a Cole-Pramer Essentials Hydrophobic Barrier PAP Pen to keep liquid on slides. Slides were placed on a rack in a tinfoil-wrapped petri dish lined by a moistened Kim wipe. If slides were to be bleached, they were first fixed for 20 minutes with 4% PFA in a fumehood before being washed three times in 1X PBS (10 minutes each). To bleach sections, 10% H_2O_2 in 1X PBS was added and slides were incubated at 60°C for 1 hour. Slides were then washed again three times with 1X PBS (10 minutes each). The steps to follow were identical for both bleached and unbleached

slides. Slides were washed three times (10 minutes each) with 1X PBTD (0.1% Tween-20, 1% DMSO in 1X PBS) Next, 200 µL of block solution (2% goat serum in 1X PBTD) was added and slides were incubated at room temperature for 30 minutes. The block solution was removed and replaced with 200 µL of block containing the primary antibodies. A piece of Parafilm was gently placed on top of each slide and the plates were covered and incubated at 4°C overnight. The next day, slides were washed three times in 1X PBTD (10 minutes each), and 200 µL of block solution containing secondary antibodies and/or stains was added. Slides were incubated for one hour at room temperature before being washed three times with 1X PBTD (10 minutes each) and coverslipped with Mowiol mounting media (made and kindly provided to us by Dr. Simmonds, University of Alberta) and stored at 4°C until confocal imaging. The following primary antibodies and concentrations were used: mouse monoclonal anti-rhodopsin 4D2 (Novus, US) at 1:500, mouse monoclonal anti-ZPR2 (Zebrafish International Resource Center, Oregon, US, gifted from Waskiewicz Lab) at 1:100, rat monoclonal anti-LAMP1 (1D4B, Departmental Studies Hybridoma Bank, University of Iowa, US) at 1:200, rabbit anti-LC3A/B (Ref#4108S, New England Biolabs, CA) at 1:100. The following secondary antibodies and concentrations were used: goat anti-mouse IgG Alexa Fluor 680 (Ref#A21057, Invitrogen, US; provided by Webber Lab) at 1:500, goat anti-rabbit IgG Alexa Fluor 488 (Ref#A11008, Life Technologies, US) at 1:500, donkey anti-rat IgG Alexa Fluor 488 (Ref#A21208, Invitrogen USA) at 1:500, and donkey anti-mouse IgG Alexa Fluor 594 nm (Ref#R37115, Invitrogen USA, gifted by Simmonds Lab) at 1:500. Peanut Agglutinin (PNA, Ref#L21409, Invitrogen, USA) was used to stain cone outer segments and was added with secondary antibodies at a concentration of 1:500.

2.11.2 Lysotracker Staining

Lysotracker Red DND99 (Ref#L7528, Invitrogen, USA, gifted by the MacDonald Lab) was used to stain lysosomes in live animals. The stain was added to a final concentration of 10 μM to 24-well plates containing six zebrafish larvae in EM. Zebrafish were incubated with the stain at 28.5°C for 2 hours before being rinsed three times with EM to remove the excess stain. Fish were then euthanized in 4.2% TMS and fixed according to section 2.11.1.

2.12.3 Hematoxylin and Eosin

All processing and staining steps were processed in a fumehood while wearing nitrile gloves (except for the tap water wash step, which occurred in a sink with gloves). Slides were first washed twice in toluene (5 minutes/wash) to deparaffinize. Samples were rehydrated through a graded ethanol series (100%, 90%, 70%, 50%) and then washed in distilled water for 2 minutes. Slides were stained with Hematoxylin Gill III (Leica Biosystems) for 2 minutes and then rinsed with cold tap water for 15 minutes to remove the stain. Slides were placed in 70% ethanol for 2 minutes before being stained with eosin (Leica Biosystems) for 30 seconds. Slides were washed twice in 100% ethanol to remove the eosin stain (2 minutes each) and kept in toluene during coverslipping with DPX mounting media (Electron Microscopy Sciences, Hatfield, USA). Slides were dried in a 37°C incubator overnight and stored at room temperature until imaging.

2.12.4 TUNEL Assay

Cryosections on SuperFrost Plus slides were fixed in freshly prepared 4% paraformaldehyde for 20 minutes at room temperature and then washed three times in 1X PBS (10 min each). Slides were incubated for 2 minutes on ice in a permeabilization solution consisting of 0.1% Triton X-100 in 0.1% sodium citrate. Slides were rinsed twice with PBS and

then 50 µL of the TUNEL reaction mixture, consisting of 5 µL TUNEL Enzyme (MiliporeSigma, Catalog #11767305001) and 45 µL TUNEL Label (MilliporeSigma, Catalog #11767291910), was added to the sections. Slides were incubated for 60 minutes at 37°C in a humid, dark environment before being rinsed three times in PBS and coverslipped with Mowiol mounting media. Slides were stored at 4°C until imaging.

2.13 Image Acquisition and Analysis

2.13.1 Light Microscopy

I used a Zeiss Axioscope.A1 and a SeBaCam camera (Laxco Inc., Mill Creek, WA) to image histological retinal sections. Brightfield images were collected at varying magnifications including 10X, 20X, 40X, 63X, and 100X. I used ImageJ to quantify retinal layer thickness and figures were assembled in Inkscape 1.1.

2.13.2 Confocal Microscopy

A Zeiss LSM 510 Meta Confocal Microscope was used to image immunostained stained tissue and TUNEL assay samples. Images were captured at 10X, 20X, 40X, and 63X. Staining was quantified in ImageJ by first creating a binary version of the image. The threshold was then adjusted to highlight puncta and the watershed tool was used to automatically split puncta that are too close together and merged as one. Puncta number and average size was then measured using the “Analyze Particle” tool.

2.13.3 Transmission Electron Microscopy

Ultrathin sections were imaged with a Philips – FEI Morgagni 268 transmission electron microscope operating at 80 kV. Images were captured with a Gatan Orius CCD Camera. Pigment granule analysis was performed in ImageJ according to the steps described in section 2.12.2.

2.14 Statistical Analysis

All statistical analysis was performed in GraphPad Prism Version 9.3.0. Where comparisons were between two groups, an unpaired t-test was performed. Where comparisons between more than two groups were performed, a one-way ANOVA followed by Tukey's posthoc test was performed. An outlier test was done to remove outliers from the data. All measurements are reported as mean and standard deviation.

CHAPTER THREE: CHARACTERIZATION OF *pikfyve* CRISPANT ZEBRAFISH

3.1 Introduction

Although *PIKFYVE* mutations in humans are largely associated with ocular phenotypes, little is known about the protein's roles in the eye outside of the cornea and the lens. Based on the patient identified by Dr. MacDonald, I predicted that PIKFYVE plays an essential role in the retina. In particular, the known functions of PIKFYVE align well with the physiology of the RPE. The RPE contains melanosomes and maintains a massive phagocytic load for the breakdown of OS discs. It is also highly metabolically active and subject to photooxidation, suggesting a high dependence on autophagy. Given that phagocytosis, autophagy, and melanosome biogenesis are all directly linked to PIKfyve, as demonstrated in other cell types, I hypothesized that loss of PIKfyve would impair these pathways, lead to the buildup of vacuoles, and impair RPE health. The photoreceptors would also be affected as a secondary consequence of disrupted RPE function.

I chose to investigate the role of PIKfyve in the RPE using zebrafish. The complex relationship between photoreceptors and RPE can only be properly studied *in vivo* and the accessibility of the zebrafish embryos from the one-cell stage creates opportunity for genetic manipulation and careful follow-up evaluation. The zebrafish genome contains one ortholog of the *PIKFYVE* gene, *pikfyve*, which is located on chromosome 9. The gene is highly conserved between humans and zebrafish and therefore, I targeted the same region mutated in the congenital cataracts and retinal dystrophy patients for CRISPR/Cas9 mutagenesis. Two crRNAs targeting the third and fourth exons making up the kinase domain which corresponds to exons 38 and 39 in zebrafish were designed. My goal was to use CRISPR/Cas9 mutagenesis to introduce random mutations in exons 38 and 39, creating a loss of function model. Knockout of *pikfyve* in

zebrafish is embryonic lethal by 7-9 dpf (Mei et al., 2021), and therefore I expected to find a high mortality rate in CRISPR-injected (referred to as *pikfyve* crispant) fish if a high cutting efficiency is achieved. I sought to analyze the retinas of *pifyve* crispants at 5 and 6 dpf to characterize some of the roles of Pikfyve in the eye. As a first step, I needed to validate that the crispant fish did indeed carry mutations in *pikfyve*.

3.2 Validation of CRISPR/Cas9 Editing

3.2.1 HRM Analysis

I used high resolution melt (HRM) analysis to detect gene editing in CRISPR-injected zebrafish. Hydrogen bonding is variable between base pairs, with adenine-thymine (AT) base pairs forming two hydrogen bonds and cytosine-guanine (CG) base pairs forming three hydrogen bonds. Consequently, the energy required to break CG bonds is higher than the energy required to break AT bonds. HRM takes advantage of this difference by introducing an intercalating dye that fluoresces only when bound to double-stranded DNA. As samples are heated, double-stranded DNA is denatured, and the dye loses its fluorescence as a result. The temperature at which DNA denatures is dependent on the composition of the DNA. For instance, a higher GC content will result in a higher melting temperature since more energy is required to break the hydrogen bonds. Thus, by recording fluorescence as temperature increases, an HRM curve unique to a particular DNA sequence is generated.

While HRM cannot determine the exact nature of DNA mutations, it is a quick and effective method of analyzing general changes to a DNA sequence, especially following CRISPR mutagenesis. As discussed in section 1.6.1, double-strand breaks introduced by Cas9 are repaired through NHEJ, which results in the introduction of random mutations. A shift in the

HRM curve from wildtype indicates cutting and imprecise repair of DNA following CRISPR/Cas9 mutagenesis. A shift to the left could be indicative of a deletion or a higher AT content in the edited sequence while a shift to the right could be indicative of an insertion or a higher GC content in the edited sequence.

I analyzed pools of five injected zebrafish embryos compared to pools of five uninjected siblings. Samples were analyzed as technical triplicates and the HRM curves of the two groups were compared. The region targeted by the crRNA in exon 38 was analyzed and as shown in Fig. 3.1, *pikfyve* crispants showed a shifted HRM curve indicative of efficient Cas9 cutting and the introduction of mutations in *pikfyve*.

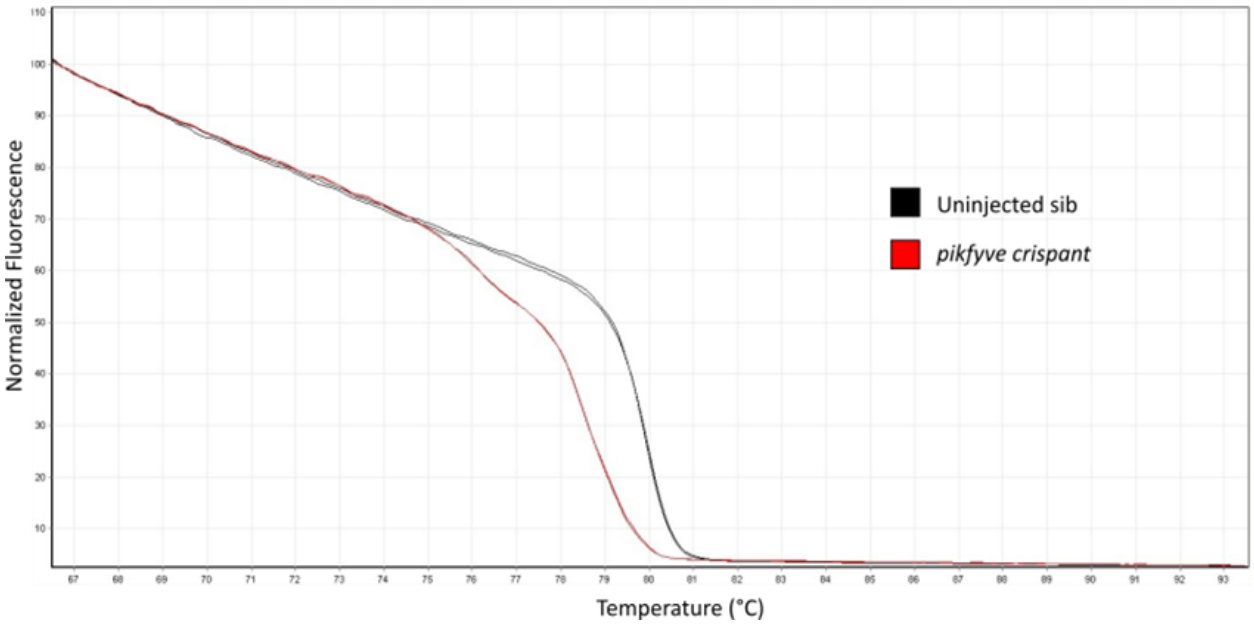

Figure 3.1 – HRM analysis of *pikfyve* crispants. Pools of 5 *pikfyve* crispants and uninjected siblings were analyzed as triplicates with HRM. Primers flanking the region targeted by CRISPR/Cas9 mutagenesis (exon 38 of the *pikfyve* gene) were designed to analyze gene editing.

The red curve (*pikfyve* crispant) is shifted to the left compared to the control (black), indicative of gene editing in the region analyzed.

3.2.2 PCR Amplification

As further validation of cutting, I performed polymerase chain reaction (PCR) to amplify the region targeted by the CRISPR/Cas9 crRNAs. DNA from pools of 5 injected or uninjected embryos was extracted and amplified in a thermocycler. PCR products were run on a 2% SB gel and the size of the bands were analyzed under a UV lamp and compared to a 1 kb DNA ladder. The forward and reverse primers were designed to create a 454 bp amplicon in the controls. I found that the uninjected band appeared between the 400 and 500 bp ladder bands, consistent with the expected size. I observed variability in band size for *pikfyve* crispants, as shown in Fig. 3.2. However, the difference was too subtle to be fully characterized on the gel. Therefore, PCR products were purified and sent for Sanger sequencing.

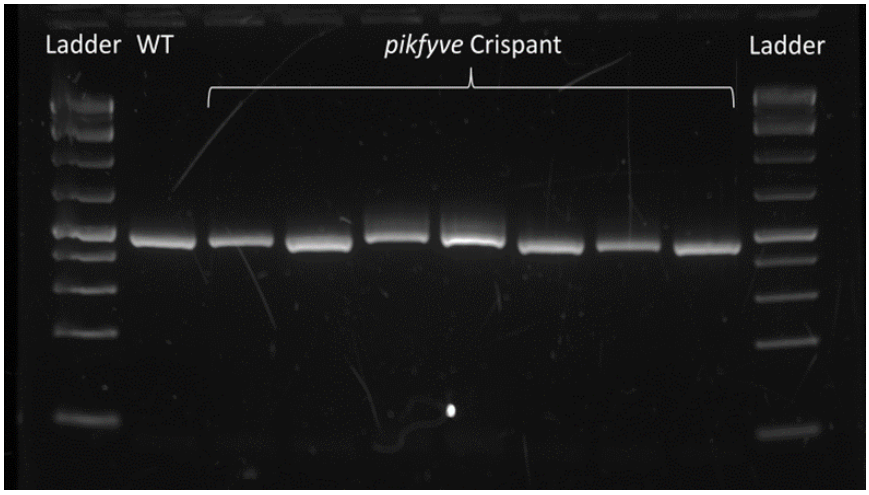

Figure 3.2 – *pikyfve* crispant PCR amplification products. DNA was extracted from pools of 5 uninjected embryos (WT) or CRISPR injected embryos (*pikfyve* crispant) and the region

targeted by the CRISPR crRNA in exon 38 was amplified with PCR. PCR products were run on 2% sodium borate gel and band size was compared against a 1 kb DNA ladder.

3.2.3 Sanger Sequencing

While HRM and gel electrophoresis can provide qualitative insight into whether gene editing has occurred, they do not reveal the exact type of editing. Therefore, I used Sanger sequencing to reveal specific DNA changes following CRISPR/Cas9 mutagenesis. DNA was extracted from pools of five injected embryos and amplified with primers targeting exon 38 of the *pikfyve* gene. Purified, amplified DNA was sent for sequencing with the reverse primer and therefore the sequence shown in Fig. 3.3 is the reverse complement of the sense strand. Upstream of the PAM site, there were no changes in the DNA sequence from wildtype and the quality of the sequence was clear. Although the peaks representing the wildtype sequence were still present downstream of the PAM and cut sites, the reads became noisier, with multiple traces appearing. I analyzed CRISPR/Cas9 injected zebrafish and therefore, the F0 generation likely exhibits mosaic editing. Thus, the multiple DNA sequences observed in Fig. 3.3 indicate efficient cutting by the Cas9 and the introduction of random mutations in a mosaic fashion.

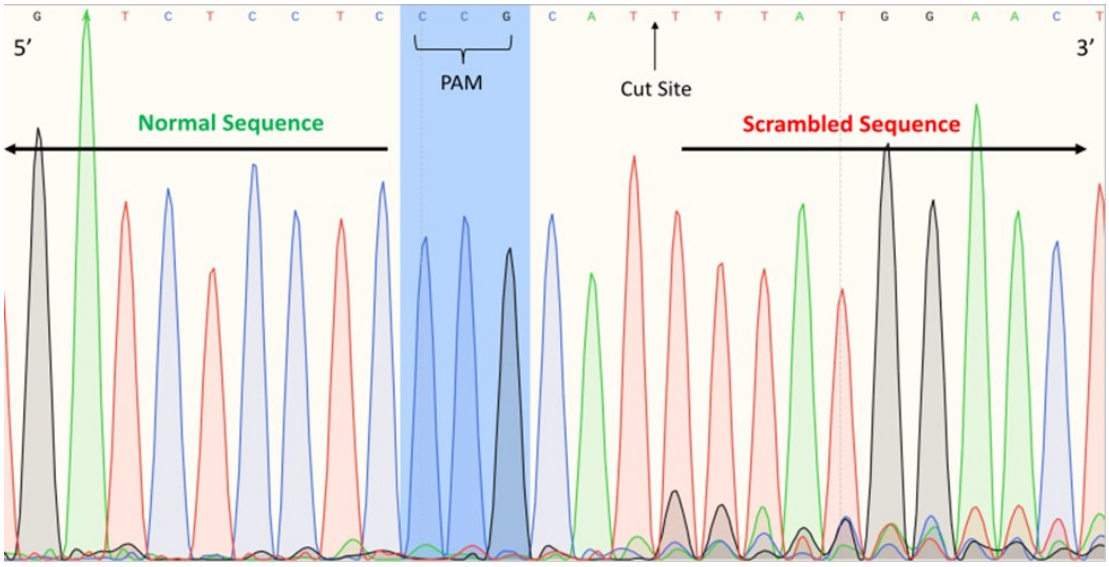

Figure 3.3 – *pikfyve* crispant Sanger sequence. DNA from five CRISPR-Cas9 injected zebrafish was extracted and the region surrounding the CRISPR target site in exon 38 was sequenced. While the sequence appeared normal upstream of the PAM site, it became noisy and multiple sequences are observed downstream of the cut site, indicative of mosaic DNA editing in the F0 generation.

3.3 *pikfyve* crispant survival and phenotypes

3.3.1 Knockout of *pikfyve* is embryonic lethal in zebrafish

Following CRISPR mutagenesis, injected embryos were kept in a 28.5°C incubator in EM and then transferred to the fish facility at 5 dpf. I found that only ~10% of injected fish transferred to the facility survived the first week. Therefore, fish were kept in the laboratory incubator past 5 dpf to closely monitor and a large proportion (~70%) died between 6 and 7 dpf as shown in Fig. 3.4. The high mortality rate was not due to the injection process itself as first, zebrafish injected with two crRNAs targeting other genes (*tyr* and *slc45a2*) showed normal survival compared to uninjected siblings (Fig. 3.4) and second, *pikfyve* crispant zebrafish did not

die immediately following injections but rather at 6-7 dpf. Hence, these findings agree with other work showing that *pikfyve* knockout is embryonic lethal in zebrafish and other species (Mei et al., 2021).

I hypothesized that fish carrying heterozygous mutations in *pikfyve* would survive to adulthood. To generate heterozygous fish, I would need to identify injected F0 fish carrying *pikfyve* mutations, outcross them to wildtype fish, and then screen for heterozygous offspring. Unfortunately, of the 5-10% of CRISPR-injected zebrafish transferred to the facility that survived, no editing in *pikfyve* could be detected with Sanger sequencing from adult fin clips. It is possible that even heterozygous mutations in *pikfyve* are embryonic lethal in zebrafish or that the CRISPR/Cas9 mutagenesis was highly efficient, knocking out the gene to the point of lethality. Of note, the survival rate of larvae in our zebrafish aquatics facility was reduced at this time, possibly because of elevated nitrates and/or reduced water hardness, which may have impeded my ability to find fish carrying *pikfyve* mutations. Nonetheless, I used crispants (Crispr-injected fish) for analysis rather than further attempting to isolate a stable line.

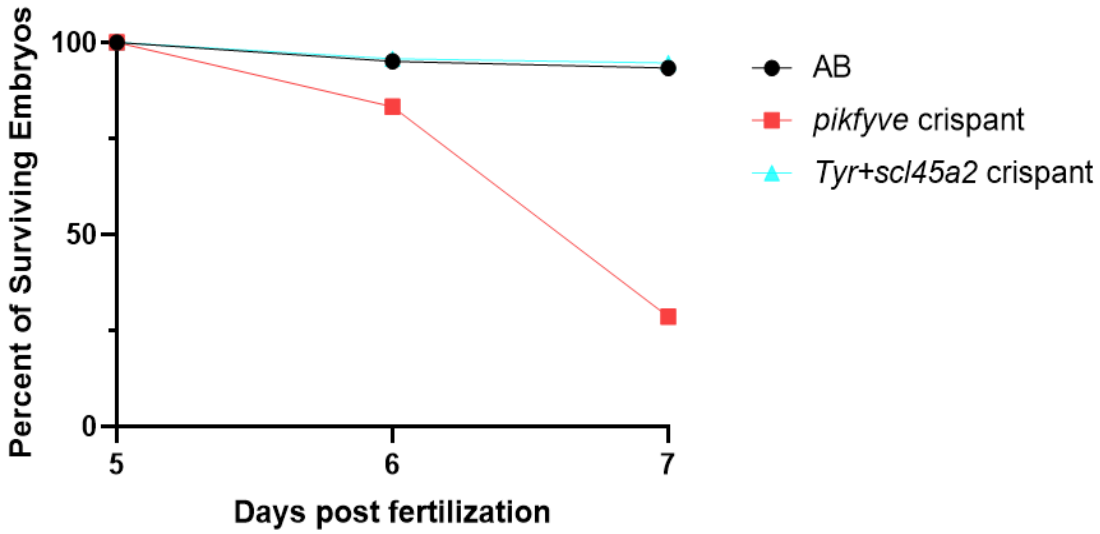

Figure 3.4 – Knockdown of *pikfyve* is embryonic lethal. Zebrafish embryos were injected with two crRNAs targeting exons 38 and 39 of the *pikfyve* gene (*pikfyve* crispant), two crRNAs targeting the *tyr* and *slc45a2* genes (*tyr* + *slc45a2* crispant), or not injected (uninjected sib, AB). Fish were grown in EM at 28.5°C and survival was monitored until 7 days post fertilization (dpf).

3.3.2 *pikfyve* crispants exhibit abnormal morphology and swimming behavior

Along with increased mortality, *pikfyve* crispants also exhibited a range of morphological and behavioral abnormalities. On average, *pikfyve* crispants were less physically active and showed a decrease in swimming. Moreover, they were less responsive to physical stimuli compared to uninjected siblings. 24-well plates with 6 fish/well were observed for responsiveness of fish to the physical stimuli of a tap to the plate. In control fish, a tap would reliably trigger swimming while in *pikfyve* crispants, ~70% of fish did not show a response to physical stimuli. *pikfyve* crispants developed edema to varying degrees as shown in Fig. 3.5A-B.

Body length was measured in ImageJ from the mouth to the tip of the tail fin. I found that *pikfyve* crispants were significantly smaller than uninjected siblings (Fig. 3.5C). Furthermore, *pikfyve* crispant fish failed to develop a swim bladder, which is a gas filled organ that helps fish maintain their buoyancy. It is possible that improper swim bladder inflation is a contributing factor to the high mortality rate observed at 6-7 dpf. In summary, *pikfyve* crispants showed developmental abnormalities including smaller body size, decreased movement, failure to inflate the swim bladder, and edema.

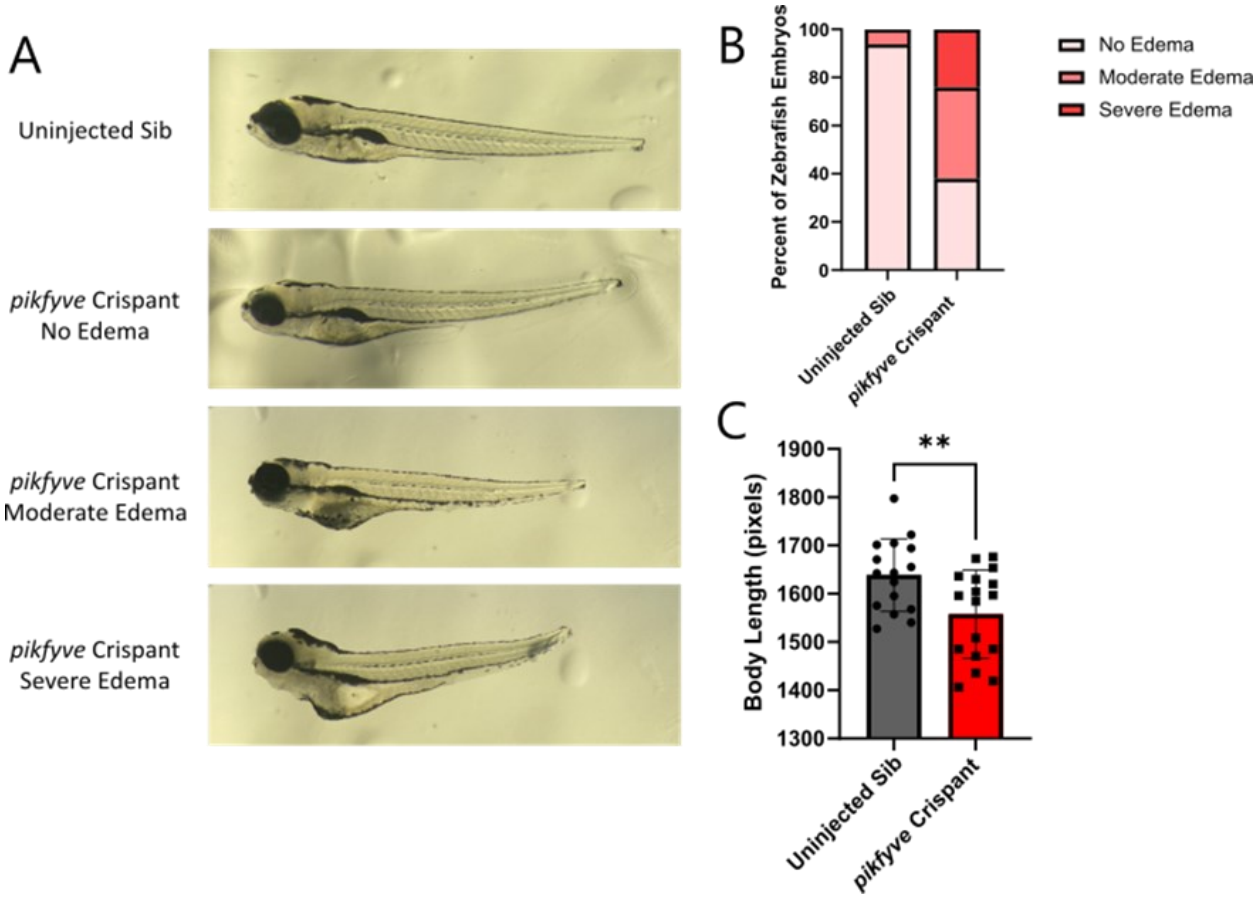

Figure 3.5 – Morphological abnormalities of *pikfyve* crispants. (A) Light microscopy images of *pikfyve* crispants compared to uninjected siblings. (B) Quantification of percentage of fish with no, moderate, or severe edema in *pikfyve* crispants compared to uninjected siblings. (C)

Quantification of body length measured from the mouth to the tail fin in ImageJ. Uninjected siblings n=16, *pikfyve* crispants n=18.

3.4 Impaired retinal electrical function in *pikfyve* crispants

I used electroretinography (ERG) to assess whether *pikfyve* CRISPR mutagenesis influences visual function. Since knockout of *pikfyve* is embryonic lethal at 7 dpf, I performed ERG testing at 5 dpf. Cone photoreceptors are fully developed and functional by 5 dpf in zebrafish while rods are not functional until 15 dpf (Bilotta et al., 2001). Therefore, I only performed photopic (light-adapted) testing to assess cone responses to light. Fish were anesthetized for 30 seconds before ERG testing, which consisted of five 10 $cd \cdot s/m^2$ -light flashes. Retinal electrical responses from each flash were recorded and averaged.

Eleven *pikfyve* crispant fish underwent ERG testing, and of those only two showed a meaningful response. The remaining nine fish showed flat ERGs with no significant a-wave or b-waves recorded as shown in Fig. 3.6A. The a-waves and b-waves in Fig 3.6B-E for *pikfyve* crispants were quantified by the program's built-in algorithm, which picks the lowest and highest peaks within a predetermined timeframe and assigns them as the a-wave and b-wave, respectively. Nevertheless, it is difficult to analyze a-wave and b-wave implicit time for the *pikfyve* crispants as there is no significant wave recorded. An outlier test was performed on the b-wave data and the two *pikfyve* crispant fish that showed a retinal electrical response were removed. These two fish exhibited wildtype-like responses and therefore, it is likely they were fish in which CRISPR mutagenesis was unsuccessful. All uninjected siblings showed significant responses to light with little variation in implicit time of a-waves and b-waves and some

variation in the amplitude of the two waves. These findings suggest that *pikfyve* plays a critical role in cone photoreceptor functioning as its impairment results in flat ERGs.

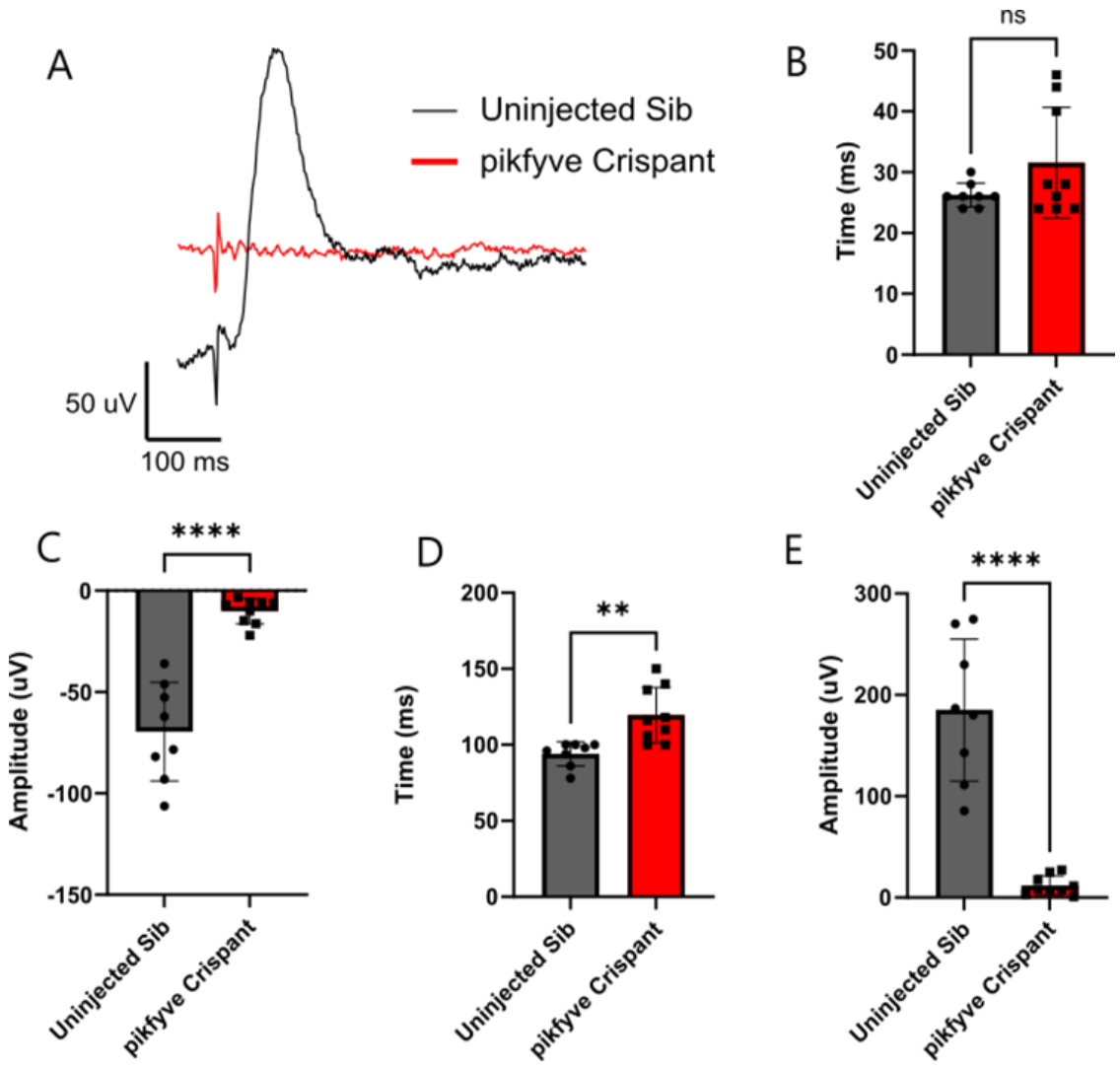

Figure 3.6 – Flat photopic ERG responses in *pikfyve* crispants. (A) Representative ERG trace from *pikfyve* crispant (red) and uninjected sibling (black). The responses shown are the averages of five individual responses. Quantification of (B) a-wave implicit time, (C) a-wave amplitude,

(D) b-wave implicit time, and (D) b-wave amplitude for uninjected siblings (n=8) and *pikfyve* crispants (n=9). **p<0.01; ****p<0.0001

3.5 *pikfyve* crispant zebrafish retinal architecture

3.5.1 Conserved retinal layer development in *pikfyve* crispants

To understand the mechanism underlying impaired cone electrical responses, I analyzed retinal architecture in *pikfyve* crispants with histology. Hematoxylin stains nuclei and endoplasmic reticuli blue, while eosin stains cell membranes and mitochondria pink. Together, hematoxylin and eosin (H&E) can be used to localize individual cells and study their shape and organelle distribution. Within the retina, H&E allows for the visualization of retinal architecture and quantification of the thickness of retinal layers.

5 dpf *pikfyve* crispants and uninjected siblings underwent histological examination. Overall, *pikfyve* crispants developed all retinal layers as shown in Fig. 3.7B although the organization and thickness of these layers varied compared to controls. *pikfyve* crispant eyes were significantly smaller than uninjected siblings, consistent with the smaller body size observed in Fig 3.5. During sectioning, it was noted that *pikfyve* crispant eyes were more fragile and showed a higher degree of tearing compared to controls, especially between the RPE and OS and within the RPE. The thickness of the RPE, ONL, INL, IPL, and GCL for both groups was measured. Notably, quantification was difficult in some *pikfyve* crispants as the distinction between the layers, especially the ONL and INL, was sometimes vague (Fig. 3.7B). The thickness of all retinal layers was comparable to control except for the IPL, which was significantly smaller in *pikfyve* crispants. The GCL showed a large amount of variation in *pikfyve* crispants (Fig. 3.7D). Moreover, although not statistically significant, the RPE of *pikfyve*

crispants was thinner than that of controls. In three of the eight *pikfyve* crispant eyes analyzed, there was an abnormal space between the RPE and photoreceptor OS (yellow arrow in Fig. 3.7B). The space showed eosin staining and therefore, it may be excess membranes between the RPE and OSs. Furthermore, in five of the eight eyes, I observed holes in the retina, appearing most frequently in the INL, IPL, and GCL. I hypothesized that these were areas of cell death. Taken together, these observations suggest that while *pikfyve* may not be critical in overall retinal development, there are clear differences in retinal architecture of *pikfyve* crispants compared to controls including thinning of the IPL and disorganization of the retina (in particular of the RPE, INL, and ONL).

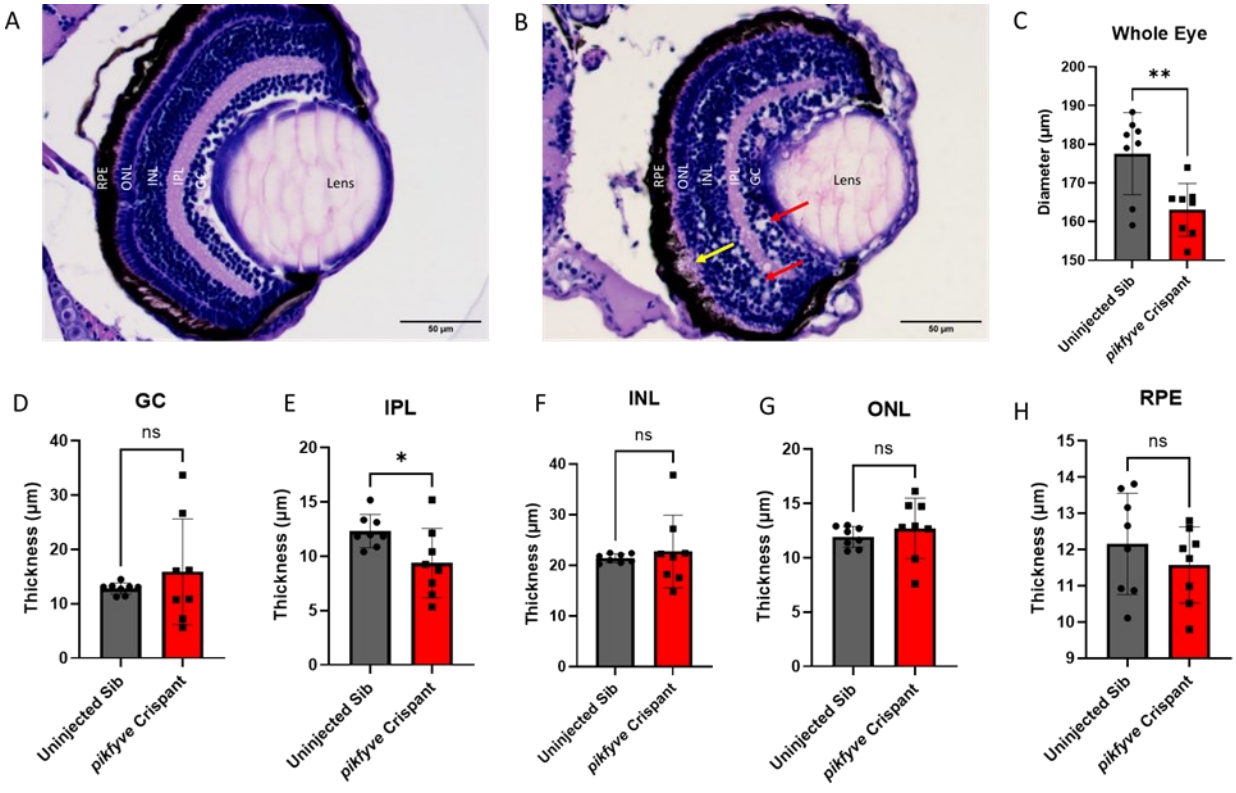

Figure 3.7 – Retinal architecture of *pikfyve* crispants. H&E staining from (A) uninjected siblings and (B) *pikfyve* crispants was performed on retinal cross sections. Quantification of (C)

whole eye diameter, (D) ganglion cell (GC) layer, (E) inner plexiform layer (IPL), inner nuclear layer (INL), outer nuclear layer (ONL), and retinal pigment epithelium (RPE) thickness was done in ImageJ from 9 control and 8 *pikfyve* crispant fish. *p<0.05; **p<0.01. Red arrows point to holes within the retina while the yellow arrow highlights abnormal space between the photoreceptor outer segments and the RPE.

3.5.2 Increased cell death in brain and eyes of *pikfyve* crispants

To confirm if the holes observed in retinal histology of *pikfyve* crispants were indeed areas of cell death, I performed a terminal deoxynucleotidyl transferase-mediated dUTP nick end labeling (TUNEL) assay. TUNEL assays detect DNA breaks and label the free 3' hydroxyl termini. Since DNA breakage is common in apoptosis, TUNEL assays are frequently used to label apoptotic cells. Here, I performed a TUNEL assay on transverse cross sections of 5 dpf zebrafish, which allows me to visualize both eyes and the brain.

As shown in Fig. 3.8C-D, the number of TUNEL positive cells was significantly higher in the eyes and brains of *pikfyve* crispants compared to controls, indicative of increased cell death. Interestingly, staining was largely observed in the retinal periphery and the anterior parts of the eye. Particularly, TUNEL-positive cells were detected in the cornea, iris, and surrounding the lens. TUNEL-positive cells were also detected in the ciliary marginal zone (CMZ), a ring of proliferative cells surrounding the retinal periphery that contains retinal stem and progenitor cells (Fischer et al., 2013). Within the brain, TUNEL-positive cells were mostly located in the dorsal area. The significance of the location of the staining will be discussed later. Taken together, these findings suggest that *pikfyve* is important in maintaining the health of various ocular and brain cells and its loss results in increased cell death in those regions. I did not perform TUNEL assays

on other tissues in *pikfyve* crispants; however, in the future it would be interesting to assess if cell death is also increased in other tissues.

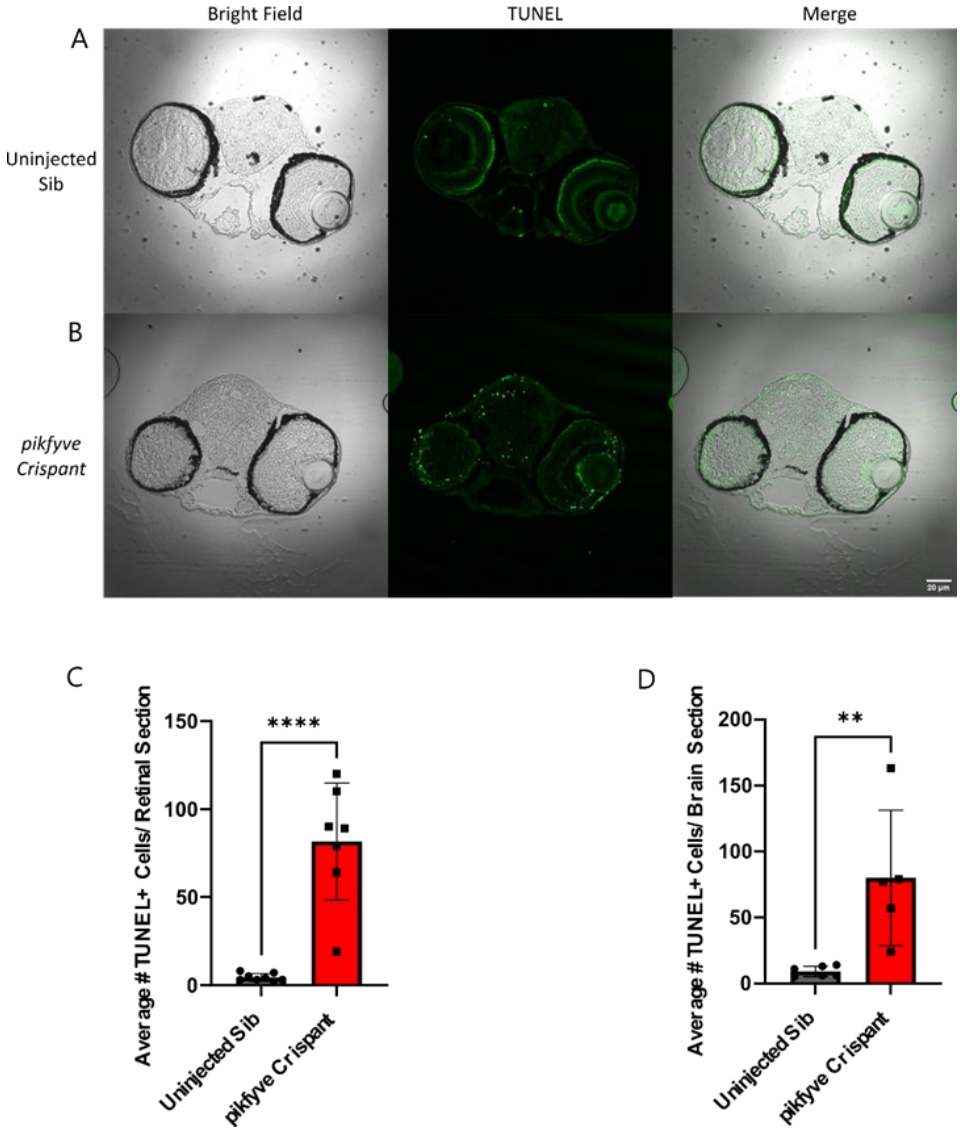

Figure 3.8 – Increased cell death in brain and eyes of *pikfyve* crispants. A TUNEL assay was performed on transverse sections of (A) uninjected controls (n=6) and (B) *pikfyve* crispants (n=6). Quantification of number of TUNEL positive cells in the eyes (C) and brain (D) was performed in ImageJ. **p<0.01; ****p<0.0001.

3.6 Ultrastructural abnormalities in *pikfyve* crispant zebrafish retinas

3.6.1 Outer segment shortening and RPE hypertrophy

While analyses of retinal sections using widefield and confocal microscopy provide a general understanding of retinal architecture, they have limited capacity to highlight experimental differences at the cellular and subcellular levels. On the other hand, transmission electron microscopy (TEM) provides high resolution images at large magnification. Therefore, I utilized TEM to visualize retinal ultrastructure, specifically focusing on the RPE and photoreceptor OSs of 5 dpf *pikfyve* crispants and age-matched controls.

Upon TEM examination, I observed drastic differences between *pikfyve* crispants and controls. Firstly, the RPE of *pikfyve* crispants was inconsistent in thickness, with areas that appeared hypertrophied (Fig. 3.9B, red arrow). This finding of RPE expansion could explain the abnormal area observed between the photoreceptor OS and RPE in the retinal histology (section 3.5.1). While it appears that RPE cells are hypertrophied, it is also possible that their size is normal but there is increased RPE cell proliferation. Either way, the expansion of the RPE into the photoreceptor layer was associated with clear changes to the photoreceptor OSs. To quantify this, I measured the length of the photoreceptor OSs and found that they were significantly shorter in *pikfyve* crispants compared to uninjected siblings. The number of OSs per section was comparable between *pikfyve* crispants and controls (Fig. 3.9D), consistent with my TUNEL finding of cell death not being localized to the photoreceptors and RPE. Of note, rod and cone photoreceptors were grouped during analysis and therefore, I cannot conclude a differential role of *pikfyve* in rods versus cones from TEM data.

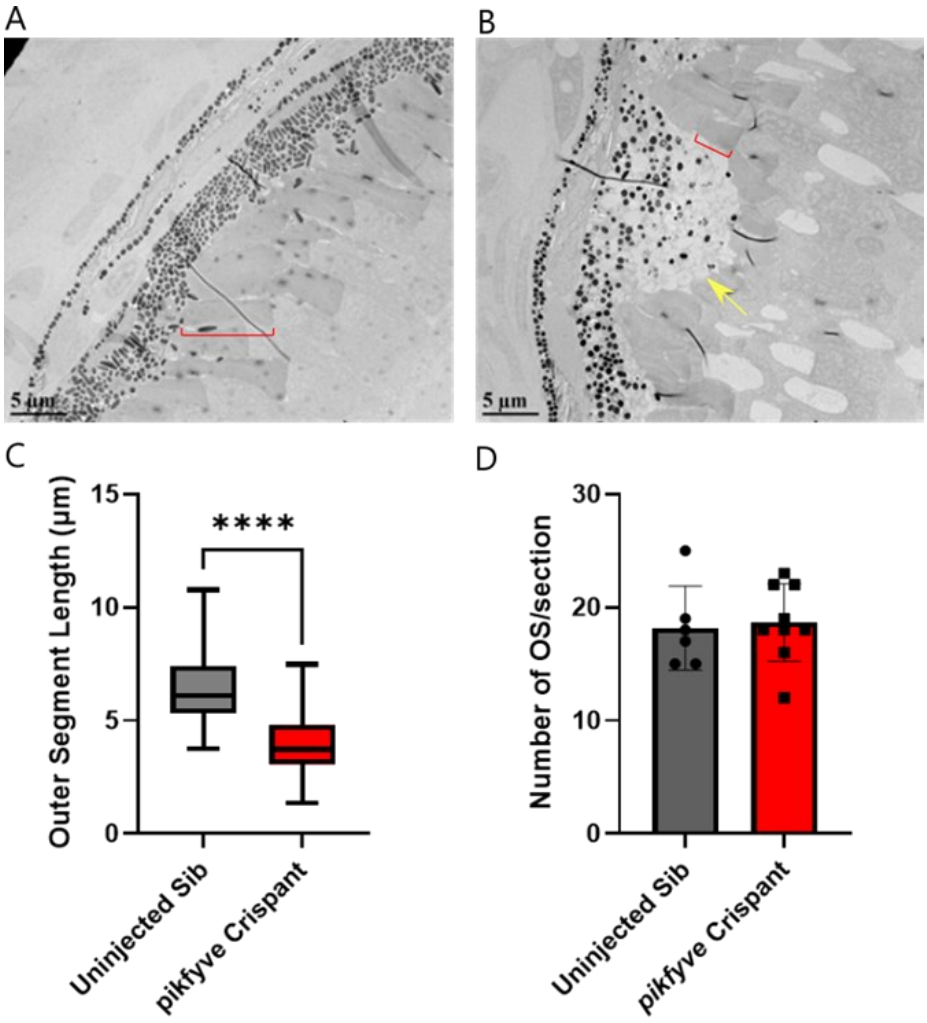

Figure 3.9 – Outer segment shortening and RPE hypertrophy in *pikfyve* crispants. TEM cross sections of (A) uninjected control and (B) *pikfyve* crispant. (C) Outer segment length and (D) number of outer segments per section were quantified in ImageJ. The red bracket shows photoreceptor outer segments and the yellow arrow points to a region of RPE hypertrophy. ****<0.0001. *pikfyve* crispant n=3 fish; uninjected sibling n=2 fish.

3.6.2 Abnormal RPE pigmentation

Upon TEM examination at lower magnification, it was evident that RPE pigmentation was different between *pikfyve* crispants and uninjected controls. To analyze this difference, I first

quantified the amount of pigment in each group through analyzing the number of melanosomes per section in ImageJ (Fig 3.10C). Of note, pigment associated with the choroid was also included in these measurements and thus, the data represented in Fig. 3.10D-E groups pigment of both the RPE and choroid. The number of melanosomes was comparable between *pikfyve* crispants and controls (Fig. 3.10D). Moreover, the average size of the melanosomes was also comparable between the two groups (Fig. 3.10E).

Since no clear difference could be quantified at a zoomed-out view, I imaged the melanosomes at higher magnifications (Fig. 3.10A-B). In controls, melanosomes were fully pigmented circular or ellipsoidal organelles (Fig. 3.10A). In contrast, *pikfyve* crispant melanosomes were not fully pigmented but rather appeared as aggregates of scattered melanin (Fig. 3.10B). As melanosomes mature, they transition from being circular to more ellipsoidal (Lopes et al., 2007b). Therefore, I quantified the number of rod-shaped melanosomes per section in *pikfyve* crispants and controls to assess melanosome maturation and found that *pikfyve* crispants developed significantly fewer rod-shaped melanosomes (Fig. 3.10F). Taken together, these observations suggest that while *pikfyve* may not be critical in the formation of pigment, it is required for the proper development and maturation of melanosomes.

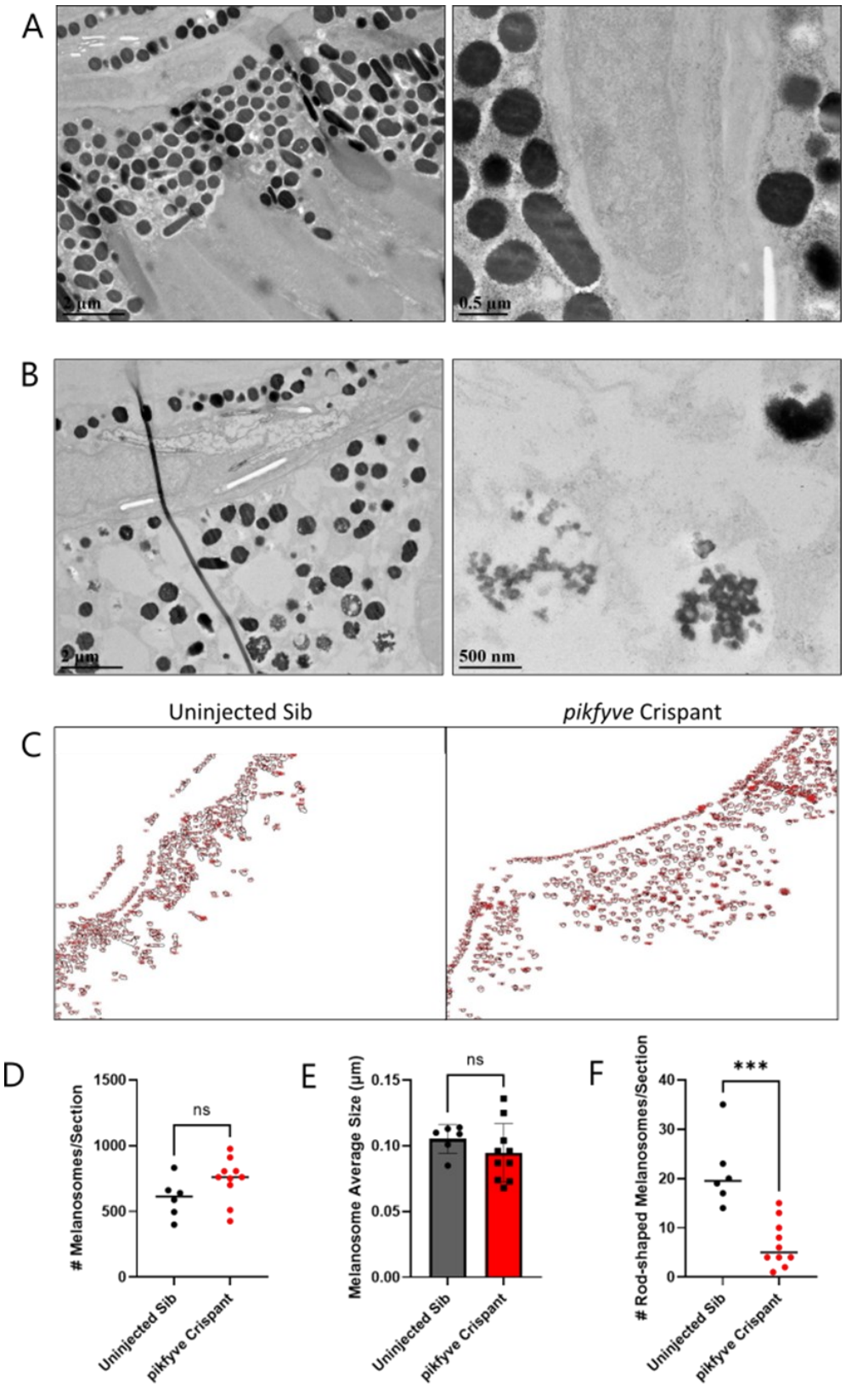
A
1 µm
0.5 µm
B
2 µm
500 nm
Uninjected Sib
pikfyve Crispant
C
D
Melanosomes/Section
1500
1000
500
0
ns
Uninjected Sib
pikfyve Crispant
E
Melanosome Average Size (µm)
0.15
0.10
0.05
0.00
ns
Uninjected Sib
pikfyve Crispant
F
Rod-shaped Melanosomes/Section
40
30
20
10
0
***
Uninjected Sib
pikfyve Crispant

Figure 3.10 – Analysis of retinal pigmentation in *pikfyve* crispants. Low magnification (left panel) and high magnification (right panel) of retinal pigment in (A) control and (B) *pikfyve* crispants. (C) Quantification of melanosomes was done in ImageJ by creating a binary version of TEM images and measuring the number and size of black pixels. Graphs show (A) number of melanosomes per section, (B) average size of melanosomes per section, and (C) number of rod-shaped melanosomes per section. Data was collected from 3-5 sections from each of three *pikfyve* crispant fish and two uninjected siblings. ***p<0.001.

3.6.3 Retinal vacuolization

One of the most observed cellular phenotypes following PIKfyve inhibition is vacuolization (Hasegawa et al., 2017). Vacuoles can be detected with electron microscopy and therefore I used TEM to analyze vacuoles within the retinas of *pikfyve* crispants. I examined retinas from three 5 dpf *pikfyve* crispants and compared them to two uninjected siblings.

Two of the three crispants analyzed showed a significant amount of vacuolization in the retina (Fig. 3.11A, right panel). The vacuoles appeared most in the RPE and the photoreceptor inner segment region. The nature of the vacuoles (e.g., enlarged lysosome, phagosome etc.) was difficult to characterize without the use of markers in the TEM images. Vacuoles differed in size depending on their location, with those that appear in the inner segment region being larger than those in the RPE. Moreover, vacuole shape and contents varied. Most vacuoles appeared empty with no recognizable material within the vacuole. However, I detected the presence of some material within other vacuoles. The number and size of the vacuoles was quantified in ImageJ (Fig. 3.11B-C) and I found that the number of vacuoles was significantly higher in *pikfyve* crispants compared to controls. However, the difference in vacuole area was not significant due

to the large variation in vacuole size depending on location in *pikfyve* crispants. Of note, analysis of vacuoles was only done in the two *pikfyve* crispant fish that showed vacuolization. The third fish was excluded from this analysis for two reasons. Firstly, the location of the section was further anterior in the eye compared to the other two samples which were from the central portion of the eye. Secondly, the excluded fish showed significant tearing between the RPE and photoreceptor OS (Fig. 3.11D, asterisk) which may have been due to the buildup of vacuoles in that region. Interestingly, the third *pikfyve* crispant fish showed a higher degree of OS disorganization compared to the two other fish studied. Some OSs appeared globular rather than cone or rod-shaped and others were abnormally overgrown into the RPE (Fig. 3.11D, red arrow). Overall, the distinction between the RPE and photoreceptor OS layer was nebulous with some areas of the RPE overgrowing into the OS layer and some OSs overgrowing into the RPE.

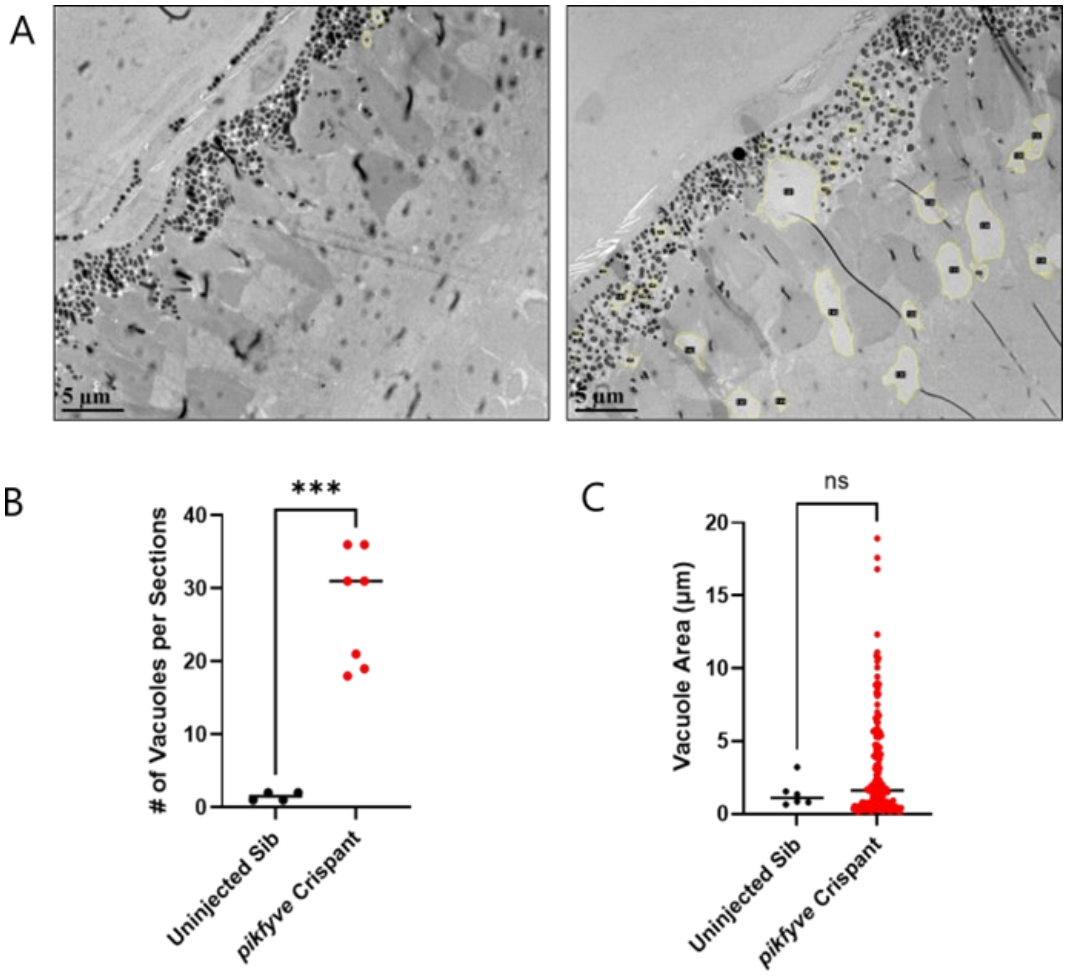
A
5 µm
5 µm
B
***
# of Vacuoles per Sections
40
30
20
10
0
Uninjected Sib
pikfyve Crispant
C
ns
Vacuole Area (µm)
20
15
10
5
0
Uninjected Sib
pikfyve Crispant
D
5 µm

Figure 3.11 – Vacuolization and abnormal retinal organization in *pikfyve* crispants. (A) Retinal vacuoles were analyzed in two control (left panel) and two *pikfyve* crispant (right panel) fish. Vacuole numbers (A) and area (B) were measured in ImageJ. (D) cross section of *pikfyve* crispant fish excluded from above analysis showing significant tearing in the RPE (asterisks) and overgrowth of photoreceptor outer segments (red arrow). ***p<0.001.

3.6.4 Impaired phagosome degradation in RPE

Packets of photoreceptor discs are shed daily from the apical OS tips and engulfed by cells of the RPE. Phagocytosed OSs are then degraded through phagosome maturation and fusion with lysosomes. I hypothesized that *pikfyve* is involved in OSs phagocytosis and/or degradation of phagosomes. Therefore, I used TEM to determine if *pikfyve* mutagenesis impairs the RPE's phagocytic and degradative capacity. Abnormal accumulation of discs at the distal tips of the OS may indicate impaired RPE phagocytosis, while the presence of shed OS discs within the RPE may indicate impaired RPE degradative capacity.

As shown in Fig. 3.12A, I detected the presence of photoreceptor OS discs within the RPE of *pikfyve* crispants but not in the uninjected siblings. OS discs phagocytosed by the RPE are typically degraded within hours, and therefore are not often found in RPE of control fish (Lakkaraju et al., 2020). The amount and size of OS material in the RPE varied between fish, but the finding was consistent in all three *pikfyve* crispants analyzed. The OSs appeared to have been phagocytosed normally by the RPE; however, their accumulation indicates impaired RPE degradative capacity. Taken together, my TEM findings provide valuable insight into the roles of *pikfyve* in the retina. Specifically, I determined that *pikfyve* is important in maturation of

melanosomes, degradation of phagosomes containing photoreceptor OS discs, and overall RPE and photoreceptor health.

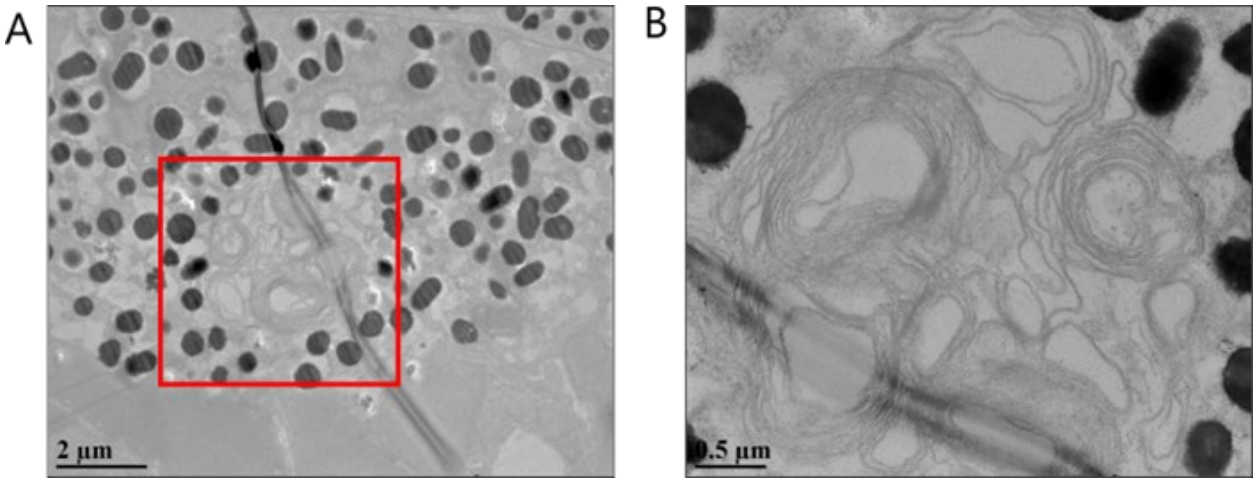

Figure 3.12 – Impaired RPE degradative capacity in *pikfyve* crispants. (A) Photoreceptor OS material was detected in the RPEs of all three *pikfyve* crispants, but not in the controls. (B) Higher magnification of the view of the engulfed OS material shown in the red box in panel A, demonstrating normal phagocytosis of OS by the RPE but impaired degradation.

3.7 Characterization of retinal vacuoles in *pikfyve* crispant zebrafish

While TEM provides valuable insight into retinal ultrastructure, it is difficult to identify the nature of vacuoles without the use of markers. Therefore, I used immunohistochemistry to label retinal cryosections and examine the presence and nature of vacuoles in the RPE. I utilized the anti-microtubule-associated protein light chain 3 (LC3) antibody as a marker of autophagosomes and phagosomes. LC3-I is present in the cytoplasm and LC3-II is membrane-bound and consists of LC3-I conjugated to phosphatidylethanolamine (Koukourakis et al., 2015). LC3-II is commonly used as an autophagy marker since it is distributed across the

autophagosome membrane. Moreover, LC3 can also be used as a phagosome marker for LC3-associated phagocytosis (LAP) as discussed in section 1.1.2.5.1. Here, I used anti-LC3-II as a marker of autophagosomes and LAP phagosomes within the RPE. I hypothesized that *pikfyve* crispants would show differences in LC3 staining compared to controls. In particular, I looked for the presence of enlarged, LC3-labeled puncta in the RPE, which would indicate impaired maturation of phagosomes or autophagosomes.

Upon confocal examination of retinal cryosections, I observed that *pikfyve* crispant retinas were more fragile than controls and showed significant tearing in the RPE as shown by the red arrow in Fig. 3.13B (bright field panel). In contrast, control RPEs remained intact during sectioning with little-to-no tearing observed. I suspect that RPE inflammation and/or vacuolization may be contributing to the increased tearing observed in *pikfyve* crispants. Of note, tissue damage because of tearing likely impeded my ability to fully characterize LC3-labeled puncta in the RPE. Another challenge I encountered with immunohistochemistry was background staining. As shown in the LC3 panels in Fig. 1.13A-B, LC3 stains the photoreceptor OS. When combined with section tearing in the surrounding region, it became increasingly difficult to differentiate background staining of photoreceptor OSs from LC3-labelled puncta indicative of autophagosomes and/or phagosomes in the RPE. Nevertheless, I devised a protocol to analyze number and size of puncta by first blinding the images and then individually editing images in Paint 3D to black out photoreceptor OSs. Edited images were then analyzed in ImageJ. As shown in Fig. 1.13C, there was no statistically significant difference in the number of LC3-labeled puncta in the RPE between the two groups although on average, *pikfyve* crispants showed a slightly higher number. Moreover, the size of LC3-labeled puncta was comparable between *pikfyve* crispants and controls (Fig. 1.13D). Of note, while editing the images individually

eliminates the majority of photoreceptor OS background staining from quantification, the distinction between OS and puncta in the RPE was not always clear and therefore, it is possible that some of the puncta analyzed in either group were background-stained OSs. In *pikfyve* crispants distinct LC3-puncta were observed more frequently in the more basal (outer) region of the RPE, consistent with delayed processing of phagosomes (Fig. 3.13A-B, high mag panel). In summary, these observations suggest that *pikfyve* crispants likely exhibit some impairment in autophagy and phagosome maturation as demonstrated by the slightly higher number of LC3-labeled puncta and their presence in the outer RPE. Nonetheless, it is difficult to conclude with certainty due to the limitations of immunohistochemistry as discussed.

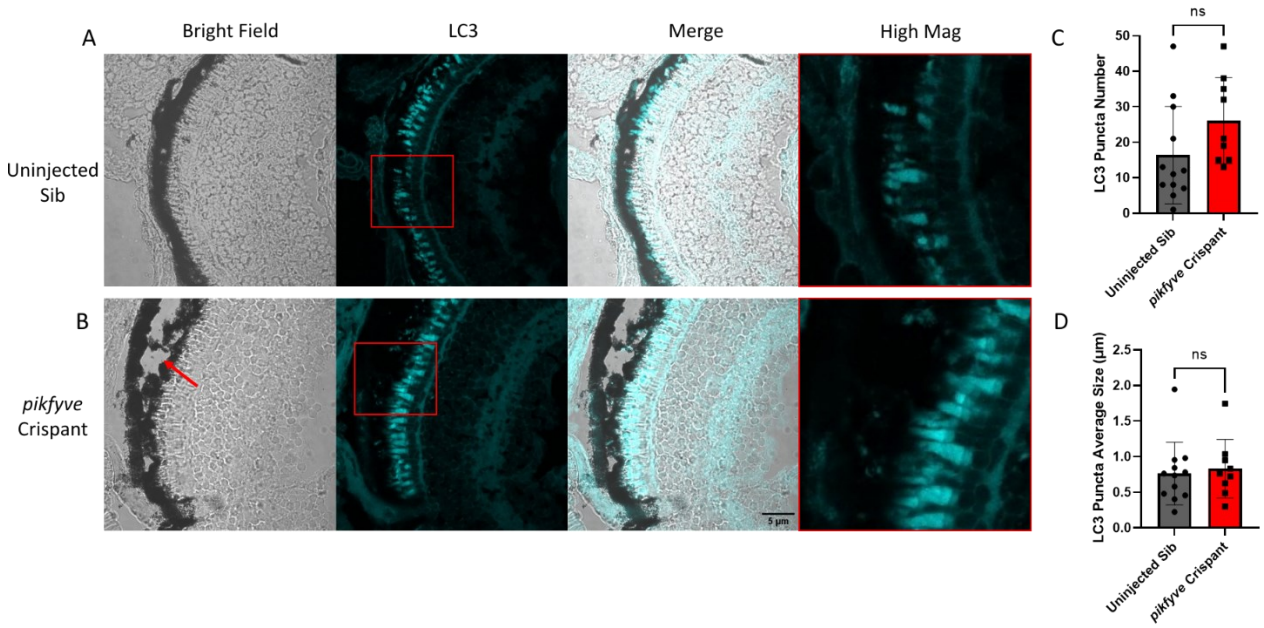

Figure 3.13 – LC3 staining in *pikfyve* crispants retinas. I performed immunohistochemistry on (A) control uninjected siblings and (B) *pikfyve* crispants at 5 dpf. I quantified (C) the number of LC3-labelled puncta in the RPE and (D) the average size of the puncta. Quantification was done on three *pikfyve* crispants and four uninjected controls. Three images were taken of the retina per

fish using a 63X objective and thus, three measurements per fish were made. The red arrow points to RPE tearing and the red box highlights the region magnified in the rightmost panel in (A) and (B).

3. 8 Summary of findings

Taken together, my analysis of *pikfyve* crispants provides valuable insight into the roles of *pikfyve in vivo*. I first showed that knockdown of *pikfyve* with CRISPR/Cas9 results in morphological abnormalities such as edema, improper swim bladder development, and small body length. I also confirmed that *pikfyve* knockout is embryonic lethal by 7 dpf in zebrafish. I then showed that *pikfyve* mutations have a detrimental effect on cone photoreceptor electrical function in zebrafish. I observed normal development of all retinal layers in *pikfyve* crispants, albeit with some differences compared to uninjected siblings. Moreover, I found that *pikfyve* knockdown increased apoptotic cell death, particularly in proliferative cells, including those in the CMZ and brain. My TEM analysis revealed a range of retinal ultrastructure abnormalities in *pikfyve* crispants including OS shortening, RPE expansion, impaired melanosome formation, retinal vacuolization, and impaired RPE degradative capacity as evident by the accumulation of OS material. I attempted to utilize immunohistochemistry to characterize vacuoles within the retina, but larger sample sizes and more reliable quantification techniques are needed in the future.

CHAPTER FOUR: Pikfyve INHIBITION IN ZEBRAFISH

4.1 Introduction

While CRISPR/Cas9 mutagenesis provides valuable insight into the importance of Pikfyve in the zebrafish retina, there are some limitations associated with studying *pikfyve* crispants. Firstly, I studied the F0 generation due to the embryonic lethality of gene knockout and inability to produce a stable heterozygous line. Therefore, the fish analyzed carried a variety of different mutations, some of which may have been more severe than others. Further, the percentage and type of cells lacking Pikfyve function would have been different for each fish. Consequently, variation within *pikfyve* crispants is highly likely since the severity of the phenotype is dependent on the nature and frequency of the mutations introduced. Nevertheless, the high larval mortality rate suggests efficient mutagenesis. The second limitation to using the *pikfyve* crispants is that the phenotypes observed are more severe than those observed in the patient, who carries a heterozygous missense mutation. As a result, the ability to extend my findings from *pikfyve* crispants to the human patient is limited. To address some of these limitations, I utilized pharmacological inhibition of PIKfyve using the potent and specific inhibitor, apilimod (Gayle et al., 2017). In contrast to CRISPR/Cas9 mutagenesis, pharmacological inhibition is titratable, giving more control over the severity of the phenotype observed through adjusting the concentration of inhibitor to which the fish are exposed. I can also begin exposure after the embryonic period is complete, and thereby test the importance of PIKfyve in cellular function rather than in early development. Moreover, pharmacological inhibition decreases variability within the experimental group since all fish are exposed to the same dose of the drug. Finally, apilimod is in clinical trials for cancer and neurodegeneration, and therefore studying its effects on the retina *in vivo* is especially important.

4.2 Apilimod delays and decreases photopic light responses in zebrafish larvae

Work done by Ifrah Anjum, an undergraduate student in our laboratory, to determine the optimal concentration of apilimod treatment revealed that a concentration of 500 nM produced a visible phenotype in zebrafish without being lethal to larvae over a two-day exposure period. Interestingly, this is significantly lower than the concentrations commonly used in zebrafish drug studies, which average around 10 μM (Wiley et al., 2017). In agreement with my CRISPR findings, the lethality of low doses of apilimod in zebrafish embryos highlights its important role in development.

Zebrafish embryos were initially treated with 500 nM apilimod from 4-6 dpf; however, the timeline was shifted to 5-7 dpf following observations that later exposure is better tolerated by zebrafish. Apilimod-treated zebrafish exhibited similar morphological and behavioral abnormalities to *pikfyve* crispants, developing edema and showing decreased responses to physical stimuli. I examined the retinal visual function of apilimod-treated zebrafish at 6 dpf to determine if *pikfyve* inhibition impaired retinal electrical function. Fish were treated with 500 nM apilimod for two days prior to photopic ERG testing to assess cone electrical function.

As shown in Fig. 4.1B, while electrical responses were recorded from both treated and control fish, treated fish showed impaired responses to light. The a-wave of apilimod-treated fish was significantly diminished and delayed compared to DMSO controls (Fig. 4.1E-F), indicating delayed and reduced hyperpolarization of cone photoreceptors in response to light. Moreover, the b-wave of apilimod-treated fish was also delayed and diminished compared to DMSO controls (Fig. 4.1C-D). The b-wave represents depolarization of downstream bipolar cells, which is delayed and reduced in apilimod-treated fish secondary to delayed and reduced photoreceptor

hyperpolarization. Taken together, these findings demonstrate that inhibition of PIKfyve results in impaired cone electrical responses to light.

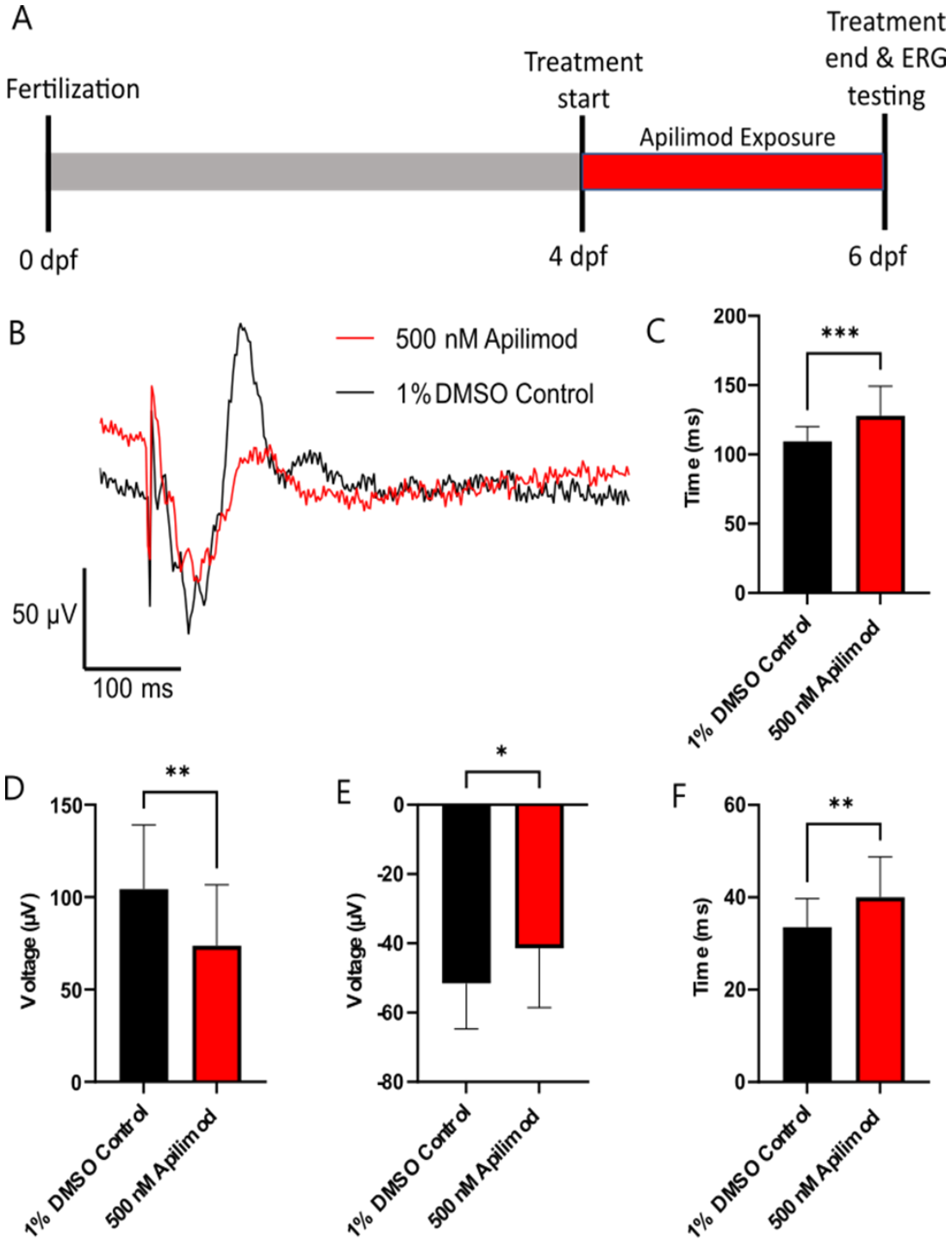

Figure 4.1 – Inhibition of PIKfyve impairs visual function *in vivo.* (A) Schematic of apilimod exposure. Zebrafish embryos were exposed to 1% DMSO or 500 nM apilimod in 1% DMSO from 4 days post fertilization (dpf) until 6 dpf. The drug was removed at 6 dpf and retinal electrical function was tested with electroretinography (ERG). (B) Representative apilimod-treated and DMSO-treated ERG traces. (C) Delayed B-waves in apilimod-treated zebrafish. (D) Reduced B-wave amplitude in apilimod-treated fish. (E) Reduced A-wave amplitude in apilimod-treated fish. (F) Delayed A-waves in apilimod-treated fish. Apilimod-treated group n=23, DMSO control group n=22. *p<0.05; **p<0.01; ***p<0.001.

4.3 Apilimod increases lysosomal staining in zebrafish larvae

The most common finding associated with inhibition of PIKfyve is enlarged lysosomes. As discussed in section 1.3.2.1, PIKfyve plays an important role in maintaining lysosomal homeostasis and therefore its inhibition impairs lysosomal function through mechanisms not fully understood. I sought to analyze the effect of Pikfyve inhibition *in vivo* on lysosomes in zebrafish larvae. LysoTracker is a fluorescent stain for acidic organelles that is commonly used in live imaging to label and trace lysosomes. I stained apilimod-treated and untreated zebrafish larvae with LysoTracker at 7 dpf for one hour prior to euthanasia. Sagittal cryosections were then prepared and imaged to detect lysosomes across the zebrafish body.

I detected little staining in the tail and middle region of the body in both treated and untreated zebrafish. Staining was detected in the brain, eye, pancreas, and liver of both treated and untreated zebrafish (Fig. 4.2A). There was significantly more staining in apilimod-treated zebrafish compared to DMSO controls as shown in Fig. 4.2B, particularly in the pancreas and liver (Fig. 4.2A). The size of LysoTracker-stained puncta was not significantly different between

the two groups, although it was slightly higher in apilimod-treated fish. Of note, only three fish per group were analyzed and therefore, variation had a remarkable effect on the data. In the future, a larger sample size would be useful in reducing the impact of variation on the data. Moreover, tissue folding during sectioning may have also impacted the number and size of puncta quantified. Since LysoTracker is added to live zebrafish, in the future imaging of live zebrafish could be done using fluorescent stereoscopy and pigmentless fish to better analyze lysosomes throughout the whole body.

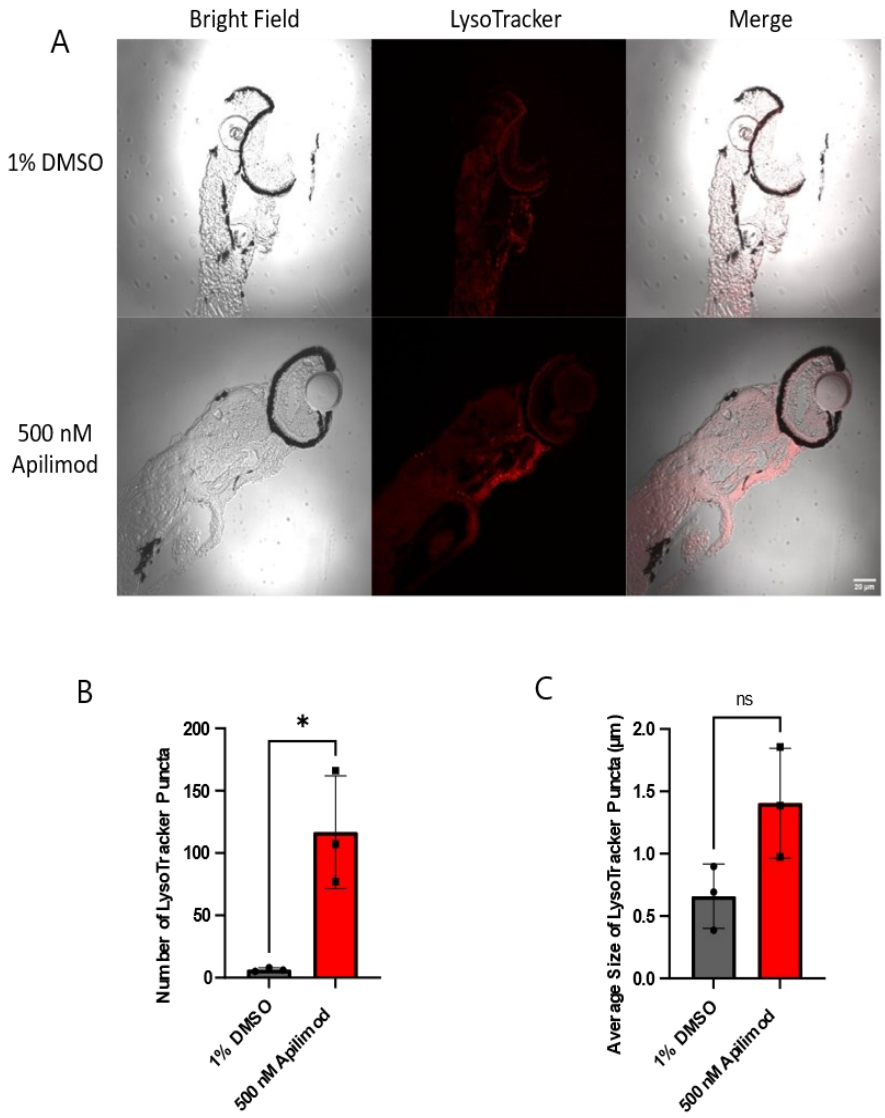

Figure 4.2 – Increased LysoTracker staining in apilimod-treated zebrafish. (A) Zebrafish were treated with 500 nM apilimod or 1% DMSO from 5 to 7 dpf and stained with LysoTracker for one hour prior to euthanasia. Sagittal cryosection were imaged with confocal microscopy and (B) the number and (C) size of LysoTracked-labeled puncta in the region containing the brain, eyes, pancreas, and liver was quantified in ImageJ.

4.4 Apilimod increases cell death in brain and eyes of zebrafish larvae

To further elucidate the mechanism underlying the impaired retinal electrical activity observed in apilimod-treated zebrafish, I performed a TUNEL assay to assess if increased cell death could be a contributing factor. Zebrafish treated with apilimod or DMSO from 5 to 7 dpf were euthanized and a TUNEL assay was performed on transverse sections through the head to visualize both eyes and brain.

I detected little staining in the brain and eyes of DMSO controls (Fig. 4.3A). Conversely, apilimod-treated fish showed a significantly higher number of TUNEL-positive cells in both the brain and eyes (Fig. 4.3B-C). The location of the staining was similar to that observed in *pikfyve* crispants. With respect to the brain, staining was observed in the dorsal region. I detected staining in the front of the eye particularly in the cornea, iris, and surrounding the lens. Staining was also detected in the CMZ of the peripheral retina in apilimod-treated fish. In contrast to *pikfyve* crispants, some TUNEL labeling was detected in the central retina, particularly in the RPE/OS layer (Fig. 4.3A). Taken together, these findings show that Pikfyve inhibition increases cell death in the brain and various ocular tissues in zebrafish.

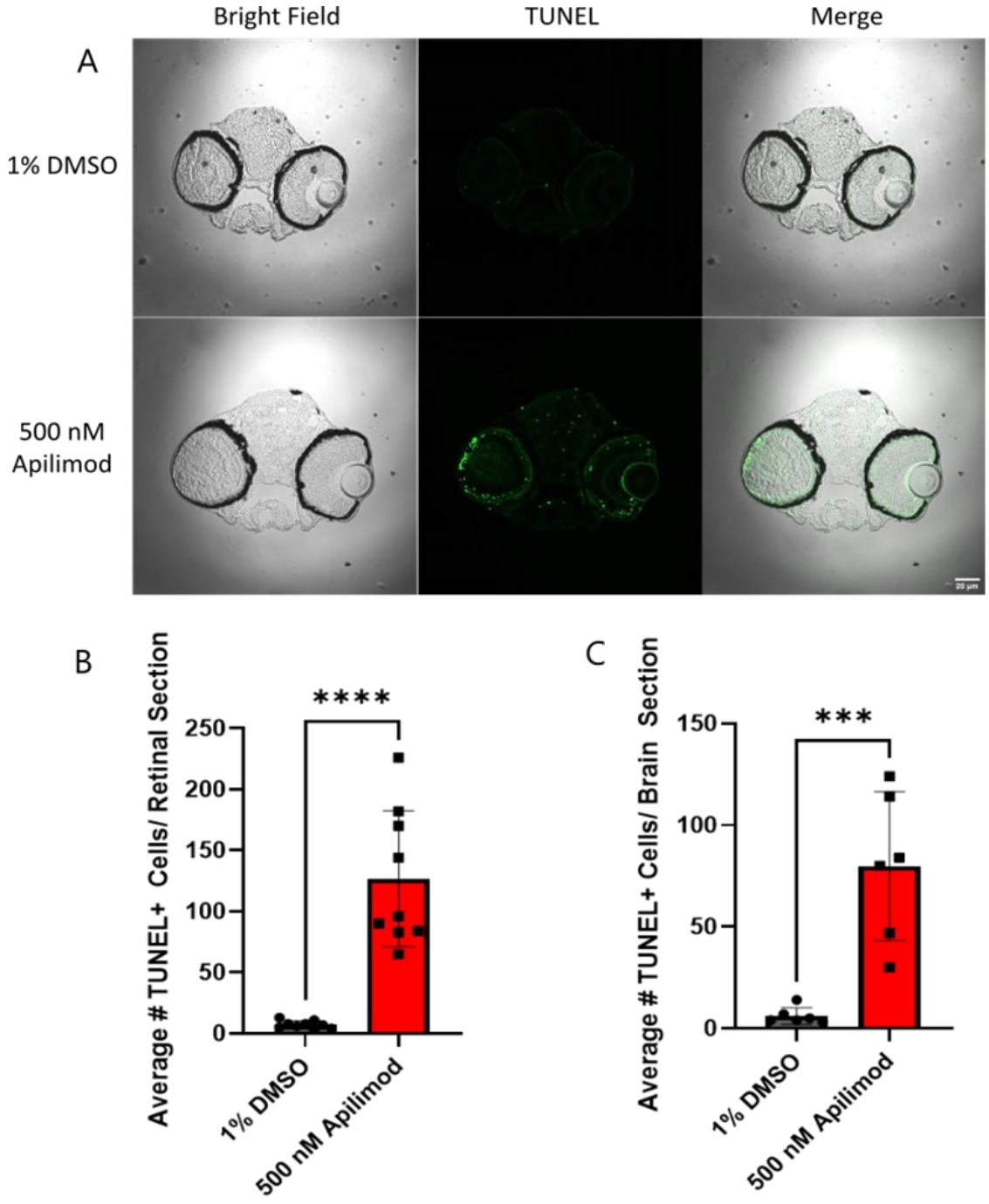

Figure 4.3 –Apilimod increases cell death in eyes and brain of zebrafish larvae. (A) TUNEL assay was performed on transverse sections from apilimod-treated and DMSO control fish. A significantly higher number of TUNEL positive cells was observed in (B) the eye and (C) the

brain of apilimod-treated zebrafish. 1% DMSO n=6 fish; 500 nM apilimod n=6 fish. ***p<0.001; ****p<0.0001.

4.5 Retinal ultrastructure of apilimod-treated zebrafish larvae

4.5.1 Vacuolization of RPE and photoreceptor layer

To get a better understanding of the effect of Pikfyve inhibition on retinal ultrastructure, I performed TEM on zebrafish treated with apilimod from 5-7 dpf and DMSO controls. I detected the presence of large vacuoles in the photoreceptor inner segment region and RPE of apilimod-treated fish (Fig. 4.4B), but not in the DMSO control (Fig. 4.4A). Vacuoles were observed throughout the retina of the apilimod-treated fish with no particular increase in the central versus the peripheral retina. Quantification of vacuole area and number was not done as one fish per group was analyzed.

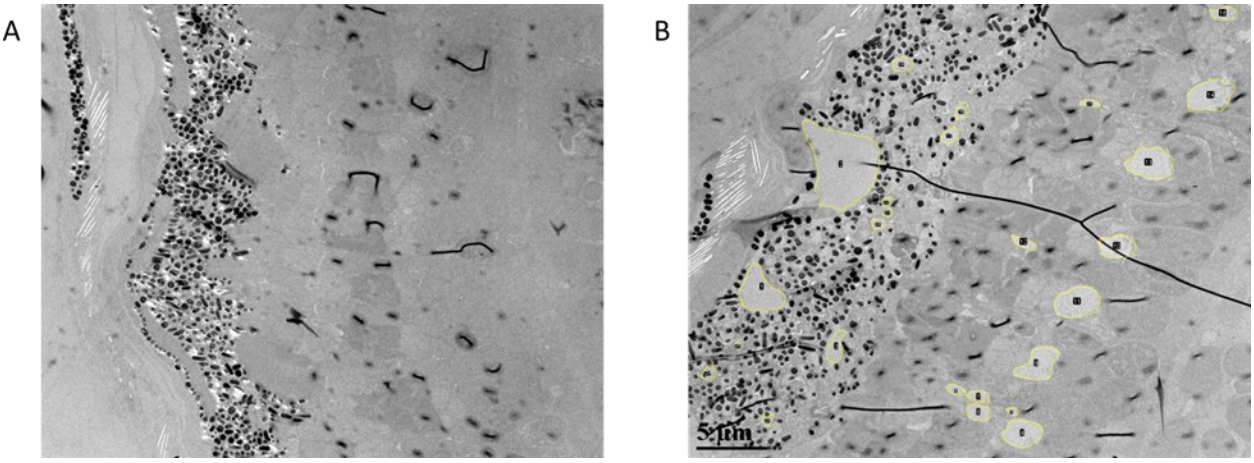

Figure 4.4 – Pikfyve inhibition causes retinal vacuolization. Zebrafish were exposed from 5-7 dpf to (A) 1% DMSO or (B) 500 nM apilimod. Disruption in the RPE and photoreceptor layer was observed in apilimod-treated fish TEM. Yellow circles highlight vacuoles in the RPE and inner segments of apilimod-treated fish.

4.5.2 RPE hypertrophy and impaired OS degradation

Beyond the formation of vacuoles in the retina, I found that Pikfyve inhibition caused a range of abnormalities, particularly in the RPE and photoreceptor OS layer. RPE layer thickness was inconsistent throughout the retina, with regions extending abnormally into the photoreceptor OS layer. As a result, photoreceptor OS were less organized compared to DMSO controls. Moreover, I observed significant accumulation of shed photoreceptor OSs in the RPE. OS aggregates were observed in two locations: in the inner RPE near the photoreceptor OS (Fig. 4.5B) and in the outer RPE (Fig. 4.5C). The significance of the location of photoreceptor OS within the RPE will be discussed later. Taken together, these observations suggest that PIKfyve is critical to the RPE's ability to degrade shed OS disks and maintain overall RPE and photoreceptor health.

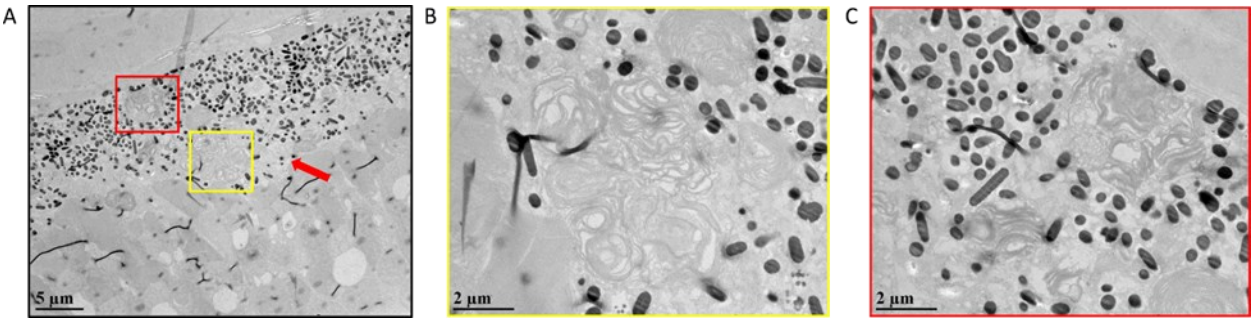

Figure 4.5 – Pikfyve inhibition causes RPE hypertrophy and impaired OS degradation. (A) Low magnification view of TEM retinal cross section from apilimod-treated zebrafish. (B) High magnification view of aggregates of shed OS disks in the inner RPE. (C) High magnification view of aggregates of shed OS disks in outer RPE. The red arrow points to an area of RPE hypertrophy. Yellow and red boxes highlight areas magnified in B and C, respectively.

4.6 Characterization of retinal vacuoles in apilimod-treated zebrafish larvae

4.6.1 Apilimod causes RPE degeneration

To get a better understanding of changes in RPE morphology because of PIKfyve inhibition, I used anti-ZPR2 antibody to label RPE cells (Yazulla and Studholme, 2002). I treated fish with apilimod (or DMSO) from 5 to 7 dpf and kept them in constant light for the duration of exposure. Light induces the production of reactive oxygen species (ROS), which are typically cleared by antioxidants such as glutathione in the RPE. In the case of persistent light exposure, oxidative damage to organelles is accelerated due to increased production of ROS. In healthy RPE cells, oxidatively damaged organelles are degraded through autophagy. Given the involvement of PI5P and $PI(3,5)P_2$ in autophagy, I hypothesized that in constant light, Pikfyve inhibition will result in the accumulation of damaged organelles, which will decline RPE health and potentially cause degeneration. Using ZPR2 staining and bright-field examination, I analyzed differences in RPE architecture and integrity in DMSO and apilimod-treated zebrafish larvae following two days of constant exposure to light. In addition, I dark-adapted zebrafish for four hours prior to fixation. Light onset and offset both trigger OS disc shedding while constant light inhibits this process (Moran et al., 2022). Thus, by taking advantage of the light-sensitive nature of OS disc shedding, I utilized constant light to inhibit OS disc shedding and then stimulated it through dark-adaptation.

In dark-adapted conditions, I found that thickness was inconsistent across the RPE layer in apilimod-treated fish as shown in Fig. 4.6A, with areas of expansion consistent with findings from *pikfyve* crispants. I observed a significant decrease in ZPR2-staining (Fig. 4.6B) in apilimod-treated compared to control DMSO fish. Moreover, I observed holes in the RPE of apilimod-treated zebrafish (Fig. 4.6A, red arrow) that corresponded with loss of ZPR2 staining in

the area. Disrupted ZPR2 staining can be used as an indicator of RPE degeneration (Hanovice et al., 2019), and therefore, decreased ZPR2 staining in apilimod-treated fish may be indicating decreased health and/or RPE cell death, which is supported by the holes observed in the bright-field images. Of note, as discussed in section 4.4, TUNEL staining was largely observed in the retinal periphery and not in the RPE. Thus, it is possible that the holes observed here are areas of non-apoptotic cell death (which would not be detected with the TUNEL assay). It is also possible that the holes observed are neither areas of apoptotic nor non-apoptotic cell death, but rather vacuoles in the RPE. My TEM observations (Fig. 4.4) support the latter hypothesis. Together, these findings show that Pikfyve inhibition causes significant changes in the RPE layer when fish are exposed to constant light followed by dark-adapted conditions.

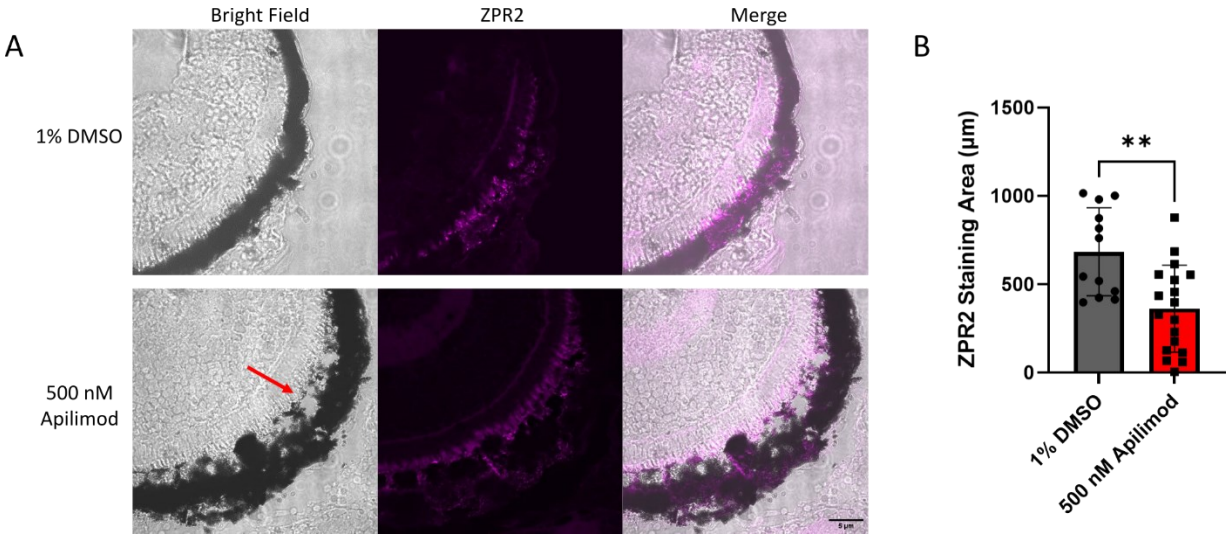

Figure 4.6 – Decreased ZPR2 staining in apilimod-treated zebrafish larvae. (A) Confocal images of retinal cross sections from dark-adapted fish treated from 5-7 dpf with apilimod or DMSO. ZPR2 is an RPE marker and (B) shows ZPR2 staining area quantified in ImageJ. Dark-adapted 1% DMSO n=4, 3 measurements/fish; dark-adapted 500 nM apilimod n=6 fish, 3 measurements/fish. **p<0.01.

4.6.2 Autophagosomes and phagosomes

PIKfyve inhibition in macrophages has been shown to impair phagocytosis and phagosome maturation (Kim et al., 2014). Moreover, PIKfyve inhibition results in impaired autophagy and the accumulation of autophagosomes, as shown in HeLa cells (de Lartigue et al., 2009). I sought to study the effect of PIKfyve inhibition on autophagy and phagocytosis in the RPE of zebrafish. Zebrafish were kept in constant light from 5-7 dpf followed by dark adaptation for four hours to trigger OS shedding. One group was treated with 500 nM apilimod, and the control group was kept in 1% DMSO from 5-7 dpf. As described above, constant light increases autophagic demand due to increased photooxidative damage to organelles. I hypothesized that apilimod-treated fish would show increased RPE damage because of Pikfyve inhibition impairing autophagy. Moreover, as evident by the TEM findings (Fig. 4.5), I hypothesized that degradation of phagosomes containing OS material would be impaired in the RPEs of apilimod-treated fish. Thus, to assess these hypotheses, I used anti-LC3 antibody to label autophagosomes and LAP phagosomes in the RPE.

Like observations made with *pikfyve* crispants, I detected background staining of photoreceptor OSs with anti-LC3 antibody. Images were blinded and edited to manually remove OS background staining. The remaining LC3 staining in the PRE was quantified in ImageJ. I did not find a significant difference in LC3-stained puncta number or size between apilimod-treated and DMSO control fish in dark-adapted conditions, although on average, apilimod-treated fish had slightly higher numbers and size of LC3-stained puncta. As shown in Fig. 4.7A-B, I detected the presence of LC3-stained puncta in the outer RPE of apilimod-treated fish but not DMSO controls. Together, these findings suggest that Pikfyve inhibition interferes to some extent with

phagosome and/or autophagosome maturation in zebrafish RPEs. However, quantification of the degree of interference is difficult due to the limitations of immunostaining.

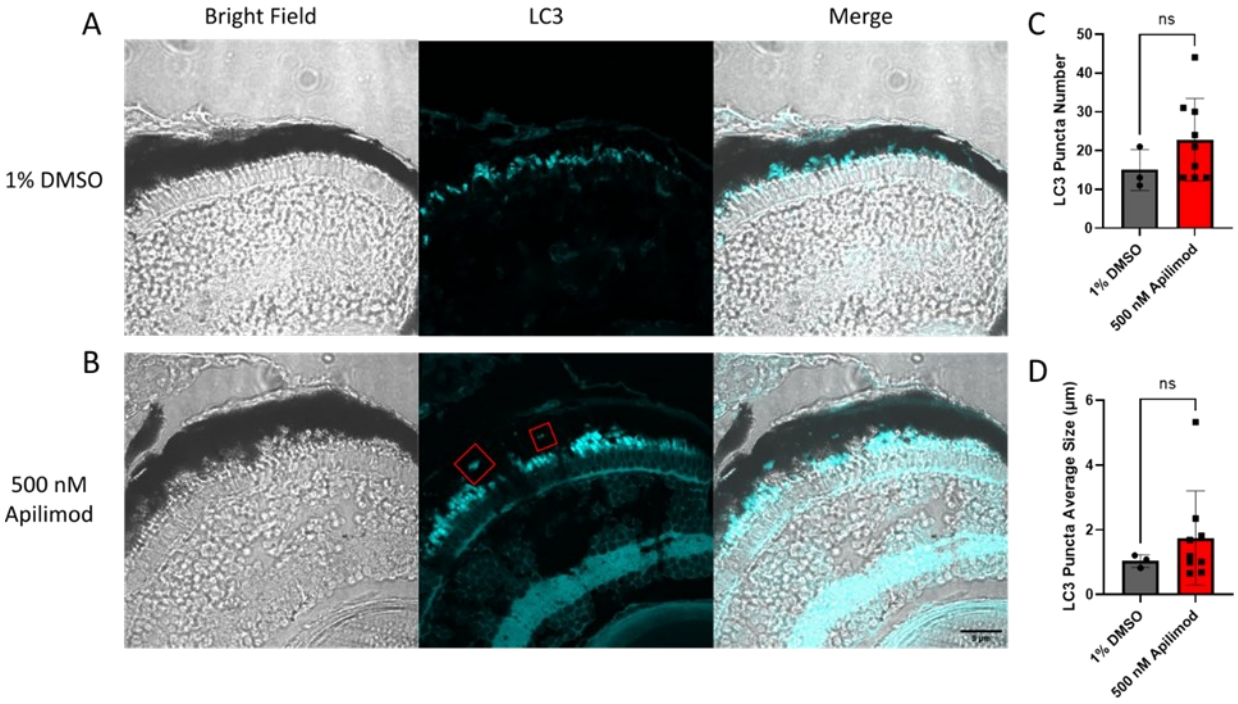

Figure 4.7 – Effect of Pikfyve inhibition on RPE autophagy and phagocytosis. Zebrafish were kept in constant light from 5-7 dpf in (A) 1% DMSO or (B) 500 nM apilimod and dark-adapted for four hours prior to fixation and analysis. Cryosections were stained with LC3 to label autophagosomes and LAP phagosomes. (C) Number and (D) size of LC3-stained puncta in the RPE was quantified in ImageJ. 1% DMSO n=1, 3 measurements/section; 500 nM apilimod n=3, 3 measurements/section.

4.6.3 Lysosomes

I previously showed that Pikfyve inhibition increased lysosomal staining in zebrafish whole bodies using LysoTracker (Fig. 4.2). I found that the quality of LysoTracker staining in

retinal cross sections was low with a high level of background staining. Therefore, I sought to use immunohistochemistry to analyze lysosomes in the RPE of apilimod-treated fish. Lysosome-associated membrane protein-1 (LAMP1) is routinely used as a marker of lysosomes (Cheng et al., 2018). Therefore, I utilized anti-LAMP1 antibody here to stain lysosomes in the RPE of apilimod-treated and control DMSO fish.

A similar experimental outline to that described in the previous section was done here where zebrafish larvae were exposed to 1% DMSO or 500 nM apilimod from 5 to 7 dpf in constant light. Treated and untreated zebrafish retinas were analyzed following four hours of dark adaptation (Fix. 4.8A, B) or light adaptation (Fig. 4.8C, D). I found a similar phenotype in apilimod-treated fish as described above of an abnormal RPE layer, with inconsistent thickness, the appearance of holes, and increased tissue tearing during sectioning (Fig. 4.8B, D, bright field panel). Moreover, I also detected background staining of photoreceptor OS in all LAMP1-stained sections. Therefore, images were blinded and edited to remove as much OS staining as possible and the remaining RPE staining was quantified in ImageJ. I did not find a statistically significant difference between the number or size of LAMP1-stained punctae in the RPE of light- and dark-adapted treated and untreated fish (Fig. 4.8E-H). The size of LAMP1 stained puncta was slightly higher in apilimod-treated fish in both light conditions and the number was slightly higher only in dark-adapted conditions (Fig. 4.8E). Moreover, in some apilimod-treated fish, I detected the presence of enlarged, LAMP1-labeled puncta in the outer RPE (Fig. 4.8B, D, red box). Taken together, these findings suggest that Pikfyve inhibition results in some lysosomal enlargement in the outer RPE. However, quantification is difficult due to the challenges of RPE pigment, background staining, and fragile nature of the treated sections.

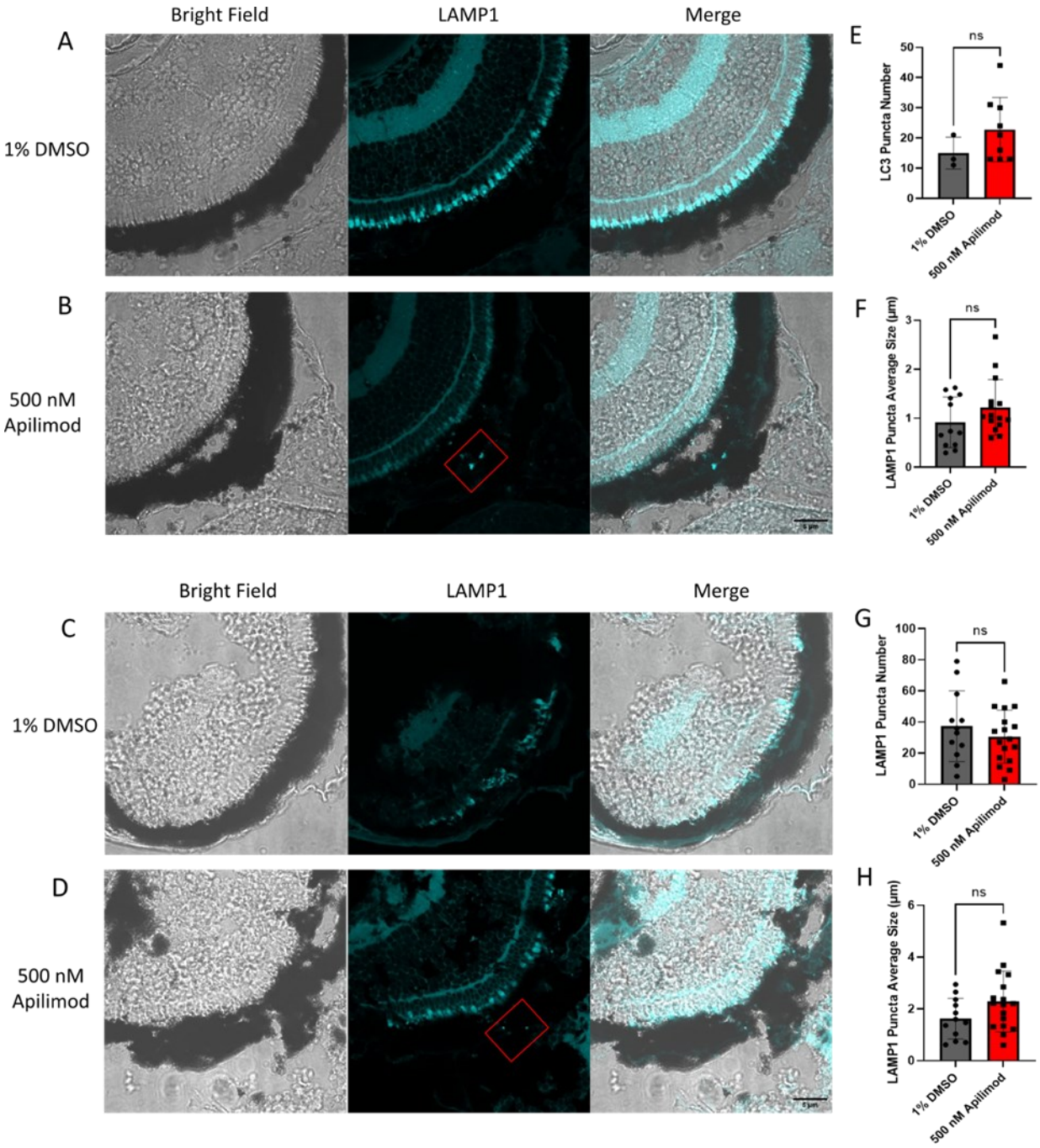

Figure 4.8 – Effect of Pikfyve inhibition on lysosomes in RPE of dark-adapted and light-adapted zebrafish. Zebrafish were treated with apilimod or DMSO from 5-7 dpf and kept in constant light for the duration of exposure. (A) One group was dark-adapted for four hours prior

to fixation and (B) another group was fixed in light-adapted conditions. Retinal cryosections were stained with the lysosomal marker LAMP1. (E, F) show number and size of LAMP1-stained puncta in the RPE of dark-adapted fish while (G, H) show number and size of LAMP1-stained puncta of light-adapted fish. Dark-adapted: 1% DMSO n=4 fish; 500 nM apilimod n=5; light-adapted: 1% DMSO n=4; 500 nM apilimod n=6. 2-3 measurements per fish were made.

4.7 Short term Pikfyve inhibition in adult zebrafish

Studying the role of Pikfyve in the zebrafish retina through CRISPR mutagenesis is limited to the first 7 days of life since gene knockout is embryonic lethal. On the other hand, pharmacological inhibition allows for the study of the effect of short-term Pikfyve inhibition at any time point. I took advantage of this and treated adult one month-post-fertilization (mpf) zebrafish with apilimod for six hours. I sought to analyze if short-term Pikfyve inhibition interfered with lysosomal homeostasis in the RPE. I hypothesized that older zebrafish would tolerate higher concentrations of apilimod and therefore I exposed one group of fish to 500 nM, the highest concentration used previously for larvae, and another to 1 μM apilimod. Further, one set of fish from each group was dark-adapted for the last four hours of treatment to stimulate OS shedding.

4.7.1 Lysosomes

Upon confocal examination of retinal cross sections, I found that the RPE of both 1% DMSO and 500 nM apilimod treated fish were intact, while the RPE of 1 μM apilimod treated zebrafish showed increased damage and tearing. I suspect that the increased tearing is due to buildup of vacuoles within the RPE and/or inflammation due to Pikfyve inhibition. I utilized anti-LAMP1 antibody to stain for lysosomes and, similar to other experiments, I detected

significant background staining of the photoreceptor OSs, which decreased the ability to decipher LAMP1-stained puncta in the RPE. Nevertheless, images were blinded and edited as described above, and the number and size of LAMP1 puncta in the RPE was quantified in ImageJ. I did not detect a significant difference in apilimod-treated compared to control fish in both dark- and light-adapted conditions (Fig. 4.9D, E and Fig. 4.10C, D). There was a trend towards an increased number and size of LAMP1 puncta in the dark-adapted 1 μM apilimod-treated group, but the difference was not statistically significant. Moreover, as shown in Fig. 4.9B, C, I detected the presence of distinct LAMP1-stained puncta in the outer RPE of both 500 nM and 1 μM apilimod-treated fish. Similarly, 1 μM apilimod-treated light-adapted fish also showed distinct LAMP1-stained puncta in the outer RPE although to a lesser extent than in dark-adapted conditions. Although a statistically significant difference was not detected, there was a trend of larger, more numerous LAMP1 puncta in the outer RPE of apilimod-treated fish. Future experiments should focus on improving visualization of stained puncta using pigmentless fish, and optimization of antibody concentrations to decrease background staining and improve quantification.

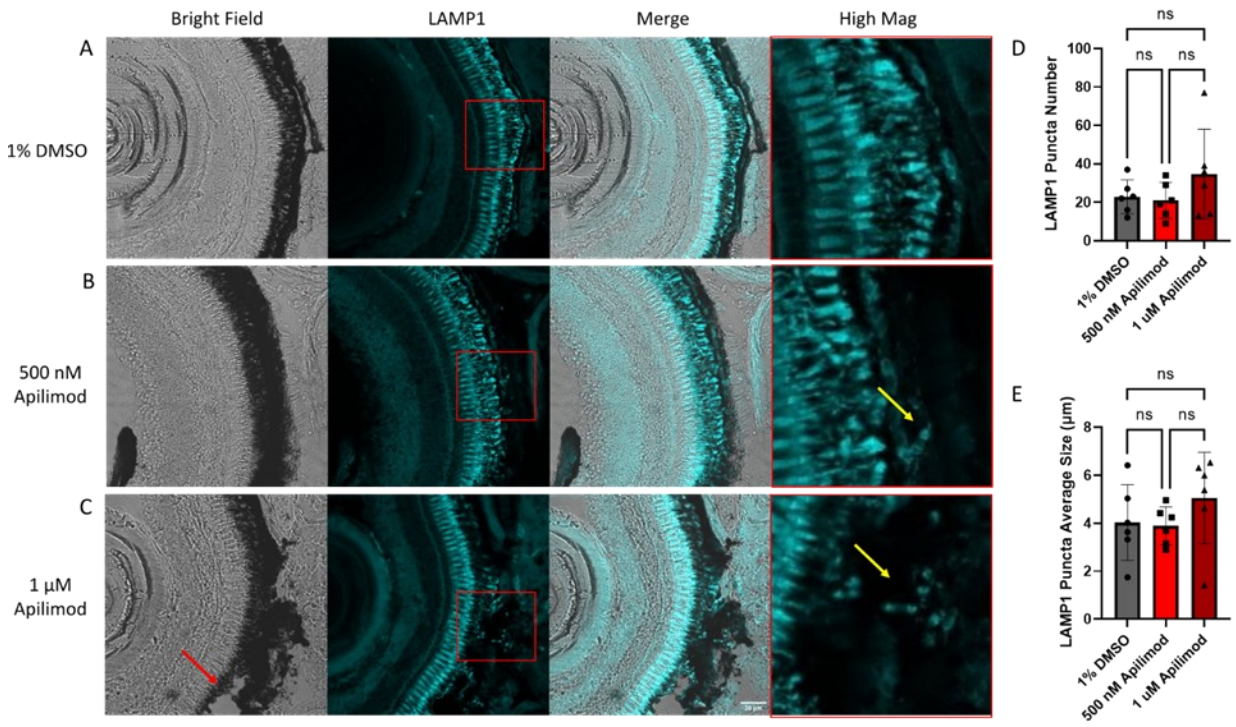

Figure 4.9 – Effect of short-term Pikfyve inhibition on lysosomes in 1 mpf zebrafish in dark-adapted conditions. 1 mpf zebrafish were treated with (A) 1% DMSO, (B) 500 nM apilimod, or (C) 1 µM apilimod for six hours. Fish were dark-adapted for four hours prior to fixing and analysis. Retinal cryosections were stained with anti-LAMP1 antibody to label lysosomes and RPE staining was quantified in ImageJ. (D) The number and (E) size of LAMP1-labelled puncta in the RPE was compared across the groups. Red arrow points to RPE damage and tearing, yellow arrow indicates distinct LAMP1-labelled puncta in the outer RPE, and the red box indicates the area magnified in the leftmost panel. 1% DMSO, 500 nM, and 1 µM apilimod n=2 for each condition; 3 measurements/fish. A one-way ANOVA test was performed with post-hoc Tukey test.

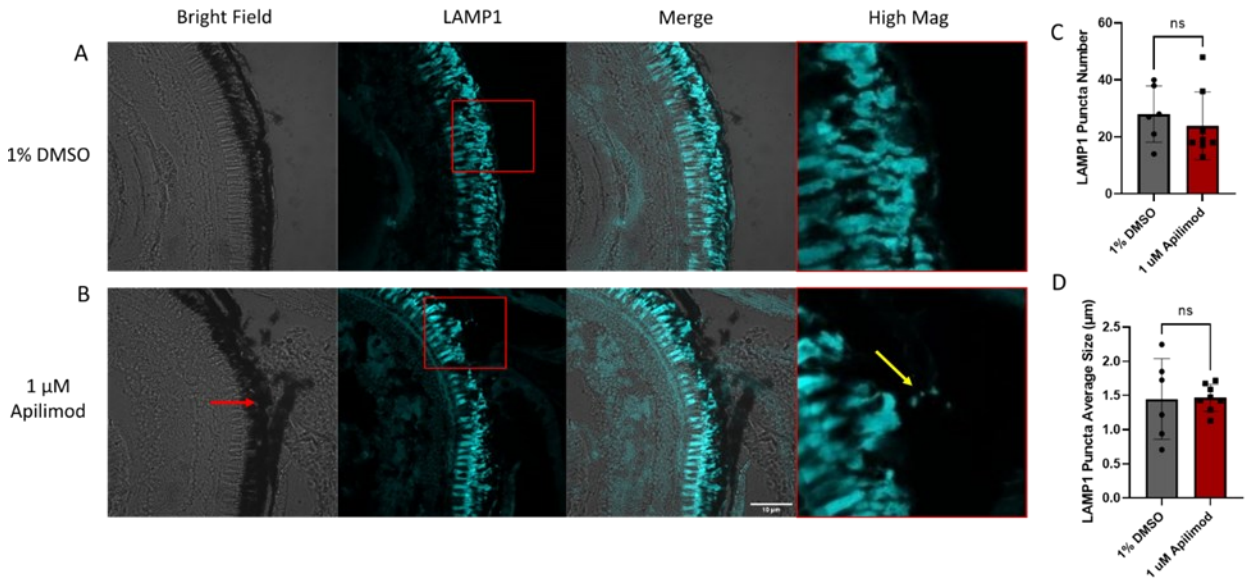

Figure 4.10 – Effect of short-term Pikfyve inhibition on lysosomes in 1 mpf zebrafish in light-adapted conditions. 1 mpf zebrafish were treated with (A) 1% DMSO, (B) 500 nM apilimod, or (C) 1 µM apilimod for six hours. Retinal cryosections were stained with anti-LAMP1 antibody to label lysosomes and RPE staining was quantified in ImageJ. Fish were kept in lit conditions for the entire exposure period. (D) The number and (E) size of LAMP1-labelled puncta in the RPE was compared across the groups. Red arrow points to RPE damage and tearing, yellow arrow indicates distinct LAMP1-labelled puncta in the outer RPE, and the red box indicates the area magnified in the leftmost panel. 1% DMSO n=2 fish; 1 µM apilimod n=3; 2-3 sections analyzed/fish.

4.8 Summary of Findings

Prior to this work, apilimod had never been previously tested in zebrafish. My findings demonstrate that apilimod is highly potent in zebrafish, causing lethality with moderate doses. By decreasing the dose, I characterized various effects of Pikfyve inhibition on the zebrafish

retina. I found that photopic light responses were diminished and delayed in apilimod-treated larvae. The TUNEL analysis demonstrates that apilimod increases cell death in the brain and eyes of zebrafish larvae. Using electron microscopy, I found that short-term inhibition of Pikfyve caused a range of retinal abnormalities. Namely, I detected the presence of vacuoles in the retina and the accumulation of OS material in the RPE indicative of impaired degradative capacity. In cryosections, I observed evidence of RPE degeneration in apilimod-treated zebrafish. I used LC3 and LAMP1 markers to study the effect of Pikfyve inhibition on autophagy, phagocytosis, and lysosomal homeostasis in the RPE. Analysis was limited due to the difficulties associated with quantification and visualization of staining. Nevertheless, the data suggests that Pikfyve inhibition has an effect to some extent on phagosome degradation, autophagy, and lysosomal homeostasis in the RPE. Future experiments should explore the use of transgenic zebrafish lines for LAMP1 and LC3 to overcome the limitations associated with immunostaining.

CHAPTER FIVE: PRECISE GENE EDITING IN ZEBRAFISH

5.1 Introduction

While CRISPR mutagenesis efficiently introduces random mutations in *pikfyve*, the embryonic lethality of gene knockout limits studies to early development. Moreover, apilimod exposure only inhibits PIKfyve for a short duration of time, limiting the ability to study the progressive effect of PIKfyve loss. I was interested in creating a zebrafish model for the retinal dystrophy *PIKFYVE* patient identified by Dr. MacDonald to elucidate the disease mechanism. The patient carries a single base substitution in the *PIKFYVE* gene and therefore, random mutations introduced by CRISPR/Cas9 mutagenesis are not an accurate model of the patient variant. Moreover, while pharmacological inhibition is an efficient method of disruption PIKfyve, it does not aid in understanding the patient variant and associated phenotype. Consequently, I sought to create a patient mimic zebrafish mutant line using precise gene editing technologies to overcome these limitations. I hypothesized that fish carrying the patient mutation will survive into adulthood, at least as heterozygotes, allowing for the study of the progressive effects of the mutation.

5.2 Homology-directed repair

5.2.1 Inefficient repair and random mutations

I first attempted homology-directed repair (HDR) to introduce the patient specific mutation into zebrafish. WES revealed that the patient carried a single base substitution from adenine to guanine that resulted in a missense amino acid change from histidine to arginine p.(His1831Arg) in the first helix of the PIKFYVE kinase domain. The residue mutated in the patient is conserved between human and zebrafish and thus, I sought to introduce the same

adenine to guanine single base substitution with HDR. To simplify detection of the patient mutation in injected zebrafish, I used an HDR template that contained two additional silent mutations, which introduced an XmnI restriction enzyme cut site. The silent mutations were in the two amino acid residues upstream of the histidine mutated in the human patient. Thus, in wildtype fish, the sequence is 5' GAG TTC CAT 3', which encodes glutamic acid, phenylalanine, and histidine, while in HDR-repaired fish the sequence is expected to be 5' GAA TTT CGT 3', which encodes glutamic acid, phenylalanine, and arginine. Single-cell zebrafish embryos were injected with Cas9 protein, a crRNA/trRNA complex that targets the 38th exon of *pikfyve,* and the single-stranded DNA template. DNA was extracted from pools of five injected or uninjected zebrafish embryos and amplified by PCR. The 454 bp PCR fragment was then digested with XmnI restriction enzyme. If HDR repair was successful, XmnI should cut the PCR fragment and generate two fragments of 229 and 225 bp. I used gel electrophoresis to visualize band size relative to a 1 kb DNA ladder. As shown in Fig. 5.1A, I did not detect any fragments around 200 bp in the fish analyzed, indicating no XmnI cutting in HDR-injected zebrafish.

Since HDR efficiency is typically low in zebrafish, it is possible that some HDR repair occurred but not enough to be detected on gel electrophoresis. Thus, I sequenced DNA from individual injected fish to analyze the DNA sequence with higher resolution. As shown in Fig. 5.1B, sequences from HDR injected fish closely resembled those from *pikfyve* crispants, showing a normal, clear sequence upstream of the PAM site, and multiple, noisy sequences downstream of the cut site. This indicates efficient targeting and cutting of the DNA by the crRNA and Cas9 but unsuccessful HDR repair.

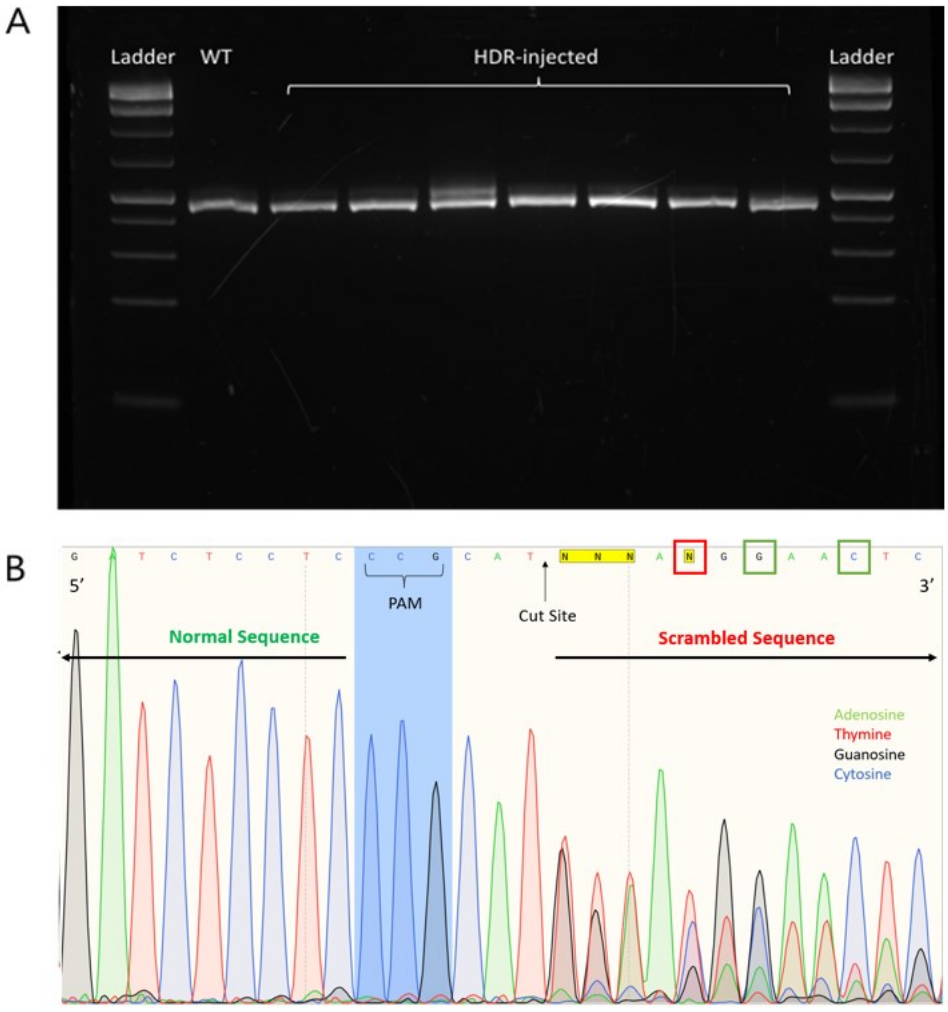

Figure 5.1 – Unsuccessful repair with HDR in zebrafish. (A) RFLP from uninjected (wildtype) and HDR-injected zebrafish. DNA was extracted from pools of five injected and uninjected embryos and the region target by the crRNA was amplified. Samples were then digested with XmnI digest. HDR repair is expected to introduce an XmnI cut site, resulting in two bands at 229 and 225 bp while the uncut fragments are expected to be 454 bp long. (B) Reverse complement Sanger sequencing from the antisense strand of one HDR-injected fish showing scrambled sequence downstream of the cut site. DNA was sequenced with the reverse primer and therefore the sequence shown is the reverse complement of the sense strand. The red

box highlights the residue mutated in the patient while the two green boxes highlight the two silent mutation residues.

5.2.2 Retinal architecture of HDR-injected zebrafish

Genotyping data showed cutting and random mutations in HDR-injected fish with no clear evidence of HDR repair. Therefore, I analyzed HDR-injected fish as *pikfyve* knockdown fish and compared them to uninjected controls to elucidate the importance of *pikfyve* in the eye. I first analyzed retinal architecture with H&E staining.

Seven uninjected and six injected 6 dpf zebrafish were analyzed. Similar to histological findings from *pikfyve* crispants, I found increased tearing, especially in the RPE, in HDR-injected fish (Fig. 5.2A-C). Interestingly, I observed a cataract-like phenotype in two of the six HDR-injected fish with the lens appearing cloudy and opaque (Fig. 5.2B, C). Moreover, injected fish had significantly smaller eyes compared to uninjected siblings (Fig. 5.2D). I quantified the thickness of the retinal layers and found that like *pikfyve* crispants, the IPL and ONL/RPE layer were significantly thinner in injected fish compared to controls (Fig. 5.2F, H). Interestingly, the GCL was significantly thicker in HDR-injected fish compared to uninjected controls (Fig. 5.2E). Moreover, I observed holes in the retinas of HDR-injected fish (Fig. 5.2I, black arrows) and therefore performed a TUNEL assay to confirm if these holes were areas of cell death. Indeed, as shown in Fig. 5.2J, I detected the presence of TUNEL-positive cells in the eyes and brains of HDR-injected fish.

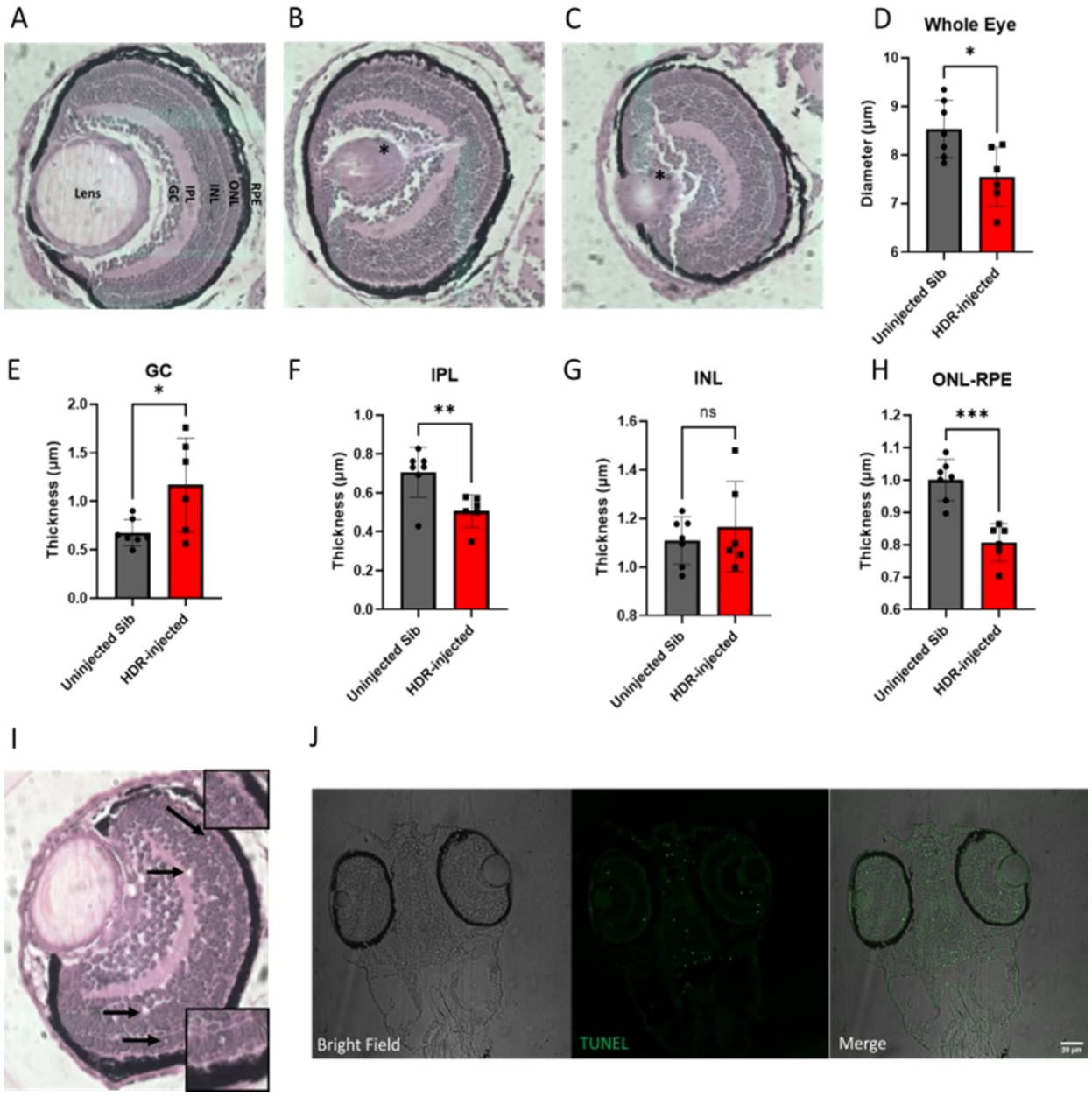

Figure 5.2 – Retinal architecture and cell death in *pikfyve* HDR-injected zebrafish. (A) H&E-stained retinal cross section from control fish with the various retinal layers labeled. (B,C) H&E-stained retinal cross sections from HDR-injected zebrafish, asterisk indicates cataract-like phenotype in lens. (D) Eye diameter was quantified in ImageJ and the thickness of the (E) GCL, (F) IPL, (F) INL, and (H) ONL-RPE was measured. (I) H&E-stained cross section from HDR-injected fish. Black arrows highlight holes in the retina and magnified images are shown. (J)

TUNEL assay from HDR-injected fish. GCL=ganglion cell layer, IPL=inner nuclear layer, INL= inner nuclear layer, ONL=outer nuclear layer, RPE=retinal pigment epithelium. *p<0.05; **p<0.01; ***p<0.001. Uninjected control siblings n=7; HDR-injected n=6.

5.2.3 Vacuole characterization

I performed immunohistochemistry on 5 dpf HDR-injected fish to further elucidate the roles of *pikfyve* in the RPE. I stained retinal cryosections with LC3 as a label for autophagosomes and LAP phagosomes. As shown in Fig. 5.3A, HDR-injected fish showed significant tearing in the RPE while sections from uninjected siblings remained intact. I detected the presence of LC3-labeled puncta in the outer RPE of HDR-injected zebrafish (Fig. 5.3A, middle panel) and therefore, I quantified the number and size of staining in the RPE. As previously discussed, LC3 stains the photoreceptor OS and therefore, images were blinded and edited to remove as much background staining of OSs before quantification. I found that while the number of LC3-stained puncta in the RPE was comparable between uninjected and injected zebrafish, the average size of LC3-stained puncta was significantly larger in HDR-injected fish (Fig. 5.3B, C). Taken together, these findings support the hypothesis of Pikfyve mediating autophagy and phagocytosis in the RPE.

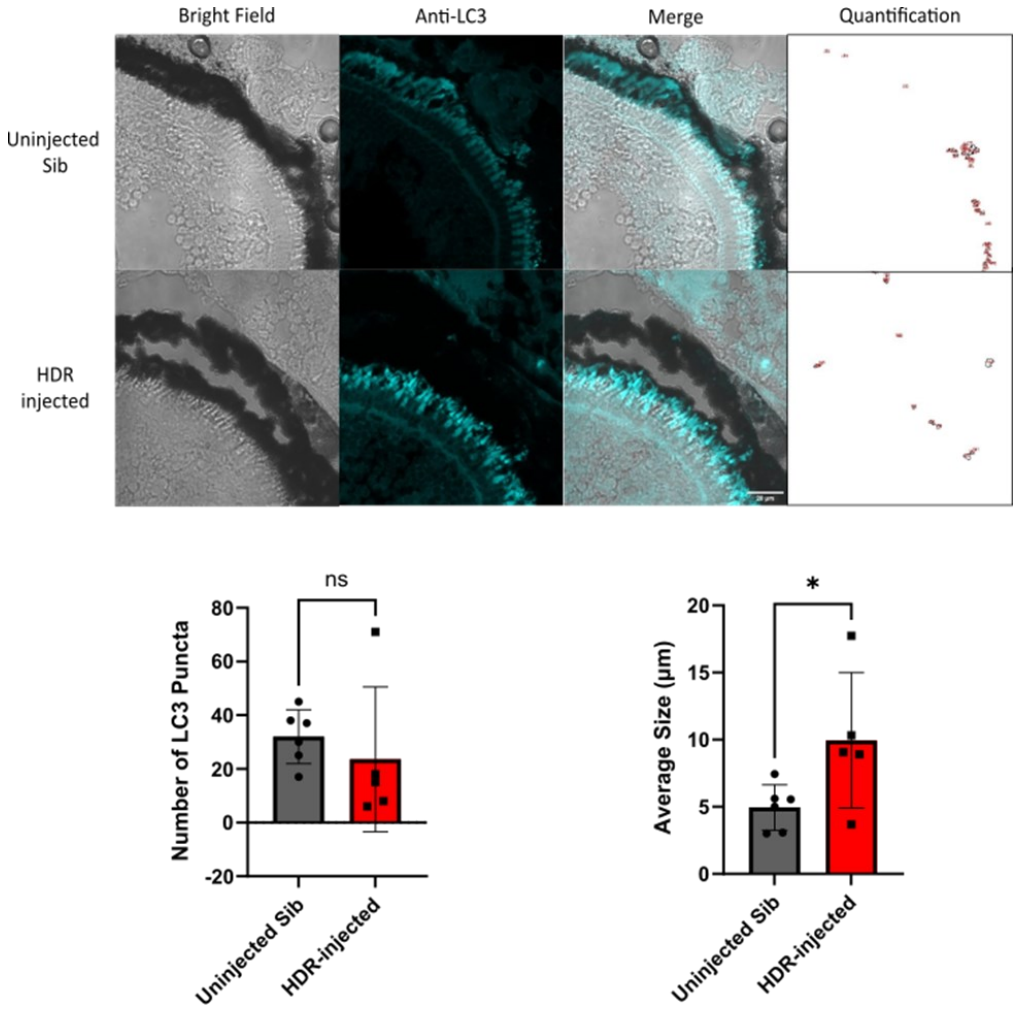

Figure 5.3 – LC3 staining in HDR-injected zebrafish. (A) *pikfyve* HDR-injected and uninjected zebrafish retinal cyrosections were stained with anti-LC3 antibody at 5 dpf and analyzed with confocal microscopy. The rightmost panel shows representative quantification done in ImageJ. The number (B) and size (C) of LC3-labelled puncta in the RPE was quantified in ImageJ. Uninjected siblings n=2 fish; HDR-injected n=2 fish; 2-3 measurements/section. *p<0.05.

5.3 Prime Editing

5.3.1 Golden gate assembly of pegRNA

Since I could not detect evidence of HDR in injected zebrafish and DSBs introduced random mutations in *pikfyve*, I attempted prime editing to introduce the patient mimic mutation into zebrafish without the use of DSBs. Prime editing was discussed in detail in section 1.6.3, and it is a newer technology that has only been reported successful once in zebrafish (Petri et al., 2021). It relies on reverse transcription to insert precise edits into the sequence of interest. I first used golden gate cloning to assemble the pegRNA components into a BB10 assembly vector (Fig. 5.4A). The vector was digested with BsaI restriction enzyme, and the plasmid backbone (Fig. 5.4B, yellow box) was purified and used in the assembly reaction demonstrated in Fig. 5.4C. The assembled plasmid was digested again with BsaI but the smaller fragment (Fig. 5.4B, red box) containing the pegRNA sequence was purified and Sanger sequenced. As shown in Fig. 5.4D, sequencing revealed correct assembly of pegRNA components and successful golden gate cloning.

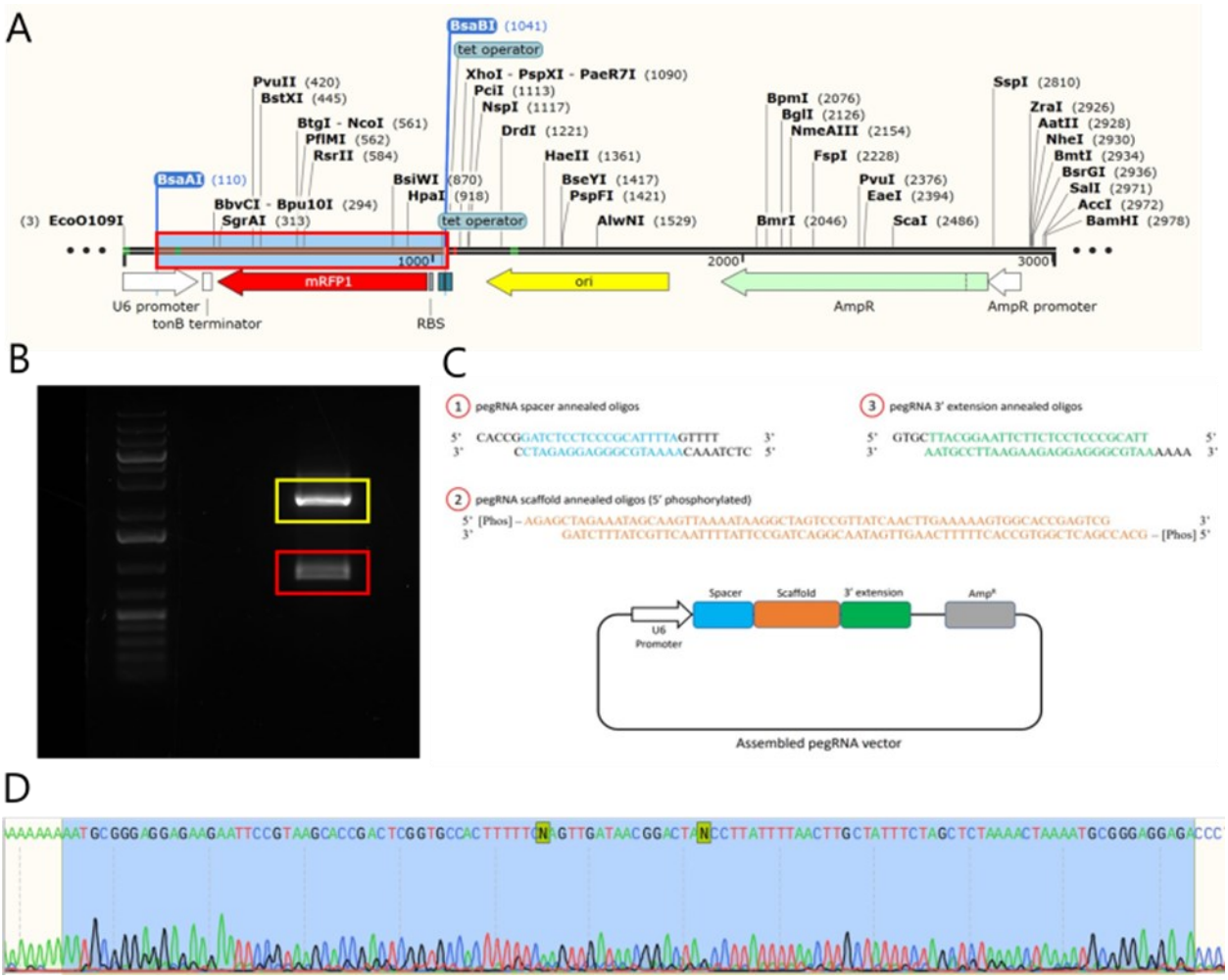

Figure 5.4 – pegRNA golden gate assembly. (A) BB10 assembly vector. The highlighted region shows the region cut by BsaI restriction enzyme which contains the red fluorescence protein (RFP) gene. (B) Gel electrophoresis of BB10 BsaI digestion. The yellow box indicates the plasmid backbone and red box highlights the RFP gene in the uncut plasmid and the pegRNA sequence in the assembled plasmid. (C) Schematic of pegRNA fragment sequences and assembly in the BB10 plasmid. (D) Sanger sequencing of assembled pegRNA sequence (highlighted region).

5.3.2 No evidence of prime editing in zebrafish

Upwards of twenty 2 dpf prime editor injected zebrafish were analyzed with PCR and Sanger sequencing. As shown in Fig. 5.5A, PCR fragments from both prime editor-injected and uninjected fish appeared at the expected size of 454 bp. To further analyze editing, I extracted DNA from individual prime editor injected zebrafish and analyzed the target DNA region by Sanger sequencing. Two rounds of prime editing injections were done and as shown in Fig. 5.5B, no evidence of editing was detected, and the adenine target base (highlighted in Fig. 5.5B) was unchanged between injected and uninjected fish. I hypothesized that the purity of the *in vitro* synthesized prime editor mRNA may have been low and therefore prime editing was unsuccessful. Therefore, I analyzed mRNA quality using gel electrophoresis (Fig. 5.5C) and found that no significant impurities were present as evident by the presence of only one band on the gel.

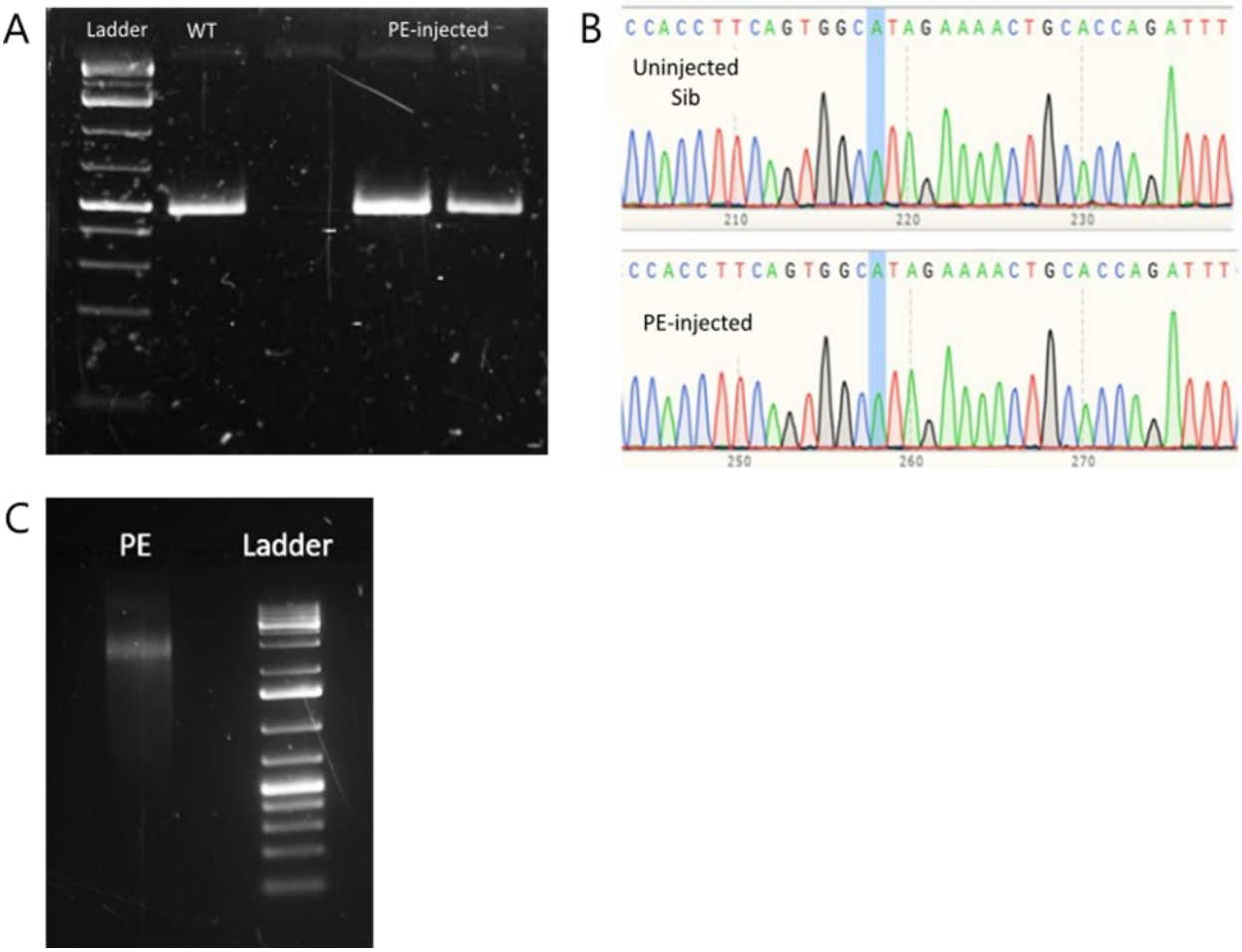

Figure 5.5 – Prime editing in zebrafish. (A) Gel electrophoresis from control (WT) and prime editor injected zebrafish. DNA was extracted from individual 2 dpf embryos and the region targeted by the pegRNA was amplified with PCR (B) Sanger sequencing from the region targeted by the prime editor. The target adenine is highlighted. (C) Gel electrophoresis of the prime editor mRNA compared to the 1 kb DNA ladder.

5.4 Adenine base editing

5.4.1 Inefficient adenine base editing in zebrafish

Since prime editing is a newer and less established technique in zebrafish, I changed my focus to adenine base editing (ABE) as a method to introduce the patient mimic mutation. ABE

was discussed in detail in section 1.6.2.2, and it utilizes an adenosine deaminase fused to a Cas9 nickase to introduce adenine to guanine (thymine to cytosine) mutations. The *PIKFYVE* patient carries an adenine to guanine point mutation and thus, ABE can be used to introduce a patient mimic mutation in fish. ABE mRNA was synthesized *in vitro* and microinjected into one-cell stage fish along with ABE crRNA. Two separate rounds of injections were performed with ~100 embryos injected per round. As shown in Fig. 5.6, DNA extracted from individual injected embryos (Fig. 5.6B) was identical to uninjected embryos (Fig. 5.6A) in the region targeted by the crRNA. The target adenine residue was unchanged in injected zebrafish (Fig. 5.6B). Moreover, the Sanger sequences showed no evidence of DNA cutting, indicating that gene editing was unsuccessful. I hypothesized that the purity of the synthesized mRNA may be low and thus, ABE did not occur. Therefore, I analyzed the ABE mRNA on a 2% SB gel. If the mRNA contains a high degree of impurities, I expected to observe multiple bands of various lengths in gel electrophoresis. However, as shown in Fig. 5.6C, I found that mRNA purity was relatively high with one main band appearing on the gel.

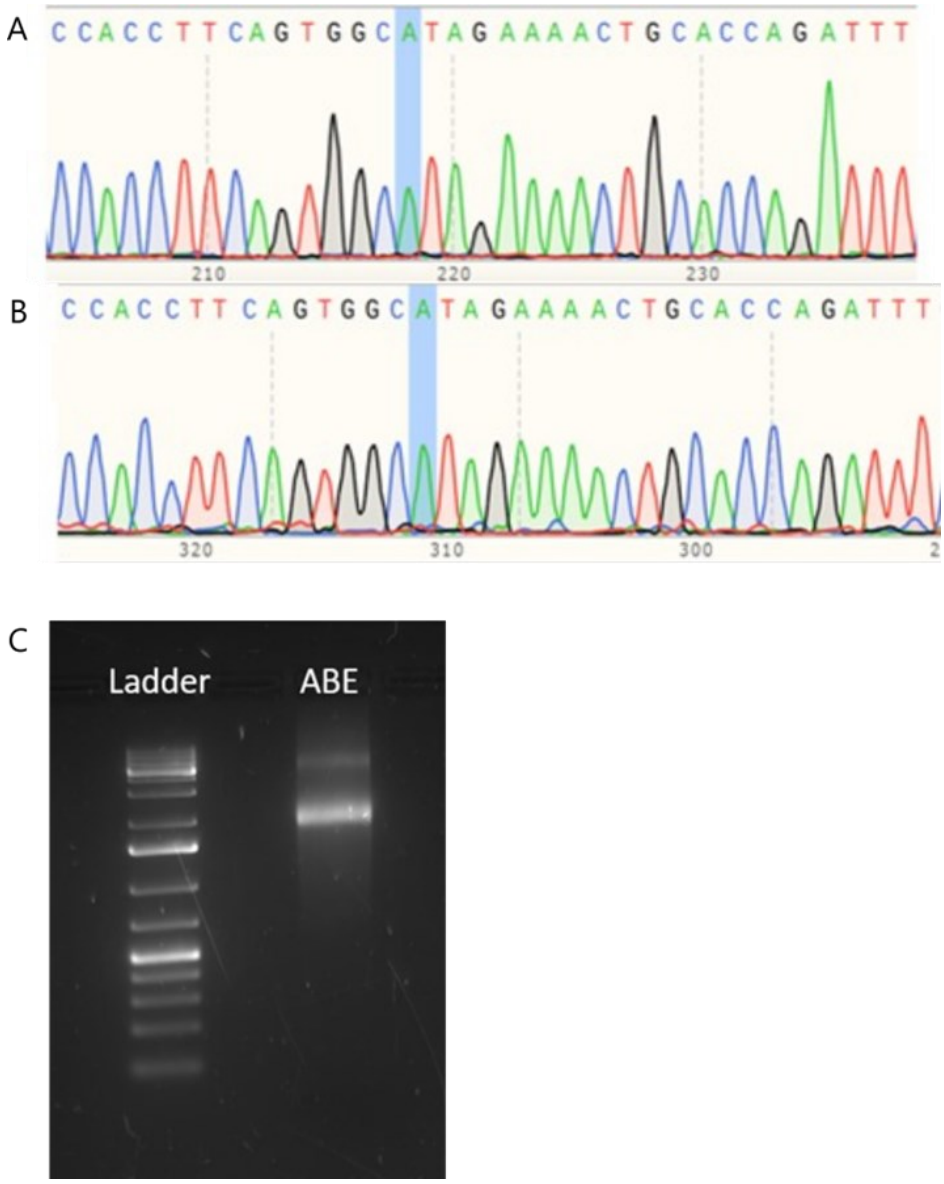

Figure 5.6 – Adenine base editing in zebrafish. (A) Sanger sequence from control uninjected and (B) adenine base editor injected zebrafish from the region targeted by the crRNA. The target adenine base is highlighted in both sequences. (C) adenine base editor mRNA was run on a 2% sodium borate gel to analyze purity.

5.5 Cytosine base editing

5.5.1 Validation of editing

Cytosine base editing (CBE) is an older technology that is well established in zebrafish. CBE was discussed in detail in section 1.6.2.1, and it relies on a cytosine deaminase fused to a Cas9 nickase to convert cytosine residues to thymine (and guanine to arginine). CBE cannot introduce the patient-mimic mutation into zebrafish since the patient mutation is an adenine to guanine substitution. Nevertheless, I attempted CBE as a proof of concept for base editing in fish. I sought to replicate work done by Rosello et al where they edited the two zebrafish pigment genes *tyr* and *slc45a2* (Rosello et al., 2021). Targeting pigment genes allows for easy detection of base edited fish as they appear less pigmented/ albino depending on editing efficiency.

I synthesized the CBE mRNA *in vitro* and then verified the sequence by reverse transcription. I designed two sets of primers - one to amplify part of the APOBEC1 sequence which encodes the cytosine deaminase, and one to amplify part of the nCas9 sequences which encodes the Cas9 nickase. Reverse transcription products were then run on an electrophoresis gel to analyze band size. If both sequences were correctly transcribed into mRNA, I expected to see a 288 bp band for APOBEC1 and a 946 bp band for nCas9. Indeed, as shown in Fig. 5.7A (panel 1), both bands were observed at the expected size, indicating successful mRNA *in vitro* transcription.

Next, I injected the CBE mRNA and the two pigment crRNAs into zebrafish embryos at the one-cell stage. I monitored pigmentation until 3 dpf as an indicator of successful base editing. At 3 dpf, pools of five embryos were euthanized and DNA was extracted for Sanger sequencing. As shown in Fig. 5.7B, the two guanine residues targeted by CBE in the *tyr* gene were

successfully edited in CBE-injected zebrafish. The first target guanine was completely changed to adenine while the second was ~50% guanine and 50% adenine. In contrast, I did not detect editing of the two guanine residues targeted in the *slc45a2* gene in the five embryos analyzed (Fig. 5.7C).

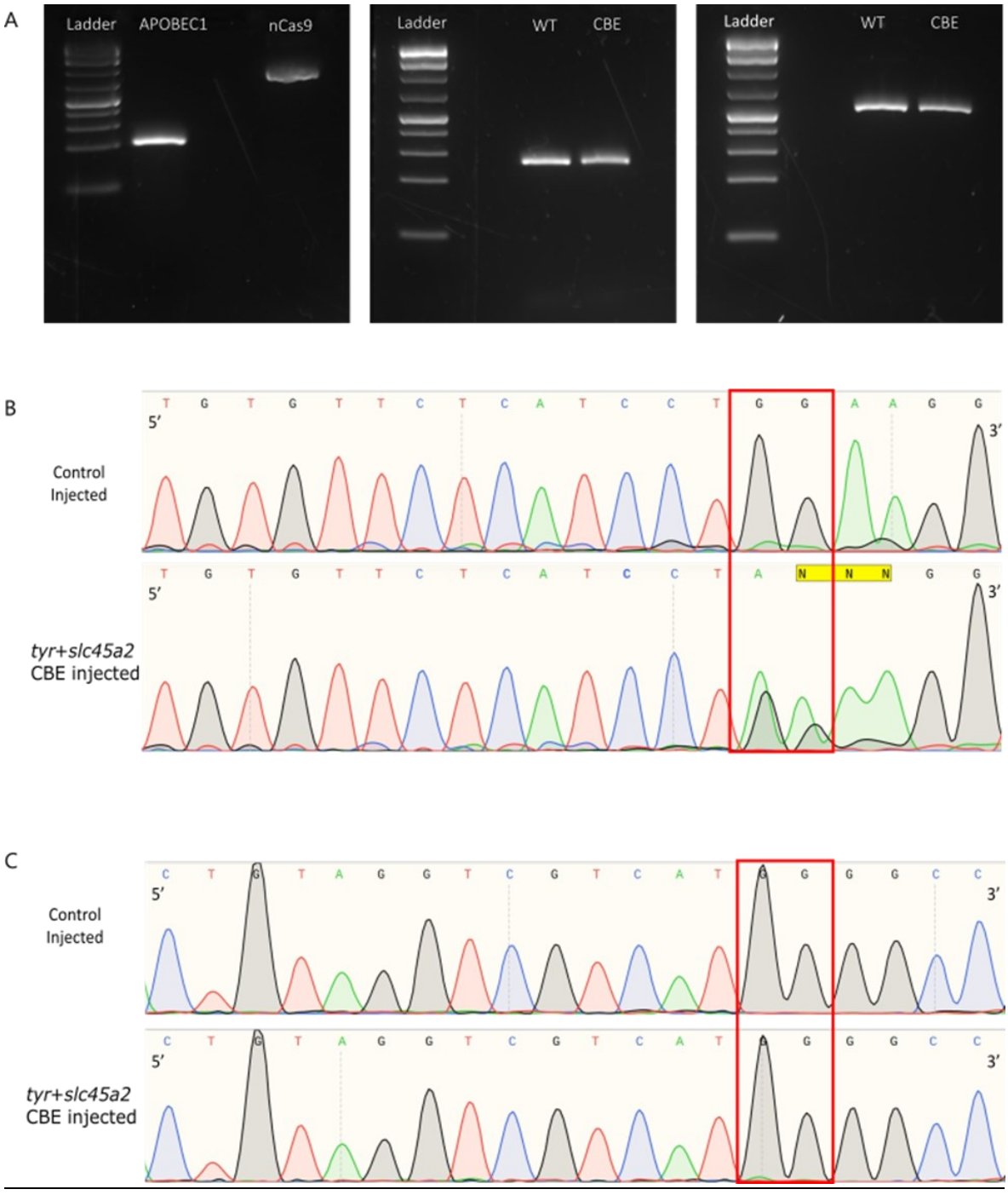

Figure 5.7 – Cytosine base editing in zebrafish. (A) Left: cytosine base editor mRNA was reverse transcribed and the part of the APOBEC1 and nCas9 sequence amplified and run on a 2% sodium borate gel. The region targeted by the *tyr* crRNA (middle gel) and the *slc45a2* crRNA (right gel) was PCR amplified and run on a 2% sodium borate gel. DNA Sanger sequencing from the region targeted in the (B) the *tyr* gene and (C) the *slc45a2* gene compared to control injected controls. The red boxes indicate the bases targeted by the cytosine base editor.

5.5.2 Pigment quantification

Along with sequencing, I monitored pigmentation in CBE-injected zebrafish as an indicator of successful base editing. I scored CBE-injected zebrafish into three categories: wildtype-like pigmentation, mild depigmentation, and severe depigmentation (Fig. 5.8A). I found that the number of mildly and severely depigmented embryos was higher in CBE-injected fish compared to control injected siblings (Fig. 5.8B). Of note, this analysis was done at 2 dpf in Rosello et al's study. However, I found that the injection process itself delayed pigment formation and therefore I performed analysis at 3 dpf to allow for pigment development in both control and CBE-injected fish. To quantify pigmentation, I performed fluorescence spectroscopy which measures the amount of melanin in a sample. Samples contained twenty 3 dpf uninjected, control injected, or CBE-injected fish. Moreover, groups were compared to a negative control which consisted of twenty PTU-treated zebrafish. PTU is frequently used in zebrafish to inhibit pigment formation and therefore I used it to inhibit pigmentation in the control group. I found that the difference in amount of melanin between CBE-injected and other control groups was not significantly different (Fig. 5.8C). Nonetheless, it is worth noting that the CBE-injected sample contained zebrafish with all degrees of pigmentation and not just mildly/severely depigmented ones. Further, even fish with successful CBE are mosaic and still produce a population of

pigmented cells. I am confident that the lack of significance is owing to the variability in the experimental group. Taken together, these findings suggest cytosine base editing is successful in zebrafish and that the particular crRNA likely impacts editing efficiency as observed by the differences in editing between *tyr* and *slc45a2* crRNAs.

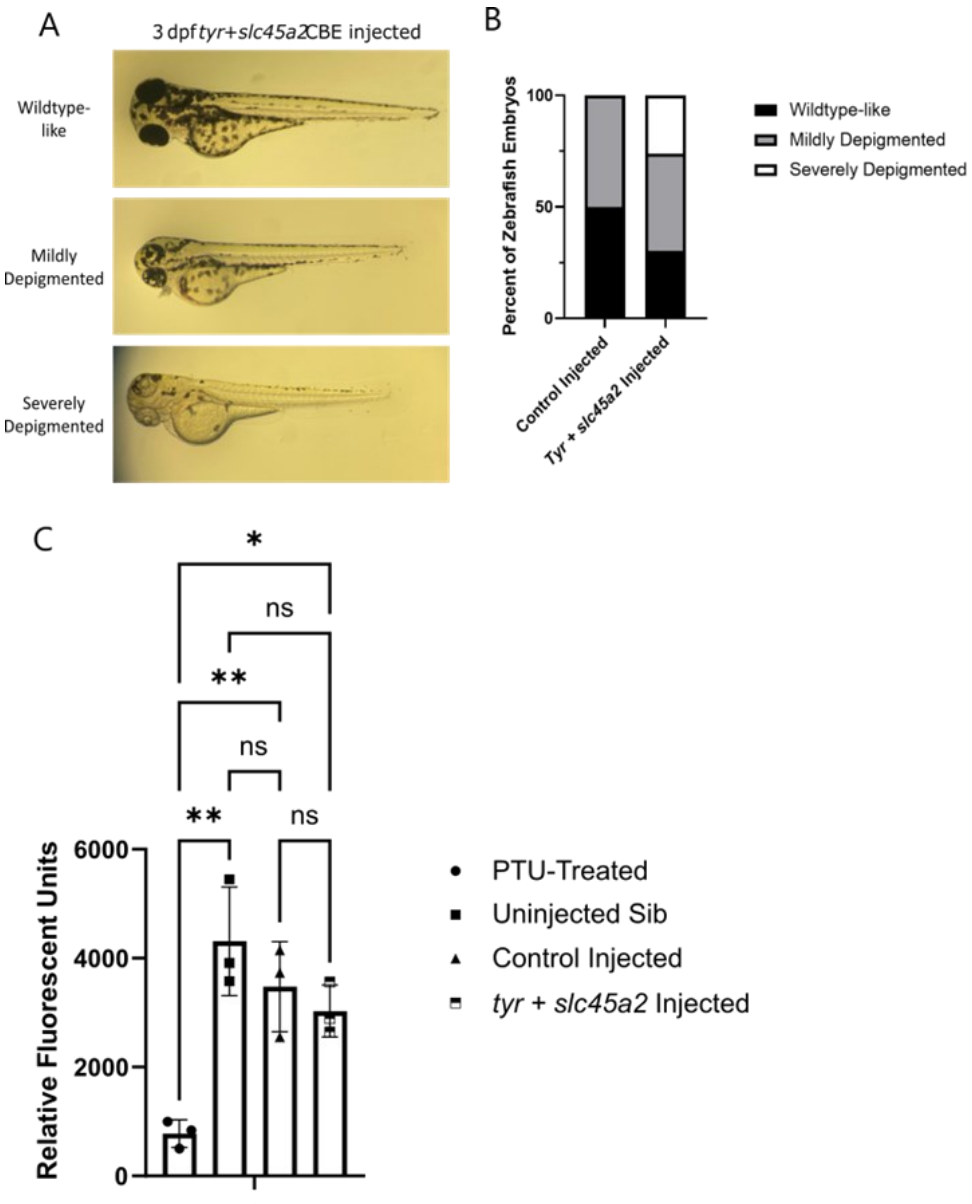

Figure 5.8 – Pigment quantification in cytosine base edited zebrafish. (A) 3 dpf control and cytosine base editor injected zebrafish were scored based on degree of pigmentation and (B)

categories were compared. (C) Fluorescence spectroscopy was performed to analyze the amount of melanin in CBE injected and control embryos. Each sample contained twenty zebrafish and a one-way ANOVA test and post-hoc Tukey test were performed. *$p<0.05$; **$p<0.01$.

CHAPTER SIX: DISCUSSION

6.1 Introduction

The goal of this work was to study the roles of Pikfyve in the zebrafish retina. Phosphoinositide biology is an active area of research, but little is known about PIKfyve and its products, $PI(3,5)P_2$ and PI5P, *in vivo*. In humans, mutations in *PIKFYVE* are ultra rare. The most common disorder associated with *PIKFYVE* mutations is Corneal Fleck Dystrophy, where white flecks appear within the stromal layer of the cornea in affected patients. Mei et al., identified one family with *PIKFYVE* mutations that developed congenital cataracts. Moreover, the Ian MacDonald lab identified a patient with a novel heterozygous missense mutation in *PIKFYVE* and a retinal dystrophy phenotype not previously reported. While the phenotypes associated with *PIKFYVE* mutations in humans are largely ocular, the roles of PIKFYVE in the eye remain unexplored which may be attributed to the difficulty of studying the gene *in vivo* due to the embryonic lethality of its knockout. I hypothesized that Pikfyve plays an important role in the zebrafish retina, and I sought to test my hypothesis through two aims. First, to characterize the general roles of Pikfyve in the zebrafish retina by studying the effect of CRISPR/Cas9 knockdown and pharmacological inhibition. Second, to utilize precise gene editing technologies in zebrafish to introduce the patient specific mutation and create a stable, mimic line that can not only be used to elucidate the mechanism of disease of the specific patient mutation, but also overcome the embryonic lethality of CRISPR/Cas9.

6.2 Precise genome editing

6.2.1 Overview

The amino acid mutated in the *PIKFYVE* patient is conserved between humans and zebrafish and therefore I sought to create a patient mimic mutant line through introducing the analogous patient mutation into the zebrafish genome. In humans, *PIKFYVE* is located on chromosome two and encodes a 2098 amino acid long protein. In zebrafish, *pikfyve* is located on chromosome nine and encodes a 2075 amino acid long protein. The patient mutation is in exon 37 in humans which is analogous to exon 38 in zebrafish, and both mutations fall within the kinase domain of the protein. The location of mutations within *PIKFYVE* seems to have a profound impact on the severity of the phenotype. *PIKFYVE* variants associated with Corneal Fleck Dystrophy all appear early in the protein, in the CCTγ, FYVE, and SPEC domains (Mei et al., 2021). On the other hand, variants in the kinase domain of PIKFYVE, namely the two reported by Dr. Ian MacDonald and by Mei et al., result in a much more severe phenotype. In 2021, Mei et al reported a novel heterozygous missense variant (p.G1943E) in *PIKFYVE* in a Chinese Korean family. 12 of 31 family members across four generations were affected with congenital cataracts. Five family members underwent whole exome sequencing (WES) – four members were affected with congenital cataracts, and one was not. WES revealed the p.(G1943E) variant in those with congenital cataracts but not in the healthy control family members. None of the affected patients presented with corneal flecks (Mei et al., 2021). The authors created a zebrafish mutant carrying an 8-bp deletion and a 112-bp insertion in exon 40 of *pikfyve* and found that mutants exhibited a cataract phenotype in addition to vacuolization of the lens (Mei et al., 2021). Overexpression of the p.(G1943E) variant did not produce a cataract phenotype and thus, the authors concluded that the variant was a loss of function and not a

dominant negative (Mei et al., 2021). Interestingly, the patient identified by Dr. Ian MacDonald carries a mutation in close proximity to the variant identified by Mei et al and yet exhibits a vastly different phenotype. No flecks were present on the patient's cornea and the patient's lenses were clear, indicating that the p.(His1831Arg) variant is associated with neither Corneal Fleck Dystrophy nor congenital cataracts.

Since the location of the mutation, even within the same domain, appears to have a profound effect on the phenotype observed, I sought to create a patient mimic mutant zebrafish line to recapitulate the patient phenotype and dissect the underlying disease mechanism. Zebrafish are particularly advantageous for this research as they are characterized by high fecundity and *ex vivo* fertilization, giving us early access to a large number of embryos for genetic manipulation. Moreover, zebrafish are excellent model organisms for studying ocular disease as they possess large eyes that are similar in retinal organization to humans. Furthermore, the zebrafish rod: cone ratio is high, allowing for analysis of both photoreceptor subtypes.

Zebrafish have been utilized in genetics research since the 1990s when they were exposed to the mutagen N-ethyl-N-nitrosourea (ENU) and phenotypes in offspring were linked to mutations through positional cloning (Rafferty & Quinn, 2018). Since then, advancements in gene editing technologies have allowed for reverse genetics in zebrafish, where instead of starting with an observable phenotype and subsequently identifying the mutation (forward genetics), genes can be targeted directly. The first technique to achieve reverse genetics in zebrafish was targeting induced local lesions in genomes or TILLING for short. Briefly, TILLING utilized a chemical mutagen to introduce genetic mutations, which are then identified with PCR. Another technique that significantly advanced zebrafish genetics was the *Tol2* transposon system, where exogenous DNA is randomly inserted into the genome through the

Tol2 transposase. Nevertheless, a targeted gene editing approach was still required, which led to the development of zinc-finger nucleases (ZFNs). Briefly, ZFNs can be engineered to target and cut specific three nucleotide sequences in the DNA. Cuts are then repaired by cellular machinery, which is imprecise, leading to the introduction of random mutations at a target region of interest. ZFNs have largely been replaced by the development of TALENs and the CRISPR/Cas9 system as their design is difficult and they show limited success. In contrast to ZFNs which are based on the zinc-finger nucleases, TALENs (short for transcription activator-like effector nucleases) are proteins containing TALE DNA-binding domains and the catalytic domain of the FokI nuclease. Thus, TALENs can easily be designed to target and cut specific sequences of DNA. On the other hand, CRISPR/Cas9 is an RNA-based gene editing technique that relies on a guide RNA to direct the Cas9 nuclease to the sequence of interest. Similar to ZFNs and TALENs, CRISRP/Cas9 relies on cellular DNA repair machinery, in particular NHEJ, to introduce random mutations at the cut site. The CRISPR/Cas9 system is both simple and highly efficient and has therefore become the major method in use.

6.2.2 Homology directed repair

CRISPR/Cas9 has been widely adopted and numerous developments have been made to advance it towards precise genome editing. One such development is the combination of the CRISPR/Cas9 system with homology directed repair (HDR). HDR was discussed in section 1.6.1, and it relies on an exogenous repair template that encodes the desired DNA change to introduce specific mutations into the genome. I used HDR in my first attempt to introduce the patient mimic mutation into zebrafish. The design of the exogenous DNA template and the microinjection protocol have a significant impact on the efficiency of precise gene editing. Therefore, I performed a literature review on HDR in zebrafish and utilized the IDT HDR design

tool to plan my experiment. Zebrafish mutagenesis occurs through microinjection of editing machinery into the one- or two-cell stage embryo. Microinjection into the cytoplasm of the cell produces a germline succession rate of 0 to 63.9% (Wierson et al., 2020) while microinjection into the yolk produces a rate of 12.5% to 37.5% (Burg et al., 2016 and Burg et al., 2018). Therefore, I performed microinjections into the cell to increase the probability of germline transmission. Another factor that impacts editing efficiency is the concentration of the components injected. Injection mixture concentrations vary considerably between studies; however, in general the Cas9 concentration used is at least four times the guide RNA and six times the template DNA concentration (Prill and Dawson, 2020). Therefore, I prepared injection mixtures following these guidelines. Cas9 endonuclease may be injected as protein or mRNA. The highest HDR success rates have been reported with Cas9 injected as mRNA (Prill and Dawson, 2020). However, comparison of HDR efficiency with Cas9 mRNA versus protein in zebrafish found higher repair efficiency with injections as protein (Zhang et al., 2018). Our lab has had high success rates with Cas9 protein for general mutations. Additionally, the protein is commercially available and therefore of reliable quality, and since I was aiming to create the HDR repair as early as possible during embryogenesis, I injected Cas9 as a protein in my HDR experiments. One of the key determinants of HDR success is the exogenous DNA template, which may be in the form of a plasmid, a single-stranded oligonucleotide (ssODN), or a double-stranded DNA (dsDNA) fragment. The highest HDR efficiencies have been reported with ssODN and therefore, I utilized a ssODN in my experiment (Prill and Dawson, 2020). The length and symmetry of the ssODN also impacts HDR efficiency. Literature is inconsistent regarding the optimal length for HDR repair with one study reporting a 10% decrease in editing efficiency when the length of the template is increased to 500 bp and a 59% decrease in efficiency when the

template is shorter than 18 bp (Bai et al., 2020 and Burg Et al., 2018). In general, a template longer than 400 bp or shorter than 18 bp results in inefficient repair (Prill and Dawson). The sequence on either end of the desired edit is referred to as the homology arm and the symmetry of the homology arms has mixed results on HDR efficiency (Prill and Dawson, 2020). My ssODN was asymmetrical and 198 bp long to ensure that the ends of the template lined up with intronic sequence, to prevent the introduction of mutations into exonic sequence at the site of integration. Finally, NHEJ is the prominent repair pathway in most cells. Therefore, to increase HDR efficiency, small molecule drugs that either inhibit NHEJ or enhance HDR are commonly used. I used NU7441, which is a potent inhibitor of DNA-dependent protein kinases that are recruited to the DSB during NHEJ, to direct the cells to using HDR as opposed to NHEJ to repair Cas9-induced DSBs (Yang et al., 2020). Injection of inhibitors was reported to produce an HDR efficiency of 53.7% while incubation with the drug in water increased efficiency to 74% in zebrafish (Zhang et al., 2018, Boel et al., 2018, Aksoy et al., 2019). I attempted both injection and incubation with NU7441 in my experiments. As shown in Fig. 5.1, I found that HDR-injected zebrafish sequencing was comparable to fish injected with just CRISPR/Cas9. Hence, DSBs were likely still repaired via NHEJ, which led to the introduction of random mutations. Of note, while I did not detect the desired single base substitution through RFLP analysis, this does not eliminate the possibility that some HDR occurred but with efficiency that was too low to be detected on a gel. In the future, DNA from HDR-injected zebrafish should be extracted and cloned into bacteria, then sequenced to increase the sensitivity of mutation detection. Moreover, attempting different length and symmetry templates, and utilizing other inhibitors in addition to NU7441 may increase HDR efficiency in future experiments. Finally, it would be worthwhile to

attempt HDR in a gene that has been previously successfully modified such as *tyr* as a proof of concept, and as an opportunity to optimize injection mixture components and concentrations.

6.2.3 Prime editing

While HDR repair may have occurred to some extent in my experiments, the nature of mutations in *pikfyve* limits the utility of HDR for this project. In other words, because *pikfyve* knockout is embryonic lethal, a high repair efficiency would be required to produce viable embryos that survive past 7 dpf. And even if I had complete HDR, the fish might not survive with two altered alleles of *pikfyve*. While I did observe a slightly lower mortality rate with HDR-injected fish compared to crispants, a significant proportion still died by 7 dpf and I could not detect the desired sequence changes with RFLP analysis in the survivors. Therefore, I decided to explore other precise gene editing technologies that do not involve the production of DSBs to overcome the embryonic lethality of gene knockout. Prime editing is a novel technology that was discussed in detail in section 1.6.3. It utilizes a catalytically impaired Cas9 endonuclease fused to a reverse transcriptase. Unlike HDR, prime editing does not rely on an exogenous DNA template, but rather the desired sequence change is encoded in the specialized guide RNA (pegRNA). Prime editing is a versatile technique that opens the door to introducing any kind of point mutation and small insertions and deletions into the genome. However, its use in animal models is relatively limited due to its novelty. In fact, only one study reporting successful prime editing in zebrafish has been published. While prime editing offers unmatched promise for disease modeling and gene therapy in the future, I encountered several drawbacks from my experience with the technology. First, the complexity of pegRNA design, which directly impacts editing efficiency, was a major hurdle. I attempted to incorporate recommendations from various protocols as discussed in section 2.5.1 to create a highly efficient pegRNA; however, in the

future testing various lengths and sequences would be advisable. Second, the assembly of the pegRNA components was another area for the potential introduction of errors; individual DNA fragments needed to be organized in the correct order with the correct sequence in the assembly vector. Third, the assembled vector was transcribed *in vitro* to synthesize the pegRNA, which is another potential step for the introduction of errors. I was unable to detect the desired sequence change in *pikfyve* with prime editing. There are a variety of factors that may be contributing to this, including the hurdles with design and pegRNA synthesis previously discussed. In addition, the prime editor was synthesized *in vitro* from a plasmid and injected as mRNA. I did not verify the sequence of the mRNA with reverse transcription and therefore cannot eliminate the possibility that either the RNA was not properly capped and tailed and was therefore degraded in the cell or that it was not correctly transcribed. In the future, the prime editor mRNA should be analyzed by reverse transcription to confirm its sequence. Of note, Petri et al., showed prime editing efficiency as high as 30% and germline transmission in zebrafish with the injection of the prime editor as a protein. Therefore, in the future it may be worthwhile to translate the prime editor mRNA and attempt microinjection as protein. To avoid room for errors in the pegRNA assembly and transcription process, pegRNAs could be directly ordered as synthesized RNA. However, this will be an expensive alternative, particularly if multiple pegRNAs are to be tested. Finally, I attempted PE2 here which, as discussed in section 1.6.3, only targets one of the two DNA strands. In the future, attempting PE3b which utilizes an additional gRNA to target the unedited strand, may increase editing efficiency.

6.2.4 Base Editing

I attempted two rounds of prime editing and detected no evidence of cutting or gene editing. We discussed our findings with the del Bene lab who have expertise in the development

of genetic tools in zebrafish and learnt that they also experienced very low success rates with prime editing. They recommended base editing as a more efficient alternative in zebrafish. Both prime and base editing could potentially introduce the patient mutation into the zebrafish genome without the introduction of DSBs. Base editing is a slightly older technology and is therefore better established in animal models. Moreover, the design process for base editors is significantly less complicated than prime editing as it only involves the base editor protein (or mRNA) and a gRNA, eliminating the errors associated with pegRNA assembly and transcription. The patient mutation is an adenine to guanine single base substitution and therefore I attempted adenine base editing (ABE) to mimic the patient point mutation.

Qin et al were first to report successful ABE of five genes in zebrafish with germline transmission (Qin et al., 2018). Qin et al first tested ABE7.10, which contains an engineered adenosine deaminase and has a reported editing efficiency of ~50% in human cells (Gaudelli et al., 2017). The region on which the deaminase acts is referred to as the base editing window and in ABE7.10, it falls within position -17 to -14 in the protospacer. Surprisingly, no base editing was detected with ABE7.10 so the authors synthesized a zebrafish codon-optimized version of the plasmid, termed zABE7.10. Editing efficiencies ranging from 7.14 to 22.20% were observed with this modified ABE. The authors noted that species has an impact on target position since the base editing window in zABE7.10 was at position -16 to -14 in the protospacer. In 2020, Richtar et al developed ABE8e, a new version carrying eight additional mutations in the adenosine deaminase to increase its editing efficiency. ABE8e was tested in zebrafish by Cornean et al where they showed successful ABE of the eye pigment gene *oca2* with a remarkable editing efficiency of 83.7 to 92.9% (Cornean et al., 2022). I therefore used ABE8e in my experiments to edit the *pikfyve* gene. According to Cornean et al the ABE8e editing window is on position -3 to

-11 of the protospacer. I utilized the ACEofBASEs design tool created by Cornean et al to design a crRNA that placed the adenine of interest at position 9, within the editing window. Of note, there was another adenine in the sequence at position 11 and thus editing it was a possibility. I performed two rounds of ABE, following recommendations from Cornean et al., 2020, Qin et al., 2018, and Zhang et al., 2017 with respect to injection mixture concentrations. However, I did not detect evidence of ABE in Sanger sequencing. There are several potential explanations for unsuccessful ABE, the main one being unsuccessful *in vitro* transcription of the ABE8e mRNA. In the future, the sequence of mRNA should be confirmed by reverse transcription. Moreover, the crRNA selected has a relatively low on-target score of 54 as predicted by the IDT CRISPR-Cas9 guide RNA design checker tool. Liang et al., recently established a zSpRY-ABE8e plasmid, which is not only codon optimized for zebrafish but also utilizes the near PAM-less Cas9 nickase, loosening the restriction on the PAM site (Liang et al., 2022). Future ABE experiments should utilize the zSpRY-ABE8e plasmid and other crRNAs with higher targeting scores to improve editing efficiency in zebrafish.

While experimenting with ABE, I also attempted to replicate work done by Rosello et al., where they used cytosine base editing (CBE) to introduce point mutations in the two pigment genes *tyr* and *slc45a2*. CBE is more well-established in zebrafish, and I sought to utilize it as a proof of concept for base editing rather than to introduce the *PIKFYVE* patient mutation. Rosello et al utilized the CBE4max-SpRY variant which contains a near PAM-less Cas9 nickase and a mutated cytosine deaminase to loosen PAM site restrictions and increase editing efficiency, respectively. This experimental design simplifies detection of editing as successful CBE will manifest as a decrease or lack of pigmentation in zebrafish. Therefore, I transcribed the CBE4max-SpRY plasmid *in vitro* to synthesize mRNA and co-injected it with the two pigment

crRNA/tracrRNA duplexes used by Rosello et al into one-cell zebrafish embryos. I detected successful CBE in the *tyr* gene but not the *slc45a2* gene in the samples analyzed. It is possible that the crRNAs targeting scores contribute to the difference observed in editing efficiency, but it is important to note that only one sample (containing genomic DNA from 5 embryos) was sequenced. Nevertheless, differences in pigmentation in injected embryos were observed by 3 dpf compared to control-injected zebrafish. Of note, depigmentation occurred in a mosaic fashion with some strongly pigmented cells still present but at lower numbers. Since I analyzed the F0 generation, it is expected that mosaic gene editing occurred and thus, variability in pigmentation between cells is presumed. While CBE cannot introduce the specific adenine to guanine patient mutation into the zebrafish genome, its success in editing the *tyr* gene shown here is a step in advancing precise gene editing in our lab. Finally, ABE should be revisited, and the same principles and concentrations used in CBE should be attempted in the future.

6.3 Characterization of roles for Pikfyve in the zebrafish eye

6.3.1 Pikfyve disruption approaches

I used apilimod to temporarily inhibit Pikfyve in zebrafish and study the effect on retinal electrical function and retinal integrity. Apilimod (also known as STA5326) is a small molecule drug that was initially tested as an inhibitor of interleukin (IL)-12 and IL-23 production (Ikonomov et al., 2019). It progressed in clinical trials for Crohn's disease and rheumatoid arthritis until phase II but was terminated due to ineffectiveness compared to placebo (Ikonomov et al., 2019). Since then, the molecular target of apilimod has been discovered as PIKfyve and the drug has regained attention as an anti-cancer therapeutic. The effects of pharmacological inhibition of PIKfyve on the eye have never been explored. Moreover, apilimod has not been previously tested in zebrafish. Therefore, I sought to characterize the effects of Pikfyve

inhibition on zebrafish, focusing on ocular phenotypes. Zebrafish are characterized by a high fecundity, producing on average 200-300 embryos from a single breeding. Moreover, they develop externally and are relatively low maintenance. Thus, zebrafish are excellent models for drug screens as drugs can be simply added and removed from embryonic media. Drug screening studies in zebrafish typically utilize concentrations ranging from 1 to 100 μM, with 10 μM being the most common concentration (Wiley et al., 2017). We initially tested apilimod at concentrations within the normal drug screening range and found 100% mortality rates within a day of exposure. Apilimod is a highly potent drug and concentrations used in the literature range from 3-5 μM in induced-pluripotent stem cell-derived motor neurons and astrocytes (Hung et al., 2023, Kang et al., 2020) to 15-1000 nM in macrophages and B-cells (Gayle et al., 2017, Kim et al., 2014). Ifrah Anjum from our lab developed an apilimod dose curve of 100, 250, and 500 nM and determined that at these concentrations, the drug was not immediately lethal but still resulted in formation of vacuoles in the tail with increasing doses. In line with these findings, I decreased apilimod concentrations in my experiments in this thesis to 500 nM – 1 μM, depending on the age of the fish.

I also utilized CRISPR/Cas9 mutagenesis to target the kinase domain of the Pikfyve protein and generate random mutations in exons 38 and 39. Our lab has previously shown high editing efficiency with CRISPR/Cas9, and therefore I aimed to utilize it to create *pikfyve* loss of function mutants. Consistent with previous research (Mei et al., 2021), I found that fish injected with CRISPR/Cas9 (*pikfyve* crispants) showed high mortality, with 71% of fish dying by 7 dpf in the group I quantified. This time point coincided with transfer of zebrafish larvae to the fish facility and therefore, I initially attributed death to failure to properly inflate the swim bladder. However, I observed that even when kept in a Petri dish, *pikfyve* crispants still died by 7 dpf. The

pikfyve gene is ubiquitously expressed and involved in cellular processes that are important throughout the body. Therefore, it is unlikely that mortality can be attributed to a single factor, but instead the accumulation of physiological defects likely results in death. I observed that *pikfyve* crispants were less active and showed a reduced response to physical stimuli compared to controls. PIKfyve is implicated in neuronal function (Huang et al., 2021, Zhang et al., 2008, Martin et al., 2013) and as evident by the increased cell death in brains of *pikfyve* crispants, it is likely that neuronal death underlies the reduced responsiveness and swimming behavior. Similar to *pikfyve* crispant zebrafish, mice lacking $PI(3,5)P_2$ due to knockout of one of the *PIKfyve*-complex proteins, *Fig4*, exhibit movement disorders (Ferguson et al., 2012) that were attributed to impaired myelination in the central and peripheral nervous systems (Chow et al., 2017, Winters et al., 2011). Additionally, work from Ifrah Anjum revealed poor muscles in the tails of treated larvae suggesting that a direct role on muscles may also be a contributing factor.

Due to the embryonic lethality of gene knockout, my analysis of *pikfyve* crispants was limited to the first few days of life. I recognize that the phenotypes observed in *pikfyve* crispants are more severe than those observed in the human patients and therefore, the ability to extend these findings to humans is limited. Nevertheless, my analysis of *pikfyve* crispants and apilimod-treated fish shed light on the importance of *pikfyve* in the retina, an area previously unexplored.

6.3.2 Effects of Pikfyve disruption on the zebrafish retina

I used a variety of techniques to analyze the retinas of *pikfyve* crispant and apilimod-treated zebrafish, including electroretinography, transmission electron microscopy, histology, and immunohistochemistry. I found that *pikfyve* crispants developed all retinal layers although some differences in layer thickness were observed. I hypothesized that the RPE would be most

affected by Pikfyve disruptions given its functions discussed in section 1.1.2.5, and therefore focused most of my analysis on the RPE layer. My work demonstrates that genetic and pharmacological disruptions of Pikfyve in zebrafish result in significant changes in the RPE. Firstly, I found a decrease in staining of the RPE marker ZPR2 in apilimod-treated zebrafish. Secondly, the RPEs of apilimod-treated and *pikfyve* crispant fish looked remarkably different from controls in brightfield images, with inconsistencies in layer thickness and increased tearing (Fig. 4.6). Thirdly, I detected RPE vacuolization and abnormal pigmentation in apilimod-treated and *pikfyve* crispant zebrafish.

The patient exhibits an ocular hypopigmentation phenotype in the iris and RPE. PIKfyve forms a complex with Vac14 and Fig4 and mutations in either of these proteins results in hypopigmentation in mice (Chow et al., 2007, Zhang et al., 2007, Jin et al., 2008). I did not observe a clear difference in whole larval pigmentation with light microscopy in *pikfyve* crispants compared to controls. Nevertheless, my TEM data provided valuable insight into alterations in RPE pigmentation as a result of *pikfyve* knockdown. Melanosomes are lysosome-related organelles that undergo a multistep maturation process to produce and store melanin. Melanin is produced through enzymatic activity of tyrosinase, which is delivered from the Golgi to the maturing melanosome by endosomes. Melanin is deposited onto PMEL fibrils to create opaque melanosomes and complete maturation. Two labs have studied the role of PIKfyve in melanosome maturation. Liggins et al found that melanocyte-specific knockout of *Pikfyve* resulted in greying of mice hair coats. The authors found that Pikfyve was required for trafficking of Tyr and TYRP1 from endosomes to stage II melanosomes and thus, loss of Pikfyve resulted in the accumulation of stage II melanosomes. In contrast, Bissig et al found that Pikfyve loss resulted in the accumulation of stage I melanosomes and attributed this to impaired PMEL

fibrillation due to compromised lysosomal protease delivery to stage I melanosomes in *PIKfyve* mutant mice. In my TEM, I found that the number of melanosomes was unchanged in *pikfyve* crispants, however, I observed a significant reduction in rod-shaped melanosomes similar to that observed in *Oa1*$^{-/-}$ mice (Rachel et al., 2012). Moreover, I detected melanosomes with abnormal melanin deposition. These findings suggest that melanosome maturation is impaired due to *pikfyve* knockdown as evident by the reduction in elongated melanosomes and the abnormal melanin deposition, potentially secondary to abnormal PMEL fibrillation. Nonetheless, I found that highly pigmented melanosomes still formed in *pikfyve* crispants. It is possible that Tyr, TYRP1, and lysosomal proteases are delivered to maturing melanosomes through an alternative pathway. Previous work in our lab by Ifrah Anjum revealed that apilimod decreases pigmentation of whole embryos at 2 dpf. Future work should analyze RPE pigmentation in *pikfyve* crispants at earlier time points (e.g., 2 dpf) to determine if melanosome maturation is delayed due to *pikfyve* knockdown.

I observed accumulation of photoreceptor OS discs in vesicles within the RPE of both *pikfyve* crispant and apilimod-treated zebrafish at 6 and 7 dpf. The RPE phagocytoses OS tips in a rhythmic fashion to prevent buildup of photo-oxidative damage in the non-regenerative photoreceptors (Moran et al., 2022). The timing of OS shedding and number of peaks per day varies between different species. In zebrafish, phagocytosis of OS peaks after light exposure and following dark onset, with phagosomes degraded within hours (Moran et al., 2022). It is important to note that while in my TEM experiments both control and crispant/treated fish were fixed at the same time, I did not take into consideration the time-of-day fish were fixed. In the future, the timing should be taken into consideration and fish fixed within hours of light onset or offset to better analyze phagosome maturation and degradation. Nevertheless, I observed that in

uninjected and DMSO controls, OS material was not present in the RPE, indicating efficient phagosome degradation. In contrast, knocking down or inhibiting Pikfyve resulted in the buildup of OS material in the RPE, indicative of impaired phagosome degradation.

To better understand the step at which phagosome maturation is impaired in *pikfyve* crispants and apilimod-treated fish, an overview of the process of OS phagocytosis and degradation by the RPE is helpful. The first step in the process involves the externalization of phosphatidylserine on the photoreceptor OS tips followed by recruitment of MFG-E8 and activation of the MerTK pathway, which results in binding of the OS tips to RPE cells (Moran et al., 2022). RPE apical processes then extend into adjacent photoreceptors and through actin reorganization, OS tips are engulfed within a phagocytic cup. These findings suggest that OS marking for degradation, binding, and engulfment are all intact in the absence of Pikfyve. Engulfed phagosomes migrate from the apical to the basal side of the RPE and become increasingly acidic (Moran et al., 2022). Phagosomes fuse with lysosomes to form phagolysosomes and OSs are degraded through enzymatic activity.

I detected the presence of OS material in both the apical and basal sides of the RPE, indicating that phagosome migration which is mediated by kinesin, myosin, and microtubules is intact. Nonetheless, the lingering presence of phagosomes containing obvious disc material indicates impaired degradation. I suspect that impaired phagosome-lysosome fusion and/or decrease phagolysosomal acidification underlie the impaired RPE degradative capacity. In a study done by Kim et al on macrophages, silencing of *PIKfyve* through either RNA or protein inhibition resulted in decreased LAMP1 staining on phagosomes, indicating defective phagosome-lysosome fusion. One potential mechanism through which this occurs is inactivation of TRPML1 due to decreased $PI(3,5)P_2$ production and therefore, decreased release of calcium,

which facilitates the phagosome-lysosome fusion process (Kim et al., 2014, Dayam et al., 2015). Another mechanism may involve impaired transport of proteins necessary for the fusion process due to defects in the endosomal system because of PIKfyve loss (Kim et al., 2014). Moreover, Kim et al showed that while phagosome acidification was intact in the absence of PIKfyve, proteolytic activity was impaired with a significant reduction in the protease Cathepsin D observed. While this may be due to failed fusion with lysosomes, the authors showed that lysosomes also exhibited reduced proteolytic activity. Hence, PIKfyve underlies the proteolytic activity of both phagosomes and lysosomes, likely through playing a role in trafficking and recycling of proteases from the Golgi to lysosomes (Kim et al., 2014). Interestingly, these findings contradict data from Michell et al where they demonstrated that genetic and pharmacological disruption of PIKfyve in amoeba reduced delivery of the proton-pumping vacuolar (V-ATPase), and therefore decreased phagosomal acidification. Of note, in the *pikfyve* zebrafish mutant created by Mei et al., ectopic expression of Trpml1 did not rescue the phenotype while treatment with bafilomycin A1 (a V-ATPase inhibitor) alleviated vacuolization in the lens. Thus, it is more likely that a mechanism involving V-ATPase is involved here.

Taken together, my findings demonstrate that like macrophages and amoeba, RPE cells require PIKfyve for proper degradation of phagosomes. To further elucidate the mechanisms through which PIKfyve mediates phagosome maturation in the RPE, LysoTracker Green staining may be utilized. LysoTracker Green stains for acidic organelles and thus, it can be used to determine if acidification of phagosomes occurs in the RPE. Additionally, treatment with bafilomycin A1 could be used to determine if V-ATPase inhibition rescues phagosome degradation in *pikfyve* crispant and apilimod-treated fish. Moreover, co-localization studies using

the lysosomal marker LAMP1 and the phagosomal marker Rab7 would provide further insight into the lysosome-phagosome fusion process.

I attempted to utilize immunohistochemistry in this study to label lysosomes with anti-LAMP1 antibody and LysoTracker Red and autophagosomes/phagosomes with anti-LC3 antibody. Unfortunately, my results were inconclusive due to a number of limitations. First, both antibodies significantly stained photoreceptor OSs, which made differentiating between labeled vacuoles in the apical RPE and photoreceptor OS difficult, especially when combined with sectioning artifacts. Second, RPE pigmentation hindered my ability to visualize staining in the RPE. I attempted to bleach sections prior to immunostaining to remove RPE pigmentation but unfortunately bleaching disrupted tissue integrity. Thirdly, as discussed in the results section, I consistently observed increased tearing in the RPEs of apilimod-treated and *pikfyve* crispant fish. It is likely that some vesicles in the RPE were lost during tearing and therefore not detected in my experiments. The use of pigmentless zebrafish in future experiments would improve the ability to visualize staining in the RPE without compromising tissue integrity with bleaching. Indeed, work done by Ifrah Anjum on Crystal fish, which carry mutations in four genes to inhibit pigment formation, revealed the presence of enlarged LC3-stained puncta in the RPE. In addition, experimenting with various antibody concentrations could reduce background staining of photoreceptor OSs although the use of transgenic zebrafish for LAMP1, Rab7, and/or LC3 would be a better alternative solution.

As mentioned, I found that the RPEs of *pikfyve* crispant and apilimod-treated fish were significantly more fragile and tore more often during sectioning. The RPE is exposed to high levels of photo-oxidation due to frequent bombardment with photons. Moreover, OS phagocytosis is an additional source of oxidative stress on the RPE (Datta et al., 2017) and

therefore, RPE cells must neutralize oxidative damage to retain their health. The RPE protects itself from oxidative damage through antioxidants like glutathione and through daily autophagy to remove damaged cellular components (Datta et al., 2017, Intartaglia et al., 2021). Oxidative damage to the RPE is a hallmark of age-related macular degeneration (AMD), and in mice, impaired autophagy creates an AMD-like phenotype (Yao et al., 2015). PIKfyve plays an important role in autophagy and its inhibition results in the accumulation of autophagosomes (Hasegawa et al., 2017). Therefore, I suspected that the RPE abnormalities observed in zebrafish with Pikfyve disruptions are to an extent attributable to impaired autophagy and the resultant buildup of oxidative damage in the RPE. Indeed, when I exposed zebrafish to apilimod and constant light, I observed an increase in RPE damage compared to DMSO-treated fish kept in the same constant light conditions. This demonstrates that Pikfyve is essential in the RPEs ability to mitigate oxidative stress, likely through degradation of damaged organelles by autophagy. Another factor contributing to the RPE abnormalities I observed, in particular the increased tearing, may be inflammation. Persistent inflammation is thought to be an underlying cause of AMD (Datta et al., 2017) and mice with oxidatively damaged lipids in the retina accumulate macrophages in the subretinal space (Cruz-Guilloty et al., 2013). Thus, it is possible that RPE inflammation secondary to increased oxidative damage caused by defective autophagy also plays a role in the increased RPE fragility during sectioning. One way this could be tested is through the analysis of the expression levels of immune-related genes in *pikfyve* crispant and apilimod-treated fish.

The mechanisms discussed above likely all contribute to RPE degeneration in *pikfyve* crispants and apilimod-treated zebrafish. Photoreceptor function and health is directly dependent on the RPE and degeneration of the RPE is correlated with photoreceptor degeneration, and vice

versa. I performed electroretinography on *pikfyve* crispants to assess cone electrical function and could not record significant responses to light. Apilimod-treated fish showed some cone responses to light although waveforms were significantly diminished and delayed. The difference between results from the two experimental approaches can be attributed to the duration of Pikfyve loss. In crispants, *pikfyve* is knocked down since birth while in apilimod-treated fish, Pikfyve is inhibited only from 4-6 dpf. Hence, it is expected for apilimod-treated fish to retain some visual function as Pikfyve was present during early stages of development. While I did not study the effect of Pikfyve loss on photoreceptor cells themselves, except for the measurements of OS length, it is an important area to explore in the future. Rajala et al showed that *PIKfyve* is highly expressed in mouse rods. Moreover, knockout of the autophagy gene *Atg5* in mice rod photoreceptors resulted in their degeneration (Yao et al., 2016). Therefore, it is possible that *PIKfyve* plays a role in maintaining the health of photoreceptors, potentially through autophagy, and therefore its loss directly impairs photoreceptor electrical function.

Finally, I detected significant TUNEL labeling in the eyes and brains of apilimod-treated and *pikfyve* crispant fish, indicative of increased apoptosis as a result of Pikfyve disruptions. Apilimod inhibition has shown a selective anti-proliferative effect against most non-Hodgkin B-cell lymphoma cell types tested (Ikonomov et al., 2019). The exact mechanism through which apilimod causes death of cancer cells is not fully understood. One hypothesized mechanism is that pre-existing abnormalities in cancer cells support excessive vacuolization which eventually leads to cell death through methuosis, a nonapoptotic cell death triggered by extreme vacuolization (Overmeyer et al., 2011). Interestingly, cell death was identified here by a TUNEL assay, which labels apoptotic cells. This suggests that cell death in the brain and eye due to Pikfyve inhibition in fish may not be occurring through methuosis as with cancer cells but rather

by apoptosis. I detected apoptosis primarily in the ciliary marginal zone of the retina and the brain, both of which are proliferative tissues. Therefore, my findings agree with previous work showing that apilimod increases cell death in proliferative cells.

In conclusion, the purpose of this work was to study the previously unexplored roles of PIKfyve in the retina *in vivo* and to establish precise gene editing technologies in zebrafish. I utilized two approaches, pharmacological inhibition and CRISPR/Cas9 mutagenesis, to assess the roles of *pikfyve* in the zebrafish retina. The mechanism underlying retinal dystrophy in the *PIKfyve* patient is not understood. I hypothesized that given the roles of PIKFYVE in phagocytosis, autophagy, melanogenesis, and lysosomal homeostasis and the importance of these processes in the RPE, pathology is primarily mediated by abnormalities in RPE function. I found that both approaches resulted in similar phenotypes of impaired retinal electrical function, increased cell death, RPE degeneration, and impaired RPE degradative capacity. I attempted HDR, prime editing, and base editing to introduce the analogous patient mutation into the zebrafish *pikfyve* gene. I found that while HDR and prime editing efficiencies were low, cytosine base editing is promising in zebrafish. Future work should focus on optimizing adenine base editing in zebrafish to create a patient mimic mutant line that can then be characterized to understand the disease mechanism of the specific patient variant. Comparison of the p.(His1831Arg) variant to other variants reported in *PIKFYVE* would provide valuable insight into genotype-phenotype correlations.

REFERENCES

Aksoy, Y. A., Nguyen, D. T., Chow, S., Chung, R. S., Guillemin, G. J., Cole, N. J., & Hesselson,D. (2019). Chemical reprogramming enhances homology-directed genome editing in zebrafish embryos. *Communications Biology*, *2*(1). https://doi.org/10.1038/s42003-019-0444-0

Anzalone, A. V., Koblan, L. W., & Liu, D. R. (2020). Genome editing with CRISPR–Cas nucleases, base editors, transposases and prime editors. *Nature Biotechnology*, *38*(7), 824–844. https://doi.org/10.1038/s41587-020-0561-9

Anzalone, A. V., Randolph, P. B., Davis, J. R., Sousa, A. A., Koblan, L. W., Levy, J. M., Chen, P. J., Wilson, C., Newby, G. A., Raguram, A., & Liu, D. R. (2019). Search-and-replace genome editing without double-strand breaks or donor DNA. *Nature*, *576*(7785), 149–157. https://doi.org/10.1038/s41586-019-1711-4

Augustin, S., Lam, M., Lavalette, S., Verschueren, A., Blond, F., Forster, V., Przegralek, L., He, Z., Lewandowski, D., Bemelmans, A.-P., Picaud, S., Sahel, J.-A., Mathis, T., Paques, M., Thuret, G., Guillonneau, X., Delarasse, C., & Sennlaub, F. (2023). Melanophages give rise to hyperreflective foci in AMD, a disease-progression marker. *Journal of Neuroinflammation*, *20*(1). https://doi.org/10.1186/s12974-023-02699-9

Banerjee, S., & Kane, P. M. (2020). Regulation of V-atpase activity and organelle ph by phosphatidylinositol phosphate lipids. *Frontiers in Cell and Developmental Biology*, *8*. https://doi.org/10.3389/fcell.2020.00510

Baranov, M. V., Bianchi, F., & van den Bogaart, G. (2020). The PIKfyve inhibitor Apilimod: A double-edged sword against covid-19. *Cells*, *10*(1), 30. https://doi.org/10.3390/cells10010030

Bilotta J, Saszik S, Sutherland SE. Rod contributions to the electroretinogram of the dark-adapted developing zebrafish. Dev Dyn. 2001 Dec;222(4):564-70. doi: 10.1002/dvdy.1188. PMID: 11748826.

Bissig, C., Croisé, P., Heiligenstein, X., Hurbain, I., Lenk, G. M., Kaufman, E., Sannerud, R., Annaert, W., Meisler, M. H., Weisman, L. S., Raposo, G., & van Niel, G. (2019). PIKfyve complex regulates early melanosome homeostasis required for physiological amyloid formation. *Journal of Cell Science*. https://doi.org/10.1242/jcs.229500

Bissig, C., Hurbain, I., Raposo, G., & van Niel, G. (2017). PIKfyve activity regulates reformation of terminal storage lysosomes from endolysosomes. *Traffic*, *18*(11), 747–757. https://doi.org/10.1111/tra.12525

Bissig C, Rochin L, van Niel G. PMEL Amyloid Fibril Formation: The Bright Steps of Pigmentation. Int J Mol Sci. 2016; 17(9). Epub 2016/09/03. https://doi.org/10.3390/ijms17091438 PMID: 27589732; PubMed Central PMCID: PMCPMC503771

Boel, A., Steyaert, W., De Saffel, H., Willaert, A., Coucke, P. J., De Paepe, A., et al. (2018). CRISPR/Cas9-mediated homology-directed repair by ssODNs in zebrafish induces complex mutational patterns resulting from genomic integration of repair-template fragments. Dis. Model. Mech. 11:dmm035352. doi: 10.1242/dmm.03535

Brockerhoff, S. E. (2011). Phosphoinositides and photoreceptors. *Molecular Neurobiology*, *44*(3), 420–425. https://doi.org/10.1007/s12035-011-8208-y

Buckley, C. M., Heath, V. L., Guého, A., Bosmani, C., Knobloch, P., Sikakana, P., Personnic, N., Dove, S. K., Michell, R. H., Meier, R., Hilbi, H., Soldati, T., Insall, R. H., & King, J. S. (2018). *PIKfyve/Fab1 Is Required for Efficient V-Atpase and Hydrolase Delivery to Phagosomes, Phagosomal Killing, and Restriction of*Legionella*Infection*. https://doi.org/10.1101/343301

Carrington, B., Weinstein, R. N., & Sood, R. (2020). BE4max and AncBE4max are efficient in germline conversion of C:G to T:a base pairs in zebrafish. *Cells*, *9*(7), 1690. https://doi.org/10.3390/cells9071690

Casey MA, Lusk S, Kwan KM. Eye Morphogenesis in Vertebrates. Annu Rev Vis Sci. 2023 Apr 11. doi: 10.1146/annurev-vision-100720-111125. Epub ahead of print. PMID: 37040791.

Caso, F., & Davies, B. (2021). Base editing and prime editing in Laboratory Animals. *Laboratory Animals*, *56*(1), 35–49. https://doi.org/10.1177/0023677221993895

Chapot, C. A., Euler, T., & Schubert, T. (2017). How do horizontal cells 'talk' to cone photoreceptors? different levels of complexity at the cone-horizontal cell synapse. *The Journal of Physiology*, *595*(16), 5495–5506. https://doi.org/10.1113/jp274177

Cheng, X.-T., Xie, Y.-X., Zhou, B., Huang, N., Farfel-Becker, T., & Sheng, Z.-H. (2018). Characterization of lamp1-labeled nondegradative lysosomal and endocytic compartments

in neurons. *Journal of Cell Biology*, *217*(9), 3127–3139. https://doi.org/10.1083/jcb.201711083

Cornean, A., Gierten, J., Welz, B., Mateo, J. L., Thumberger, T., & Wittbrodt, J. (2022). Precise in vivo functional analysis of DNA variants with base editing using aceofbases target prediction. *eLife*, *11*. https://doi.org/10.7554/elife.72124

Crespo, C., & Knust, E. (2018). Characterisation of maturation of photoreceptor cell subtypes during zebrafish retinal development. *Biology Open*. https://doi.org/10.1242/bio.036632

Datta, S., Cano, M., Ebrahimi, K., Wang, L., & Handa, J. T. (2017a). The impact of oxidative stress and inflammation on RPE degeneration in non-neovascular AMD. *Progress in Retinal and Eye Research*, *60*, 201–218. https://doi.org/10.1016/j.preteyeres.2017.03.002

Datta, S., Cano, M., Ebrahimi, K., Wang, L., & Handa, J. T. (2017b). The impact of oxidative stress and inflammation on RPE degeneration in non-neovascular AMD. *Progress in Retinal and Eye Research*, *60*, 201–218. https://doi.org/10.1016/j.preteyeres.2017.03.002

Dayam, R. M., Saric, A., Shilliday, R. E., & Botelho, R. J. (2015). The phosphoinositide-gated lysosomal ca2+channel, TRPML1, is required for phagosome maturation. *Traffic*, *16*(9), 1010–1026. https://doi.org/10.1111/tra.12303

de Lartigue, J., Polson, H., Feldman, M., Shokat, K., Tooze, S. A., Urbé, S., & Clague, M. J. (2009). PIKfyve regulation of endosome-linked pathways. *Traffic*, *10*(7), 883–893. https://doi.org/10.1111/j.1600-0854.2009.00915.x

Falkenburger, B. H., Jensen, J. B., Dickson, E. J., Suh, B.-C., & Hille, B. (2010). Symposium review: Phosphoinositides: Lipid regulators of membrane proteins. *The Journal of Physiology*, *588*(17), 3179–3185. https://doi.org/10.1113/jphysiol.2010.192153

Fernandes B, Matamá T, Guimarães D, Gomes A, Cavaco-Paulo A. Fluorescent quantification of melanin. Pigment Cell Melanoma Res. 2016 Nov;29(6):707-712. doi: 10.1111/pcmr.12535. Epub 2016 Oct 22. PMID: 27770559.

Fischer AJ, Bosse JL, El-Hodiri HM. The ciliary marginal zone (CMZ) in development and regeneration of the vertebrate eye. Exp Eye Res. 2013 Nov;116:199-204. doi: 10.1016/j.exer.2013.08.018. Epub 2013 Sep 8. PMID: 24025744.

Follo, C., Ozzano, M., Mugoni, V., Castino, R., Santoro, M., & Isidoro, C. (2011). Knock-down of cathepsin D affects the retinal pigment epithelium, impairs swim-bladder ontogenesis and causes premature death in zebrafish. *PLoS ONE*, *6*(7). https://doi.org/10.1371/journal.pone.0021908

Gaudelli, N. M., Komor, A. C., Rees, H. A., Packer, M. S., Badran, A. H., Bryson, D. I., & Liu, D. R. (2017). Programmable base editing of a•t to G•C in genomic DNA without DNA cleavage. *Nature*, *551*(7681), 464–471. https://doi.org/10.1038/nature24644

Gayle, S., Landrette, S., Beeharry, N., Conrad, C., Hernandez, M., Beckett, P., Ferguson, S. M., Mandelkern, T., Zheng, M., Xu, T., Rothberg, J., & Lichenstein, H. (2017). Identification of apilimod as a first-in-class pikfyve kinase inhibitor for treatment of B-cell non-Hodgkin Lymphoma. *Blood*, *129*(13), 1768–1778. https://doi.org/10.1182/blood-2016-09-736892

Gee JA, Frausto RF, Chung DW, Tangmonkongvoragul C, Le DJ, Wang C, Han J, Aldave AJ. Identification of novel PIKFYVE gene mutations associated with Fleck corneal dystrophy. Mol Vis. 2015 Sep 17;21:1093-100. PMID: 26396486; PMCID: PMC4575904.

George, A. A., Hayden, S., Stanton, G. R., & Brockerhoff, S. E. (2016). ARF6 and the 5'phosphatase of synaptojanin 1 regulate autophagy in cone photoreceptors. *BioEssays*, *38*. https://doi.org/10.1002/bies.201670913

Giridharan, S. S., Luo, G., Rivero-Rios, P., Steinfeld, N., Tronchere, H., Singla, A., Burstein, E., Billadeau, D. D., Sutton, M. A., & Weisman, L. S. (2022). Lipid kinases VPS34 and PIKfyve coordinate a phosphoinositide cascade to regulate retriever-mediated recycling on endosomes. *eLife*, *11*. https://doi.org/10.7554/elife.69709

Güngör Kobat, S. (2020). Importance of müller cells. *Beyoglu Eye Journal*. https://doi.org/10.14744/bej.2020.28290

Hanovice, N. J., Leach, L. L., Slater, K., Gabriel, A. E., Romanovicz, D., Shao, E., Collery, R., Burton, E. A., Lathrop, K., Link, B. A., & Gross, J. M. (2018). *Regeneration of the Zebrafish Retinal Pigment Epithelium after Widespread Genetic Ablation*. https://doi.org/10.1101/372151

Hasegawa, J., Strunk, B. S., & Weisman, L. S. (2017). PI5P and pi(3,5)p2: Minor, but essential phosphoinositides. *Cell Structure and Function*, *42*(1), 49–60. https://doi.org/10.1247/csf.17003

Hazeki, K., Nigorikawa, K., Takaba, Y., Segawa, T., Nukuda, A., Masuda, A., Ishikawa, Y., Kubota, K., Takasuga, S., & Hazeki, O. (2012). Essential roles of PIKfyve and PTEN on phagosomal phosphatidylinositol 3-phosphate dynamics. *FEBS Letters*, *586*(22), 4010–4015. https://doi.org/10.1016/j.febslet.2012.09.043

He, C., & Klionsky, D. J. (2010). Analyzing autophagy in zebrafish. *Autophagy*, *6*(5), 642–644. https://doi.org/10.4161/auto.6.5.12092

Hou, J., Xi, Z., Niu, J., Li, W., Wang, X., Liang, C., Sun, H., Fang, D., & Xie, S. (2018). Inhibition of pikfyve using YM201636 suppresses the growth of liver cancer via the induction of autophagy. *Oncology Reports*. https://doi.org/10.3892/or.2018.6928

Hsu, J. Y., Anzalone, A. V., Grünewald, J., Lam, K. C., Shen, M. W., Liu, D. R., Joung, J. K., & Pinello, L. (2020). *Primedesign Software for Rapid and Simplified Design of Prime Editing Guide RNAS*. https://doi.org/10.1101/2020.05.04.077750

Huang, P.-T., Einav, S., & Asquith, C. R. (2021). PIKfyve: A lipid kinase target for COVID-19, cancer and Neurodegenerative Disorders. *Nature Reviews Drug Discovery*, *20*(10), 730–730. https://doi.org/10.1038/d41573-021-00158-9

Hung, S.-T., Linares, G. R., Chang, W.-H., Eoh, Y., Krishnan, G., Mendonca, S., Hong, S., Shi, Y., Santana, M., Kueth, C., Macklin-Isquierdo, S., Perry, S., Duhaime, S., Maios, C., Chang, J., Perez, J., Couto, A., Lai, J., Li, Y., … Ichida, J. K. (2023a). PIKFYVE inhibition mitigates disease in models of diverse forms of Als. *Cell*, *186*(4). https://doi.org/10.1016/j.cell.2023.01.005

Hurley, J. B. (2021). Retina metabolism and metabolism in the pigmented epithelium: A busy intersection. *Annual Review of Vision Science*, *7*(1), 665–692. https://doi.org/10.1146/annurev-vision-100419-115156

Hwang, G.-H., Park, J., Lim, K., Kim, S., Yu, J., Yu, E., Kim, S.-T., Eils, R., Kim, J.-S., & Bae, S. (2018). Web-based design and analysis tools for CRISPR base editing. *BMC Bioinformatics*, *19*(1). https://doi.org/10.1186/s12859-018-2585-4

Ikonomov, O. C., Sbrissa, D., & Shisheva, A. (2019). Small molecule pikfyve inhibitors as cancer therapeutics: Translational promises and limitations. *Toxicology and Applied Pharmacology*, *383*, 114771. https://doi.org/10.1016/j.taap.2019.114771

Ikonomov, O. C., Sbrissa, D., Delvecchio, K., Xie, Y., Jin, J.-P., Rappolee, D., & Shisheva, A. (2011a). The phosphoinositide kinase PIKfyve is vital in early embryonic development. *Journal of Biological Chemistry*, *286*(15), 13404–13413. https://doi.org/10.1074/jbc.m111.222364

Intartaglia, D., Giamundo, G., & Conte, I. (2021). Autophagy in the retinal pigment epithelium: A new vision and future challenges. *The FEBS Journal*, *289*(22), 7199–7212. https://doi.org/10.1111/febs.16018

Jang, H., Jo, D. H., Cho, C. S., Shin, J. H., Seo, J. H., Yu, G., Gopalappa, R., Kim, D., Cho, S.-R., Kim, J. H., & Kim, H. H. (2021). Application of prime editing to the correction of mutations and phenotypes in adult mice with liver and eye diseases. *Nature Biomedical Engineering*, *6*(2), 181–194. https://doi.org/10.1038/s41551-021-00788-9

Jiang, T., Henderson, J. M., Coote, K., Cheng, Y., Valley, H. C., Zhang, X.-O., Wang, Q., Rhym, L. H., Cao, Y., Newby, G. A., Bihler, H., Mense, M., Weng, Z., Anderson, D. G., McCaffrey, A. P., Liu, D. R., & Xue, W. (2020). Chemical modifications of adenine base editor mrna and guide RNA expand its Application Scope. *Nature Communications*, *11*(1). https://doi.org/10.1038/s41467-020-15892-8

Jiang, Y.-Y., Chai, Y.-P., Lu, M.-H., Han, X.-L., Lin, Q., Zhang, Y., Zhang, Q., Zhou, Y., Wang, X.-C., Gao, C., & Chen, Q.-J. (2020). *Prime Editing Efficiently Generates W542L and S621I Double Mutations in Two ALS Genes in Maize*. https://doi.org/10.1101/2020.07.06.188896

Jo, D. H., Jang, H.-K., Cho, C. S., Han, J. H., Ryu, G., Jung, Y., Bae, S., & Kim, J. H. (2021). *Therapeutic Adenine Base Editing Corrects Nonsense Mutation and Improves Visual Function in a Mouse Model of Leber Congenital Amaurosis*. https://doi.org/10.1101/2021.01.07.425822

Kang, Y.-L., Chou, Y.-Y., Rothlauf, P. W., Liu, Z., Soh, T. K., Cureton, D., Case, J. B., Chen, R. E., Diamond, M. S., Whelan, S. P., & Kirchhausen, T. (2020). *Inhibition of Pikfyve Kinase Prevents Infection by Zaire Ebolavirus and SARS-COV-2*. https://doi.org/10.1101/2020.04.21.053058

Kim, G. H. E., Dayam, R. M., Prashar, A., Terebiznik, M., & Botelho, R. J. (2014). PIKfyve inhibition interferes with phagosome and endosome maturation in macrophages. *Traffic*, *15*(10), 1143–1163. https://doi.org/10.1111/tra.12199

Komor, A. C., Kim, Y. B., Packer, M. S., Zuris, J. A., & Liu, D. R. (2016). Programmable editing of a target base in genomic DNA without double-stranded DNA cleavage. *Nature*, *533*(7603), 420–424. https://doi.org/10.1038/nature17946

Koukourakis MI, Kalamida D, Giatromanolaki A, Zois CE, Sivridis E, Pouliliou S, Mitrakas A, Gatter KC, Harris AL. Autophagosome Proteins LC3A, LC3B and LC3C Have Distinct Subcellular Distribution Kinetics and Expression in Cancer Cell Lines. PLoS One. 2015 Sep 17;10(9):e0137675. doi: 10.1371/journal.pone.0137675. PMID: 26378792; PMCID: PMC4574774.

Kramer, R. H., & Davenport, C. M. (2015). Lateral inhibition in the vertebrate retina: The case of the missing neurotransmitter. *PLOS Biology*, *13*(12). https://doi.org/10.1371/journal.pbio.1002322

Kweon, J., Yoon, J.-K., Jang, A.-H., Shin, H. R., See, J.-E., Jang, G., Kim, J.-I., & Kim, Y. (2020). *Engineered Prime Editors with Pam Flexibility*. https://doi.org/10.1101/2020.11.10.377580

Kwon, W., & Freeman, S. A. (2020). Phagocytosis by the retinal pigment epithelium: Recognition, resolution, Recycling. *Frontiers in Immunology*, *11*. https://doi.org/10.3389/fimmu.2020.604205

Lakkaraju, A., Umapathy, A., Tan, L. X., Daniele, L., Philp, N. J., Boesze-Battaglia, K., & Williams, D. S. (2020). The cell biology of the retinal pigment epithelium. *Progress in Retinal and Eye Research*, *78*, 100846. https://doi.org/10.1016/j.preteyeres.2020.100846

Lees, J. A., Li, P., Kumar, N., Weisman, L. S., & Reinisch, K. M. (2020a). Insights into lysosomal pi(3,5)P2 homeostasis from a structural-biochemical analysis of the PIKfyve lipid kinase complex. *Molecular Cell*, *80*(4). https://doi.org/10.1016/j.molcel.2020.10.003

Lenk, G. M., & Meisler, M. H. (2014). Mouse models of PI(3,5)P2 deficiency with impaired lysosome function. *Methods in Enzymology*, 245–260. https://doi.org/10.1016/b978-0-12-397926-1.00014-7

Lewis, T. R., Kundinger, S. R., Link, B. A., Insinna, C., & Besharse, J. C. (2018). *Kif17 Phosphorylation Regulates Its Ciliary Localization and Photoreceptor Outer Segment Turnover*. https://doi.org/10.1101/351122

Li, P., Hu, M., Wang, C., Feng, X., Zhao, Z., Yang, Y., Sahoo, N., Gu, M., Yang, Y., Xiao, S., Sah, R., Cover, T. L., Chou, J., Geha, R., Benavides, F., Hume, R. I., & Xu, H. (2020). LRRC8 family proteins within lysosomes regulate cellular osmoregulation and enhance cell survival to multiple physiological stresses. *Proceedings of the National Academy of Sciences*, *117*(46), 29155–29165. https://doi.org/10.1073/pnas.2016539117

Liang, F., Zhang, Y., Li, L. *et al.* SpG and SpRY variants expand the CRISPR toolbox for genome editing in zebrafish. *Nat Commun* **13**, 3421 (2022). https://doi.org/10.1038/s41467-022-31034-8

Liggins, M. C., Flesher, J. L., Jahid, S., Vasudeva, P., Eby, V., Takasuga, S., Sasaki, J., Sasaki, T., Boissy, R. E., & Ganesan, A. K. (2018). PIKfyve regulates melanosome biogenesis. *PLOS Genetics*, *14*(3). https://doi.org/10.1371/journal.pgen.1007290

Lin, J., Liu, X., Lu, Z., Huang, S., Wu, S., Yu, W., Liu, Y., Zheng, X., Huang, X., Sun, Q., Qiao, Y., & Liu, Z. (2021). Modeling a cataract disorder in mice with prime editing. *Molecular Therapy - Nucleic Acids*, *25*, 494–501. https://doi.org/10.1016/j.omtn.2021.06.020

Lin, J., Wu, S., Shen, Q., Liu, J., Huang, S., Peng, G., & Qiao, Y. (2021). Base editing-mediated perturbation of endogenous PKM1/2 splicing facilitates isoform-specific functional analysis in vitro and in vivo. *Cell Proliferation*, *54*(8). https://doi.org/10.1111/cpr.13096

Liu, C.-H., Lin, C.-H., Tsai, M.-J., Chen, Y.-H., Yang, S.-F., & Tsai, K.-B. (2017). *Melanin Bleaching with Warm Hydrogen Peroxide and Integrated Immunohistochemical Analysis: An Automated Platform * https://doi.org/10.20944/preprints201703.0167.v1

Liu, K., Petree, C., Requena, T., Varshney, P., & Varshney, G. K. (2019). Expanding the CRISPR toolbox in zebrafish for studying development and disease. *Frontiers in Cell and Developmental Biology*, *7*. https://doi.org/10.3389/fcell.2019.00013

Liu, Y., Li, X., He, S., Huang, S., Li, C., Chen, Y., Liu, Z., Huang, X., & Wang, X. (2020). Efficient generation of mouse models with the prime editing system. *Cell Discovery*, *6*(1). https://doi.org/10.1038/s41421-020-0165-z

Lopes, V. S., Wasmeier, C., Seabra, M. C., & Futter, C. E. (2007b). Melanosome maturation defect in RAB38-deficient retinal pigment epithelium results in instability of immature melanosomes during transient melanogenesis. *Molecular Biology of the Cell*, *18*(10), 3914–3927. https://doi.org/10.1091/mbc.e07-03-0268

Manicam, C., Pitz, S., Brochhausen, C., Grus, F. H., Pfeiffer, N., & Gericke, A. (2014). Effective melanin depigmentation of human and murine ocular tissues: An improved method for paraffin and frozen sections. *PLoS ONE*, *9*(7). https://doi.org/10.1371/journal.pone.0102512

Martin, S., Harper, C. B., May, L. M., Coulson, E. J., Meunier, F. A., & Osborne, S. L. (2013). Inhibition of pikfyve by YM-201636 dysregulates autophagy and leads to apoptosis-independent neuronal cell death. *PLoS ONE*, *8*(3). https://doi.org/10.1371/journal.pone.0060152

Mei, S., Wu, Y., Wang, Y., Cui, Y., Zhang, M., Zhang, T., Huang, X., Yu, S., Yu, T., & Zhao, J. (2022). Disruption of PIKFYVE causes congenital cataract in human and zebrafish. Elife. 2022 Jan 13;11:e71256. doi: 10.7554/eLife.71256.

Min, Sang H., Suzuki, A., Stalker, T. J., Zhao, L., Wang, Y., McKennan, C., Riese, M. J., Guzman, J. F., Zhang, S., Lian, L., Joshi, R., Meng, R., Seeholzer, S. H., Choi, J. K., Koretzky, G., Marks, M. S., & Abrams, C. S. (2014). Loss of pikfyve in platelets causes a lysosomal disease leading to inflammation and thrombosis in mice. *Nature Communications*, *5*(1). https://doi.org/10.1038/ncomms5691

Min, Sang Hee, Suzuki, A., Weaver, L., Guzman, J., Chung, Y., Jin, H., Gonzalez, F., Trasorras, C., Zhao, L., Spruce, L. A., Seeholzer, S. H., Behrens, E. M., & Abrams, C. S. (2019a). PIKfyve deficiency in myeloid cells impairs lysosomal homeostasis in macrophages and promotes systemic inflammation in mice. *Molecular and Cellular Biology*, *39*(21). https://doi.org/10.1128/mcb.00158-19

Moran, A. L., Fehilly, J. D., Floss Jones, D., Collery, R., & Kennedy, B. N. (2022). Regulation of the rhythmic diversity of daily photoreceptor outer segment phagocytosis in vivo. *The FASEB Journal*, *36*(10). https://doi.org/10.1096/fj.202200990rr

Nandrot, E. F., Anand, M., Almeida, D., Atabai, K., Sheppard, D., & Finnemann, S. C. (2007). Essential role for MFG-E8 as ligand for αvβ5 integrin in diurnal retinal phagocytosis. *Proceedings of the National Academy of Sciences*, *104*(29), 12005–12010. https://doi.org/10.1073/pnas.0704756104

Nicot, A.-S., Fares, H., Payrastre, B., Chisholm, A. D., Labouesse, M., & Laporte, J. (2006). The phosphoinositide kinase PIKfyve/Fab1p regulates terminal lysosome maturation in*caenorhabditis elegans*. *Molecular Biology of the Cell*, *17*(7), 3062–3074. https://doi.org/10.1091/mbc.e05-12-1120

Overmeyer, J. H., Young, A. M., Bhanot, H., & Maltese, W. A. (2011). A chalcone-related small molecule that induces methuosis, a novel form of non-apoptotic cell death, in glioblastoma cells. *Molecular Cancer*, *10*(1). https://doi.org/10.1186/1476-4598-10-69

O'Connell, C. E., & Vassilev, A. (2023). *Data from Combined Inhibition of P38mapk and Pikfyve Synergistically Disrupts Autophagy to Selectively Target Cancer Cells*. https://doi.org/10.1158/0008-5472.c.6513483

Penberthy, K. K., Lysiak, J. J., & Ravichandran, K. S. (2018). Rethinking phagocytes: Clues from the retina and testes. *Trends in Cell Biology*, *28*(4), 317–327. https://doi.org/10.1016/j.tcb.2018.01.004

Petri, K., Zhang, W., Ma, J., Schmidts, A., Lee, H., Horng, J. E., Kim, D. Y., Kurt, I. C., Clement, K., Hsu, J. Y., Pinello, L., Maus, M. V., Joung, J. K., & Yeh, J.-R. J. (2021). CRISPR prime editing with ribonucleoprotein complexes in zebrafish and primary human cells. *Nature Biotechnology*, *40*(2), 189–193. https://doi.org/10.1038/s41587-021-00901-y

Ponsford, A. H., Ryan, T. A., Raimondi, A., Cocucci, E., Wycislo, S. A., Fröhlich, F., Swan, L. E., & Stagi, M. (2020). Live imaging of intra-lysosome ph in cell lines and primary neuronal culture using a novel genetically encoded biosensor. *Autophagy*, *17*(6), 1500–1518. https://doi.org/10.1080/15548627.2020.1771858

Prill, K., & Dawson, J. F. (2020). *Homology Directed Repair in Zebrafish: Witchcraft and Wizardry?* https://doi.org/10.31219/osf.io/wnhu9

Qin, W., Lu, X., Liu, Y., Bai, H., Li, S., & Lin, S. (2018). Precise a•t to G•C base editing in the zebrafish genome. *BMC Biology*, *16*(1). https://doi.org/10.1186/s12915-018-0609-1

Rachel, R. A., Nagashima, K., O'Sullivan, T. N., Frost, L. S., Stefano, F. P., Marigo, V., & Boesze-Battaglia, K. (2012). Melanoregulin, product of the DSU locus, links the Bloc-pathway and OA1 in Organelle biogenesis. *PLoS ONE*, *7*(9). https://doi.org/10.1371/journal.pone.0042446

Rafferty, S. A., & Quinn, T. A. (2018). A beginner's guide to understanding and implementing the genetic modification of zebrafish. *Progress in Biophysics and Molecular Biology*, *138*, 3–19. https://doi.org/10.1016/j.pbiomolbio.2018.07.005

Rajala, A., Rajala, R., Gopinadhan Nair, G. K., & Rajala, R. V. (2023). Atlas of phosphoinositide signatures in the retina identifies heterogeneity between cell types. *PNAS Nexus*, *2*(3). https://doi.org/10.1093/pnasnexus/pgad063

Rajala, A., Rajala, R., Teel, K., & Rajala, R. V. S. (2022). Ribosomal targeting strategy and nuclear labeling to analyze photoreceptor phosphoinositide signatures. *Biochimica et Biophysica Acta (BBA) - Molecular and Cell Biology of Lipids*, *1867*(8), 159161. https://doi.org/10.1016/j.bbalip.2022.159161

Rasband, W.S., ImageJ, U. S. National Institutes of Health, Bethesda, Maryland, USA, https://imagej.nih.gov/ij/, 1997-2018.

Rees, H. A., & Liu, D. R. (2018a). Base editing: Precision chemistry on the genome and transcriptome of living cells. *Nature Reviews Genetics*, *19*(12), 770–788. https://doi.org/10.1038/s41576-018-0059-1

Ren, Q., Sretenovic, S., Liu, S., Tang, X., Huang, L., He, Y., Liu, L., Guo, Y., Zhong, Z., Liu, G., Cheng, Y., Zheng, X., Pan, C., Yin, D., Zhang, Y., Li, W., Qi, L., Li, C., Qi, Y., & Zhang, Y. (2021). Pam-less plant genome editing using a CRISPR–Spry Toolbox. *Nature Plants*, *7*(1), 25–33. https://doi.org/10.1038/s41477-020-00827-4

Richter, M. F., Zhao, K. T., Eton, E., Lapinaite, A., Newby, G. A., Thuronyi, B. W., Wilson, C., Koblan, L. W., Zeng, J., Bauer, D. E., Doudna, J. A., & Liu, D. R. (2020). Phage-assisted evolution of an adenine base editor with improved CAS domain compatibility and activity. *Nature Biotechnology*, *38*(7), 883–891. https://doi.org/10.1038/s41587-020-0453-z

Rivero-Ríos, P., & Weisman, L. S. (2022). Roles of pikfyve in multiple cellular pathways. *Current Opinion in Cell Biology*, *76*, 102086. https://doi.org/10.1016/j.ceb.2022.102086

Rosello, M., Serafini, M., Mione, M. C., Concordet, J.-P., & Del Bene, F. (2021). *Disease Modeling by Efficient Genome Editing Using a near Pam-Less Base Editor* in Vivo. https://doi.org/10.1101/2021.06.28.450169

Scholefield, J., & Harrison, P. T. (2021). Prime editing – an update on the field. *Gene Therapy*, *28*(7–8), 396–401. https://doi.org/10.1038/s41434-021-00263-9

Sethna, S., Chamakkala, T., Gu, X., Thompson, T. C., Cao, G., Elliott, M. H., & Finnemann, S. C. (2016). Regulation of phagolysosomal digestion by caveolin-1 of the retinal pigment epithelium is essential for vision. *Journal of Biological Chemistry*, *291*(12), 6494–6506. https://doi.org/10.1074/jbc.m115.687004

Simon, D. A., Tálas, A., Kulcsár, P. I., Biczók, Z., Krausz, S. L., Várady, G., & Welker, E. (2022). Pear, a flexible fluorescent reporter for the identification and enrichment of successfully prime edited cells. *eLife*, *11*. https://doi.org/10.7554/elife.69504

Simone, B. W., Martínez-Gálvez, G., WareJoncas, Z., & Ekker, S. C. (2018). Fishing for understanding: Unlocking the zebrafish gene editor's toolbox. *Methods*, *150*, 3–10. https://doi.org/10.1016/j.ymeth.2018.07.012

Soares, A. C., Ferreira, A., Mariën, J., Delay, C., Lee, E., Trojanowski, J. Q., Moechars, D., Annaert, W., & De Muynck, L. (2021). PIKfyve activity is required for lysosomal

trafficking of tau aggregates and Tau seeding. *Journal of Biological Chemistry*, *296*, 100636. https://doi.org/10.1016/j.jbc.2021.100636

Sparrow, J. R., Gregory-Roberts, E., Yamamoto, K., Blonska, A., Ghosh, S. K., Ueda, K., & Zhou, J. (2012). The bisretinoids of retinal pigment epithelium. *Progress in Retinal and Eye Research*, *31*(2), 121–135. https://doi.org/10.1016/j.preteyeres.2011.12.001

Standage-Beier, K., Tekel, S. J., Brafman, D. A., & Wang, X. (2021). Prime editing guide RNA design automation using pine-cone. *ACS Synthetic Biology*, *10*(2), 422–427. https://doi.org/10.1021/acssynbio.0c00445

Tanaka, S., Yoshioka, S., Nishida, K., Hosokawa, H., Kakizuka, A., & Maegawa, S. (2018). In vivo targeted single-nucleotide editing in zebrafish. *Scientific Reports*, *8*(1). https://doi.org/10.1038/s41598-018-29794-9

Tatiossian, K. J., Clark, R. D. E., Huang, C., Thornton, M. E., Grubbs, B. H., & Cannon, P. M. (2021). Rational selection of CRISPR-Cas9 guide RNAS for homology-directed genome editing. *Molecular Therapy*, *29*(3), 1057–1069. https://doi.org/10.1016/j.ymthe.2020.10.006

Theos AC, Tenza D, Martina JA, Hurbain I, Peden AA, Sviderskaya EV, et al. Functions of adaptor protein (AP)-3 and AP-1 in tyrosinase sorting from endosomes to melanosomes. Mol Biol Cell. 2005; 16 (11):5356–72. Epub 2005/09/16. doi: E05-07-0626 [pii] https://doi.org/10.1091/mbc.E05-07-0626 PMID: 16162817; PubMed Central PMCID: PMC1266432.

Tisi, A., Passacantando, M., Lozzi, L., Riccitelli, S., Bisti, S., & Maccarone, R. (2019). Retinal long term neuroprotection by cerium oxide nanoparticles after an acute damage induced by high intensity light exposure. *Experimental Eye Research*, *182*, 30–38. https://doi.org/10.1016/j.exer.2019.03.003

Umapathy, A., Torten, G., Paniagua, A. E., Chung, J., Tomlinson, M., Lim, C., & Williams, D. S. (2023). Spatiotemporal live-cell analysis of photoreceptor outer segment membrane ingestion by the retinal pigment epithelium reveals actin-regulated scission. *The Journal of Neuroscience*, *43*(15), 2653–2664. https://doi.org/10.1523/jneurosci.1726-22.2023

Vicencio, J., Sánchez-Bolaños, C., Moreno-Sánchez, I., Brena, D., Kukhtar, D., Ruiz-López, M., Cots-Ponjoan, M., Vejnar, C. E., Rubio, A., Melero, N. R., Carolis, C., Pérez-Pulido, A. J., Giráldez, A. J., Kleinstiver, B. P., Cerón, J., & Moreno-Mateos, M. A. (2021). *Genome Editing in Animals with Minimal PAM CRISPR-Cas9 Enzymes*. https://doi.org/10.1101/2021.06.06.447255

Walton, R. T., Christie, K. A., Whittaker, M. N., & Kleinstiver, B. P. (2020). Unconstrained genome targeting with near-pamless engineered CRISPR-Cas9 variants. *Science*, *368*(6488), 290–296. https://doi.org/10.1126/science.aba8853

Wensel, T. G. (2020). Phosphoinositides in retinal function and disease. *Cells*, *9*(4), 866. https://doi.org/10.3390/cells9040866

Wierson, W. A., Welker, J. M., Almeida, M. P., Mann, C. M., Webster, D. A., Torrie, M. E., Weiss, T. J., Kambakam, S., Vollbrecht, M. K., Lan, M., McKeighan, K. C., Levey, J., Ming, Z., Wehmeier, A., Mikelson, C. S., Haltom, J. A., Kwan, K. M., Chien, C.-B.,

Balciunas, D., … Essner, J. (2020). Efficient targeted integration directed by short homology in zebrafish and mammalian cells. *eLife*, *9*. https://doi.org/10.7554/elife.53968

Wiley, D. S., Redfield, S. E., & Zon, L. I. (2017). Chemical screening in zebrafish for novel biological and Therapeutic Discovery. *The Zebrafish - Disease Models and Chemical Screens*, 651–679. https://doi.org/10.1016/bs.mcb.2016.10.004

Xue, N., Liu, X., Zhang, D., Wu, Y., Zhong, Y., Wang, J., Fan, W., Jiang, H., Zhu, B., Ge, X., Gonzalez, R. V., Chen, L., Zhang, S., She, P., Zhong, Z., Sun, J., Chen, X., Wang, L., Gu, Z., … Zhang, X. (2023). Improving adenine and dual base editors through introduction of TADA-8E and rad51dbd. *Nature Communications*, *14*(1). https://doi.org/10.1038/s41467-023-36887-1

Yang, H., Ren, S., Yu, S., Pan, H., Li, T., Ge, S., Zhang, J., & Xia, N. (2020). Methods favoring homology-directed repair choice in response to CRISPR/cas9 induced-double strand breaks. *International Journal of Molecular Sciences*, *21*(18), 6461. https://doi.org/10.3390/ijms21186461

Yang, S., Zhou, J., & Li, D. (2021). Functions and diseases of the retinal pigment epithelium. *Frontiers in Pharmacology*, *12*. https://doi.org/10.3389/fphar.2021.727870

Yao J, Jia L, Feathers K, Lin C, Khan NW, Klionsky DJ, Ferguson TA, Zacks DN. Autophagy-mediated catabolism of visual transduction proteins prevents retinal degeneration. Autophagy. 2016 Dec;12(12):2439-2450. doi: 10.1080/15548627.2016.1238553. Epub 2016 Oct 18. PMID: 27753525; PMCID: PMC5173283.

Yazulla, S., & Studholme, K. M. (2002). Neurochemical anatomy of the zebrafish retina as determined by immunocytochemistry. *Chemical Anatomy of the Zebrafish Retina*, 3–44. https://doi.org/10.1007/978-1-4615-1089-5_2

Zhang, X., Chow, C. Y., Sahenk, Z., Shy, M. E., Meisler, M. H., & Li, J. (2008). Mutation of FIG4 causes a rapidly progressive, asymmetric neuronal degeneration. *Brain*, *131*(8), 1990–2001. https://doi.org/10.1093/brain/awn114

Zhang, Y., Qin, W., Lu, X., Xu, J., Huang, H., Bai, H., Li, S., & Lin, S. (2017). Programmable base editing of zebrafish genome using a modified CRISPR-Cas9 system. *Nature Communications*, *8*(1). https://doi.org/10.1038/s41467-017-00175-6

Zhang Y, Zhang Z, Ge W. An efficient platform for generating somatic point mutations with germline transmission in the zebrafish by CRISPR/Cas9-mediated gene editing. J Biol Chem. 2018 Apr 27;293(17):6611-6622. doi: 10.1074/jbc.RA117.001080. Epub 2018 Mar 2. PMID: 29500194; PMCID: PMC5925810.

Zheng, S., Liang, F., Zhang, Y., Fei, J.-F., Qin, W., & Liu, Y. (2023). Efficient pam-less base editing for zebrafish modeling of human genetic disease with Zspry-ABE8E. *Journal of Visualized Experiments*, (192). https://doi.org/10.3791/64977

Zolov, S. N., Bridges, D., Zhang, Y., Lee, W.-W., Riehle, E., Verma, R., Lenk, G. M., Converso-Baran, K., Weide, T., Albin, R. L., Saltiel, A. R., Meisler, M. H., Russell, M. W., & Weisman, L. S. (2012). In vivo, Pikfyve generates pi(3,5)p2, which serves as both a signaling lipid and the major precursor for PI5P. *Proceedings of the National Academy of Sciences*, *109*(43), 17472–17477. https://doi.org/10.1073/pnas.1203106109